ROTATIONAL AND VIBRATIONAL RAMAN SPECTROSCOPY FOR THERMOCHEMISTRY MEASUREMENTS IN SUPERSONIC FLAMES

A Dissertation

by

ALEXANDER CHRISTIAN BAYEH

Submitted to the Office of Graduate Studies of
Texas A&M University
in partial fulfillment of the requirements for the degree of

DOCTOR OF PHILOSOPHY

Approved by:

Chair of Committee,	Adonios N. Karpetis
Committee Members,	Rodney Bowersox
	Sharath Girimaji
	Simon North
Head of Department,	Rodney Bowersox

August 2013

Major Subject: Aerospace Engineering

ABSTRACT

High speed chemically reacting flows are important in a variety of aerospace applications, namely ramjets, scramjets, afterburners, and rocket exhausts. To study flame extinction under similar high Mach number conditions, we need access to thermochemistry measurements in supersonic environments. In the current work a two-stage miniaturized combustor has been designed that can produce open supersonic methane-air flames amenable to laser diagnostics. The first stage is a vitiation burner, and was inspired by well known principles of jet combustors. We explored the salient parameters of operation experimentally, and verified flame holding computationally using a well-stirred reactor model. The second stage of the burner generates an external supersonic flame, operating in premixed and partially premixed modes. The very high Mach numbers present in the supersonic flames should provide a useful testbed for the examination of flame suppression and extinction using laser diagnostics. We also present the development of new line imaging diagnostics for thermochemistry measurements in high speed flows. A novel combination of vibrational and rotational Raman scattering is used to measure major species densities (O_2, N_2, CH_4, H_2O, CO_2, CO, & H_2) and temperature. Temperature is determined by the rotational Raman technique by comparing measured rotational spectra to simulated spectra based on the measured chemical composition. Pressure is calculated from density and temperature measurements through the ideal gas law. The independent assessment of density and temperature allows for measurements in environments where the pressure is not known a priori. In the present study we applied the diagnostics to laboratory scale supersonic air and vitiation jets, and examine the feasibility of such measurements in reacting supersonic flames. Results of full thermochemistry were obtained for the air and vitiation jets that reveal the expected structure of an underexpanded jet. Centerline traces of density, temperature, and pressure of the air jet agree well with computations, while measurements of chemical composition for the vitiation flow also agree well with predicted equilibrium values. Finally, we apply the new diagnostics to the exhaust of the developed burner, and show the first ever results for density, temperature, and pressure, as well as chemical composition in a supersonic flame.

DEDICATION

To my father, Albert Fouad Bayeh

ACKNOWLEDGEMENTS

I would like to extend my gratitude to my advisor, Dr. Adonios Karpetis, for guiding my research efforts, his continued support, and for pushing me to always try harder. I would like to extend my gratitude to my committee members, Dr. Rodney Bowersox, Dr. Simon North, and Dr. Sharath Girimaji.

I would also like to thank everyone I have worked with in the lab and our group over the course of the past 6 years. I owe a great deal to this collective group for their many contributions, namely Adam Johnson, Celine Kluzek, Ben Cohen, Carl Mullins, Luke Richards, Ryan Haughey, Wenjiang Xu, and Dean Ellis. Additionally, I would like to thank my close friends and family for all of their support and encouragement over the last few years.

TABLE OF CONTENTS

LIST OF FIGURES

LIST OF TABLES

TABLE Page

1. INTRODUCTION

Modern propulsion systems frequently employ high-speed flows through their devices. Fuel and oxidizer streams are sometimes mixed and burned under high velocity and strain rate conditions that may lead to strong coupling between the local flow field and the prevailing chemistry. Examples include rockets, turbojets and scramjet propulsion systems. Chemical rocket systems always involve low propellant speeds in the rocket chamber, where combustion is nearly always completed, and very high flow speeds in the nozzle expansion, where chemical reactions are usually ‘frozen’ as a result of the short transient times [42]. Turbojet systems involve high speed air flows in the combustors, and even higher speeds in the afterburner and nozzle expansions downstream of the combustors [42]. Chemistry is often affected by the high speeds involved in turbojet systems, as evidenced by the presence of unburnt hydrocarbons and chemical reactions in the wake of afterburner exhausts. Finally, scramjet propulsion systems involve flows that are supersonic almost everywhere in the combustor, and require special design considerations before reactions can take place and the chemical release necessary for propulsion can be effected [19]. In addition to the expected coupling of subsonic fluid flow with chemistry, all three propulsion systems exhibit regions where the flow becomes supersonic, and thus provide examples of an even more extreme interaction between flow and chemistry. Supersonic flows involve significant pressure variation, due to the presence of expansion fans and compression shock waves. These, in turn, result in high local fluid acceleration and deceleration, and ultimately very high strain rates that may significantly affect chemical reactions.

The main objectives of the present work are the design and construction of a miniature burner for the generation of ‘canonical’ supersonic flames, and the development of a new laser diagnostics system to examine the full thermochemistry within supersonic flows. The motivation for this research comes from the need for a complete study of thermochemistry and the quantification of flow-chemistry interaction in the presence of supersonic waves and pressure variation [11]. A small and select group of research studies have performed laser diagnostics experiments in supersonic combustion in the past. Experiments can generally fit in one of two categories; combustion in supersonic wind tunnels [2, 80, 20, 47, 60], as well as in lab based scramjet combustors [74, 34]. Both types of studies have employed various laser and optical diagnostics techniques, such as Coherent Anti-Stokes Raman Scattering (CARS, e.g. [80]), or Planar Laser-Induced Fluorescence (PLIF, e.g. [60]). However, both of these experimental configurations necessitate the use of optical windows, which in turn require the use of laser diagnostics with relatively high signals, such as CARS and PLIF. The presence of windows would be detrimental to a low signal scattering technique, such as the incoherent Raman scattering that we employ [13]. Despite that, incoherent Raman techniques have been used in isobaric environments using windows[57, 94].

Optically accessible supersonic flames have been developed in the past that do not hinder techniques such as incoherent Raman [23, 68, 18]. These flames, however, operate in a mode that mixes and burns fuel and oxidizer in a coflow shear layer external to the burner. In that regard, these burners operate in a non-premixed configuration, and the research performed in such environments studies the flame holding that takes place within the shear layer close to the flame exit. The present work concentrates on premixed and partially premixed burning that takes place far from walls and boundaries, and is relatively unaffected by boundary layers. The burner constructed by Klavuhn and McDaniel [55] achieves premixed supersonic burning, and is very similar to the objective of the present study. However, supersonic conditions are achieved through use of a vacuum chamber at the exit of the burner nozzle. Operation under these conditions requires the use of optical windows for access, and provide flames with lower number densities, both of which are detrimental to low light level laser diagnostics.

In many respects, the optimum configuration for a canonical supersonic flame is that of a real full-scale jet afterburner. Laser diagnostics has been applied in such extreme environment [27], yet high risk and prohibitive expense make this type of experiment impractical. Our design seeks to miniaturize the jet afterburner concept, and thus provide a testbed that is suitable for the application of optical techniques. In the present work we develop a canonical supersonic premixed flame that is open to the ambient atmosphere, and is therefore amenable to laser diagnostics. The overall operation of our miniature system closely resembles that of a jet combustor and afterburner exhaust. The flame can be operated under high Reynolds numbers and modest supersonic Mach numbers, thus allowing for the study of compressibility and the effects of expansion/compression waves in chemically reacting flows. In what follows we explore the salient parameters of the burner operation experimentally, and verify traditional flame holding scaling [67, 62] computationally using a well-stirred reactor model. Additionally, we present results of the external supersonic flame, operating in both premixed and partially premixed modes, and examine flame phenomenology.

In the present work we also describe an incoherent vibrational and rotational Raman spectrometer capable of full thermochemistry measurements, i.e. major species composition X_i, temperature T and pressure P, using a single laser and detector arrangement. Vibrational Raman spectra are used for the direct measurement of species concentrations of the main products of combustion (N_2, O_2, CH_4, CO_2, H_2O, CO, and H_2)[35, 9, 36, 65, 94, 18, 71, 79, 61, 40], while their combined rotational Raman spectra are used to determine temperature. In the current work, temperature is calculated from the rotational Raman spectra based on the combined profile integral and location of the profile peak [57, 58]. The independent measurements of concentration and temperature allow for the calculation of pressure using an equation of state. This novel combination allows for the application of the developed technique in non-isobaric flows where the pressure is not known a priori. In what will follow, we highlight and discuss the major techniques and contributions to the field.

Raman measurements in supersonic hydrogen-air diffusion flames by R. Pitz and his group at Vanderbilt [18] provide one of the earliest applications of incoherent Raman scattering to supersonic flames. As noted above, the flame configuration that was examined corresponds to a mode that mixes and burns fuel and oxidizer in a coflow shear layer external to the burner. Major species concentrations were measured using Stokes vibrational incoherent Raman scattering within the flow field. Vibrational Raman signals were collected using a single array of photomultiplier tubes (PMT's) positioned on each spectral channel. This resulted in a single point measurement of species concentrations, as opposed to the one-dimensional measurements we are capable of making with a spectral camera. Temperature measurements were performed using an additional PMT to monitor the N_2 anti-Stokes signal, and examining the ratio between it and its corresponding Stokes signal.

Vibrational Raman measurements have been performed in both laminar and turbulent flames extensively by R.S. Barlow and coworkers in Sandia National Labs [5, 6, 4, 9, 35, 52, 66, 7]. Simultaneous temperature measurements, however, were performed mostly using Rayleigh scattering on a separate imager. Although temperature and density measurements were performed independently, the flame measurements were all isobaric and at one atmosphere. In our research we advance the state of the art by performing both sets of measurements on the same imager, and examine non-isobaric environments where pressure is not known.

Simultaneous temperature and pressure measurements in supersonic jet have been been reported by R. Miles and collaborators at Princeton [33, 76, 32]. Planar measurements of temperature and pressure (as well as velocity) are performed by spectrally resolving both the scattering line shapes and Doppler shifts of the Rayleigh signal that has been notch filtered. The experiments, however, require that the composition be known prior to measurements. This excludes the technique from being applied to reacting flows where the composition is not known a priori, and must be measured in order to characterize temperature and pressure. The technique provides spatial measurements in two dimensions for quantities of interest, which can be desirable over one-dimensional measurements, but cannot be applied to flows of interest to the current research because of its lack of full thermochemistry.

Coherent anti-Stokes Raman spectroscopy has been widely used to measure temperature, pressure, and a limited amount of species in various flows [31, 27, 20, 98, 59, 68, 80, 2, 95]. This technique boasts a large advantage with regards to signal to noise ratio because of the coherent signal that is collected from the test section. The technique, however, is limited to measurements at a single point for very few (typically one or two) species, and typically performs measurements using N_2. Work performed by A.D. Cutler and his group at NASA Langley have developed a variation of CARS denoted as width-increased dual-pump enhanced coherent anti-Stokes Raman spectroscopy (WIDECARS)[95]. The technique utilizes a broadband Stokes dye laser, as well as a dual pump technique, that allows for measurements of temperature and mole fractions for up to six species, namely N_2, O_2, H_2, C_2H_4, CO, and CO_2. It should be noted that two species of interest are not captured by this technique, namely H_2O and CH_4. Water is a major product of both hydrogen and hydrocarbon combustion, and therefore the technique requires additional measurements to properly quantify the flow composition. Spatial measurements using any CARS technique must be formed by scanning the flow field with the laser probe volume, which is complicated by the presence of multiple laser beams. Additionally, this adds the requirement that the flow being measured must be steady and repeatable if a scan is being performed.

The Raman line imaging spectrometer described in this work combines a large portion of the salient features mentioned above. These features include: the independent measurement of temperature and density using a single laser-imager combination, species sensitivity for composition measurements, one-dimensional spatial measurements of the mentioned quantities, and applicability of the technique to non-isobaric conditions. Initial measurements with the Raman line imaging spectrometer were performed in the wake of a supersonic cold air jet. The jet exhaust was scanned using the newly developed technique, and the measurements were compared with computational results for calibration of the rotational Raman temperature technique. The final results of the jet scan provide the first ever one-dimensional thermochemistry measurements in a supersonic environment.

A supersonic jet of hot vitiation products from the supersonic burner was also scanned using the developed diagnostics. The scan provides a calibration and test bed for the technique because of its elevated temperatures, and composition that includes combustion products. The measurements produced by the scan provide a good calibration for species concentrations and possible interferences in anticipation for measurements in flames. Finally, the Raman line imaging spectrometer was applied to the exhaust of a supersonic flame. The flame was scanned similarly to the air and vitiation jets, and provided the first ever measurements of full thermochemistry in a supersonic flame. Although the measurements in the flame are initial results, they show the feasibility of applying a new diagnostic technique in an environment and flow that is difficult to measure.

2. SUPERSONIC FLAMES

2.1 Underexpanded jets

Flow from a supersonic nozzle offers an experimental environment with both varying pressure and optical accessibility. Expansion and shock waves due to the supersonic flow give rise to large pressure variations within the flow. Two types of jets are possible from a supersonic nozzle, over- and underexpanded. The two are differentiated based on the pressures at the nozzle exit, with respect to the local atmospheric pressure. Supersonic jets that exhibit an exit pressure (P_e) greater than the atmospheric pressure (P_a) are referred to as underexpanded jets [97]. When the opposite case is true (exit pressure greater than atmospheric), an overexpanded jet it formed at the exit of the nozzle. An under expanded jet configuration is chosen for the purpose of laser diagnostics due to the higher number densities associated with the flow.

For an underexpanded jet, the pressure at the nozzle exit first comes into equilibrium with the surrounding atmosphere by expansion through Prandtl-meyer waves [1], as seen in Fig. 2.1. The expansion waves pass through the centerline of the jet and interact with the expansion waves emanating from the rest of the nozzle tip. After the interaction, the expansion waves continue until they interact with the jet boundary, a constant pressure slip line that separates the high speed flow from the stagnant, or low speed, surroundings. The expansion waves reflect off of the jet boundary as compression waves, and coalesce onto each other. If the exit pressure is modestly greater than the atmospheric pressure ($P_e > P_{atm}$), the compression waves will coalesce into an oblique shock. The oblique shock waves impinge on each other at the jet centerline, and reflect outwards back towards the jet boundary. From here the shocks are reflected off as a set of expansion fans, and the process is repeated. Each successive iteration is weaker than the previous due to entropy generation by the shocks, as well as viscous effects. Eventually the flow cannot recover from the shocks and viscous losses, and the flow becomes subsonic and highly turbulent [50].

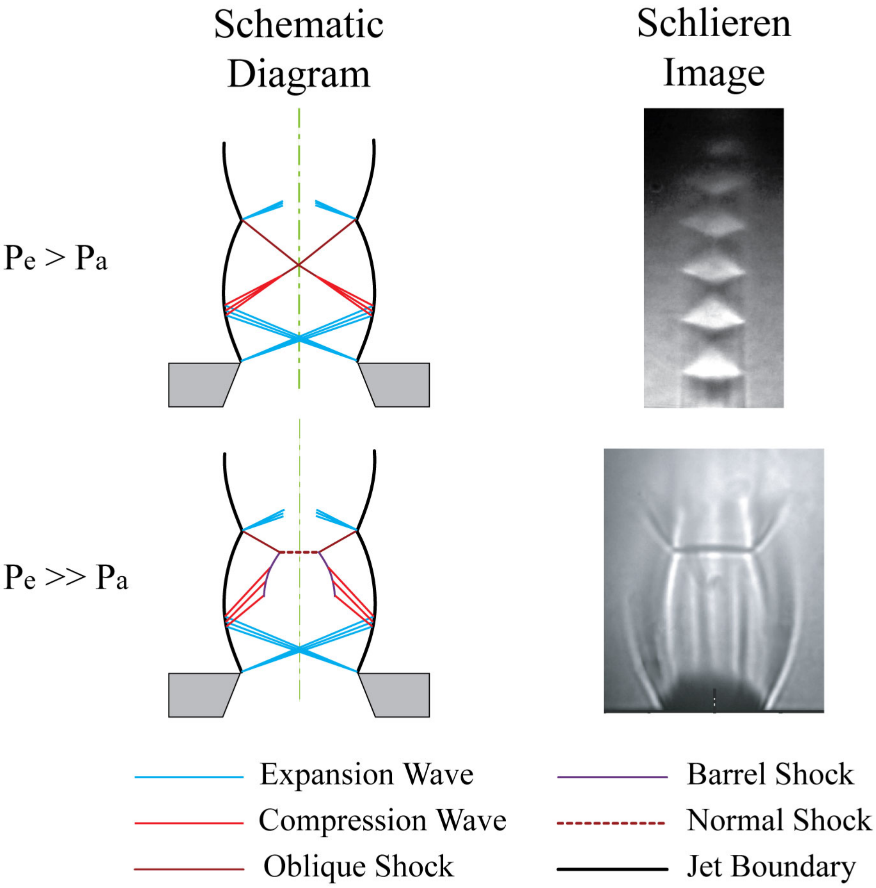

Figure 2.1: Schlieren images and schematic drawings of underexpanded jets

A different variation of this observed when the exit pressure at the tip of the nozzle is much greater than that of the atmospheric pressure ($P_e >> P_{atm}$). The incident angles of the oblique shocks at the jet axis are extremely shallow (shown as the barrel shock), and a simple reflected shock is not capable of keeping the flow parallel to the centerline. To correct for this, a normal shock occurs at the jet centerline, and is connected to the incident and reflected socks by a triple point, as seen in Fig. 2.1. In cylindrical coordinates, the normal shock forms the Mach disk when rotated about the axis of symmetry. Similar to the other case, the reflected shocks from the triple point will propagate towards jet boundary and restart the process once again. If there is enough pressure loss due to the presence of the normal shock, the repeated patterns will mimic the flow configuration described for the mildly underexpanded case.

Along the jet centerline the flow oscillates between over- and underexpansion, and hence oscillates between Mach numbers as well. The underexpanded flow at the jet exit undergoes multiple expansion waves along the jet centerline. Expansion waves emanating from the nozzle circumference interact at the jet centerline, and cause the centerline pressure to become less than atmospheric (overexpanded). Shortly thereafter, the normal or oblique shocks compress the flow to a pressure similar to the exit pressure of the nozzle. As the process is repeated, pressure losses across the shocks will bring the levels of under- and overexpansion closer to the atmospheric pressure until the jet can no longer recover.

Sample chemiluminescence images of under expanded flames, as well as accompanying schlieren images, can be seen in Fig. 2.2. Total pressure of the combustion chamber is increased from left to right, where Fig. 2.2 (a) begins at 45 *psig* and (f) ends at 95 *psig*, with 10 *psig* increments between each sample set. The chemiluminescence and schlieren images from Fig. 2.2(a) through (s) show the clear structure of a mildly underexpanded jet case, and the 'Mach diamond' structure is repeated until it is no longer discernible. Between Figs. 2.2(c) and (d), it can be seen that the supersonic flow shifts from the oblique shock configuration at the jet centerline, to a

Mach disk configuration due to the increased exit pressure. Figures 2.2 (d) through (f) show a clear increase in the diameter of the Mach disk with pressure, and the post-shock subsonic regions are highlighted by increased chemiluminescence where combustion may be taking place.

2.2 Supersonic burner

2.2.1 Configuration

An illustration of the burner design used in this study is shown in Fig. 2.3, as well as a picture of the burner in operation. The objective of our design was the generation of an external supersonic flame that would be accessible to laser diagnostics. To that end we followed well known principles of jet combustor design [63, 62]. The burner is built around two successive stages, as shown in Fig. 2.4. The first stage is a vitiation burner, similar in concept to the one found in jet combustors. In the first stage an overall lean burning was designed between the vitiation air and fuel, A_V and F_V, respectively. This was done mainly to ensure excess air is present in the vitiation products, but also to avoid high temperatures that could potentially melt the device. Since this equivalence ratio ($\phi_V \sim 0.4$) is below the lean flammability limit for methane-air flames (~ 0.53 [16]), the vitiation air A_V cannot be premixed with the fuel all at once, and must be divided into two streams before ignition and flameholding take place. Apportioning of the air stream is effected by proper selection of the areas for the openings that admit air into the combustor. This multiple airstream design was influenced by actual jet combustors, where primary, secondary, and sometimes tertiary air injection is used to create the proper reacting flowfield in the combustor [62].

The first air stream represents approximately 40% of the total vitiation air A_V, and is denoted in Fig. 2.4 as A_B (burning air). This fraction of air A_B is

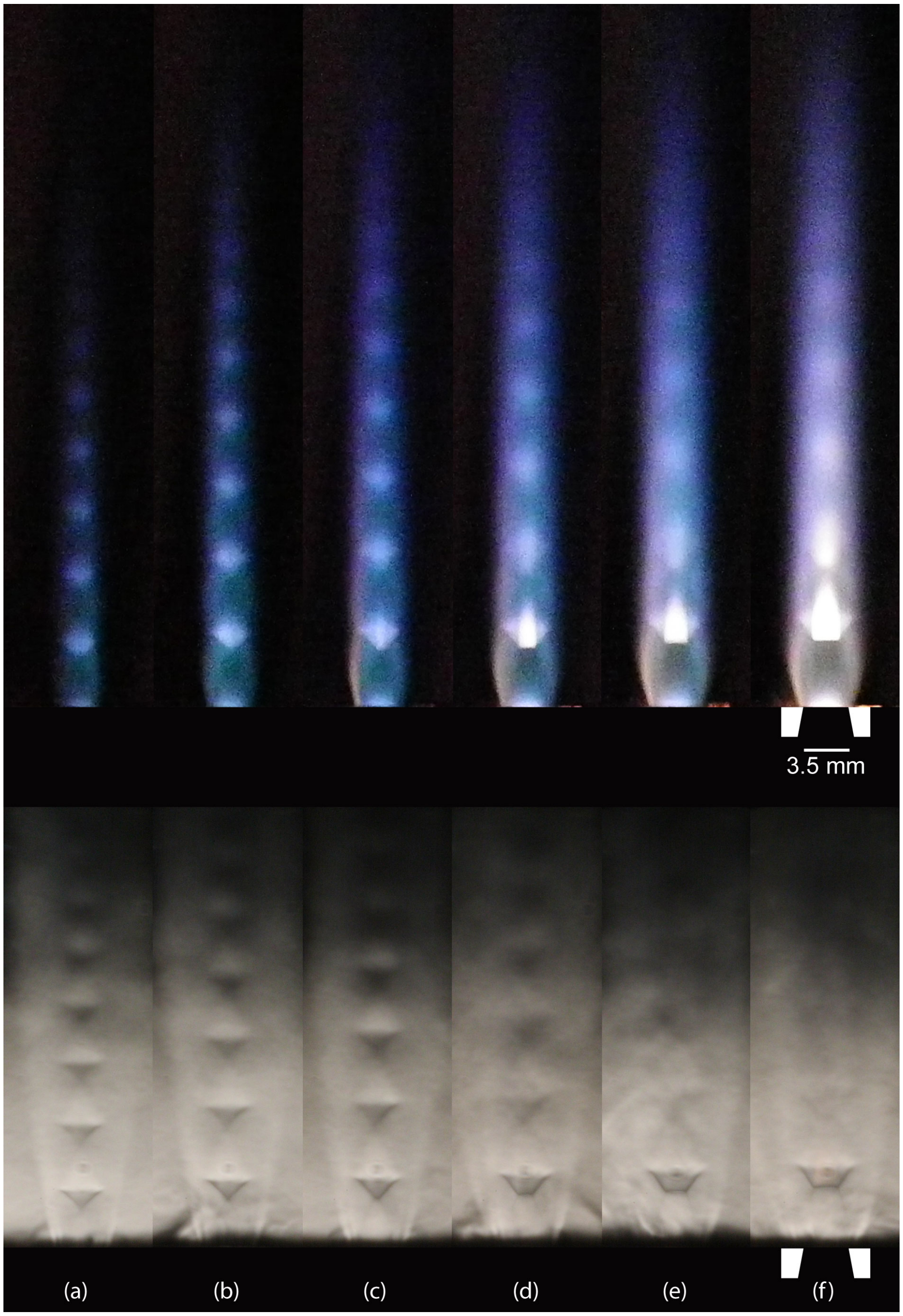

Figure 2.2: Chemiluminescence images of external supersonic flame with corresponding schlieren. Equivalence ratio $\phi_E = 1.9$ corresponds to partially premixed conditions. The chamber back pressure is increased from 45 to 95 psia from left to right those show the flow structure development.

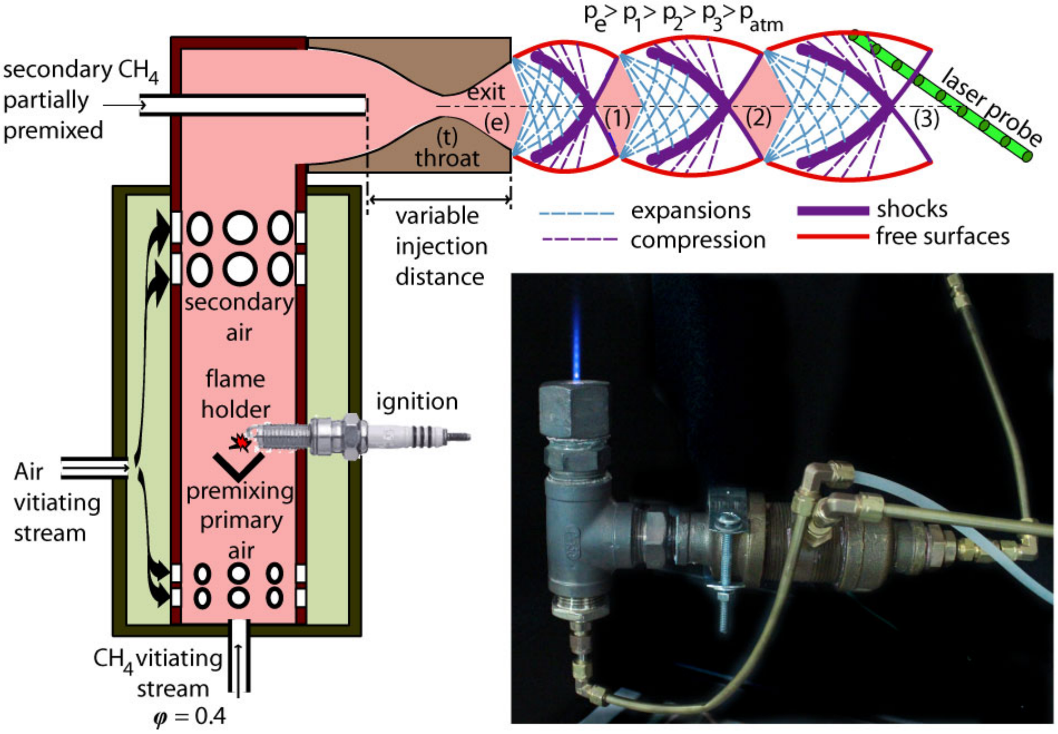

Figure 2.3: An illustration of the burner operation. The inset picture shows a long exposure image of the burner under operational conditions.

mixed with the fuel F$_V$, and the premixture is ignited and burned within the ignition/flameholding region shown in the schematic. The equivalence ratio formed by air A$_B$ and fuel F$_V$ (ϕ_B) must be within the flammability limits for methane air flames, and this is one of the major parameters of interest in the following section. The remaining 60% of the vitiation air is denoted in Fig. 2.4 as A$_D$ (dilution air). This fraction of air is added after the combustion to dilute the vitiation products and lower their temperature to sustainable levels. The final vitiation equivalence ratio ϕ_V that results from adding the dilution air to the products is important for the prediction of composition at the exit of the premixed vitiation burner. As shown in Fig. 2.4 that mixture consists of combustion products P$_V$ and excess air A$_E$ that is used for the external flame in the second stage.

Methane was chosen as the fuel in our experiments because of its reduced propen-

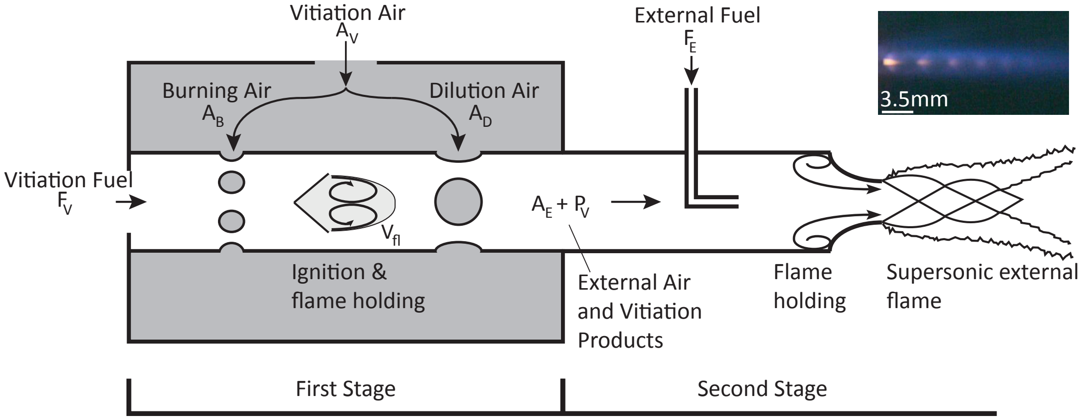

Figure 2.4: Combustion chamber configuration with sample supersonic flame. Vitiation fuel F_V and vitiation air A_V burn and produce the hot stream containing air A_E and products P_V; additional fuel F_E is injected and burns in the second stage.

sity to producing soot particles [38]. The Raman laser diagnostics relies on extremely low-level scattering techniques [26, 53], and as a result soot production through the flame had to be suppressed at all costs. Unlike liquid fuel burners that utilize swirl-atomization for fuel injection, a gas fuel combustor requires a recirculation region for flame holding [63, 88]. For that purpose, a bluff body was inserted into the vitiation burner for flame holding purposes, as shown in Fig. 2.4. Local velocities in the bluff body recirculation are lower than speeds of methane air flames, and flame holding is maintained as recirculated hot products continuously ignite reactants [28]. A spark plug, embedded in the flame holder, is used for ignition.

The second stage of our burner utilizes the hot vitiated products (P_V) and excess air (A_E) coming out of the first stage to generate the external flame. Additional fuel (F_E) is injected into the mixture with an equivalence ratio ϕ_E, based on the excess air (A_E). This equivalence ratio is an important design parameter since it determines the character and overall phenomenology of the external flame. The prevailing temperatures after the first vitiation stage is approximately 1300 K (based on adiabatic equilibrium calculations) and this value is sufficiently high for the ignition and establishment of an external flame. As discussed subsequently, flame holding occurs prior to the nozzle, and the resulting premixed flame accelerates through a nozzle and extends into the supersonic flow. The simple converging nozzle provides a sonic line at the exit ($d_e = 3.5$ mm), but also generates a supersonic flow as a result of isentropic expansion after the exit [1]. A sample flame can be seen in Fig. 2.4. The burner configuration allows for variation of multiple parameters of the external supersonic flame, namely equivalence ratio ϕ_E, exit pressure P_E, and Mach number. The burner design and resulting flame is akin to the flowfield seen in afterburner exhausts [27]. The small scale of the current system allows for safe bench top experimentation, with ease and economy of use.

In the supersonic flame the light emanates from low speed, subsonic regions following shock waves. Conversely, dark regions correspond to high speed supersonic flow where the reactions cannot keep up with the fast fluid mechanics, resulting in flame extinction. This flow pattern is reproducible, stationary, and quasi-laminar, thus simplifying the application of laser diagnostics and resulting in high signal to noise ratio for our experiments by allowing averaging of many laser shots for each measurement [26, 12]. The pressure variation inherent in supersonic flames is the topic of our current research [11]. The interchange of shocks and expansion wave trains continues until the flow can no longer recover from pressure losses and viscous effects, at which point the flow is everywhere subsonic. As a result the flow becomes fully turbulent in these regions and no stationary fluid mechanic structure can be discerned.

The supersonic flames generated by the burner provide some of the highest Reynolds numbers accessible to laser diagnostics. Past research concentrated on measurements in turbulent flames with Reynolds numbers up to ~100,000 [5, 66]. The present system can easily generate Reynolds numbers on the order of 300,000 under cold conditions. A simple calculation based on the sample flame, shown in Fig. 2.4, can provide an estimate of prevailing strain rates in the supersonic flow. The resulting value of strain is 10^5 s^{-1}, which is much higher than the highest previously measured ($\sim 10^3$ s^{-1}) [52]. In those high strain regions reactions are suppressed and flames tend to be extinguished, as shown in Fig. 2.4. It is precisely these regions that are the most interesting target for investigation using the laser diagnostics [11].

2.2.2 Internal vitiation

The earliest study of flame holding behind bluff bodies was performed by Longwell *et al.* [67], and later expanded and applied by Lefebvre [62] to flame holding within gas turbine combustors. Flame holding and blow-off limits were characterized by the parameter $\dot{m}/V_{fl}P^n$; where $\dot{m}$ is the mass flow rate through the flame holder, P is the pressure, n is the overall order of the reaction, and V_{fl} is the recirculation and flame holding volume. By using a Well Stirred Reactor (WSR) model, and a simple single step global reaction, the authors of reference [67] conclude this parameter ($\dot{m}/V_{fl}P^n$) is a function only of equivalence ratio. This scaling predicts the intuitively correct behavior of flame blow-off at increasing mass flow rate, and decreasing pressure. It is precisely this scaling that explains why combustors tend to blow-off more at high altitudes, and require larger volumes for stable flame holding at these conditions. In the present study we use this scaling to design the vitiation burner, and explain the regions of stability and flammability. This is accomplished experimentally and computationally as seen below.

Experiments were performed using the first stage of the burner system, shown in Fig. 2.4, open to atmospheric conditions. The open configuration allowed visible access to the flame holder, and maintained a constant atmospheric pressure throughout the experiments. The vitiation burner is normally operated at high pressures (P), and the mass flow rate ($\dot{m}$) through the choked nozzle is proportional to that pressure. As a result the mass flow rate and pressure can not be varied independently, unless the second stage is removed and the experiments are performed under constant pressure. For each experiment, the burner was started at minimum operating conditions, and the mass flow rate was steadily increased until blow-off was observed, as shown in Fig. 2.5. The results indicate measurement points where instances of stable flame holding were observed, and when flame blow-off occurred. Visual observation of the flame holder showed the flame anchored within the bluff body, as shown schematically in Fig. 2.4. This indicates that the vitiation fuel (F_V) is mixing with the burning air (A_B), forming a flammable premixture with an equivalence ratio ϕ_B.

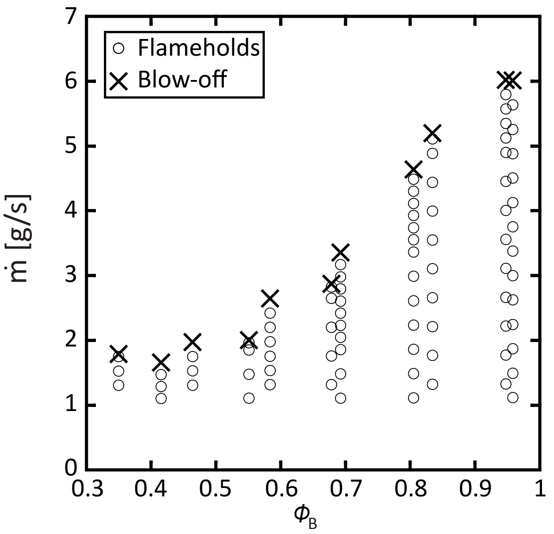

Figure 2.5: Experimental flame holding results of the vitiation stage. Circles denote conditions with stable flame holding, while x's denote flame blow-off. The equivalence ratio ϕ_B corresponds to the premixture formed by the vitiation fuel (F_V) and burning air (A_B).

The results shown in Fig. 2.5 are presented in terms of this equivalence ratio ϕ_B, and the ordinate is the flow rate $\dot{m}$ of the two relevant streams (F_V and A_B). We may infer from these atmospheric results, that flame holding is more robust closest to stoichiometric conditions, and this will be our operating condition.

Considering the difficulty of changing pressure and/or volume experimentally, we opted for detailed chemistry computations of the WSR problem. The purpose of the computations was to explain the experimental flame holding limits, to extend our analysis to higher pressures, and verify the relevance of the theoretical parameter $\dot{m}/V_{fl}P^n$. Atmospheric computations were carried out for the WSR using reactor models in Cantera [39], and utilized the GRI 3.0 detailed chemistry mechanism for methane [93]. The governing equations of the reactor models are based on open system species and energy conservation equations at steady state and steady flow. The species conservation equations for the WSR at steady state are

$$Y_{j,e} = \frac{V\dot{\omega}_j MW_j}{\dot{m}} + Y_{j,0} \tag{2.1}$$

where for every species j, $Y_{j,0}$ and $Y_{j,e}$ are respectively the inlet and outlet mass fractions, $\dot{\omega}_j$ is the chemical production rate, V is the reactor volume, and MW_j is the molecular weight [54, p. 663]. As seen in the above equation, the relevant parameter for the computational problem is $\dot{m}/V$. This parameter, related to the transient time through the reactor $m/\dot{m}$, was varied in our computations to determine flammability limits using the WSR model. Specifically, the progress of reacting species was examined to evaluate the presence of reaction, which was interpreted as successful flame holding. Conversely, a negligible variation in composition, as judged by $Y_{j,0} - Y_{j,e}$, was considered as blow-off. This process was repeated for numerous values of equivalence ratio ϕ that span the range of experimental values ϕ_B.

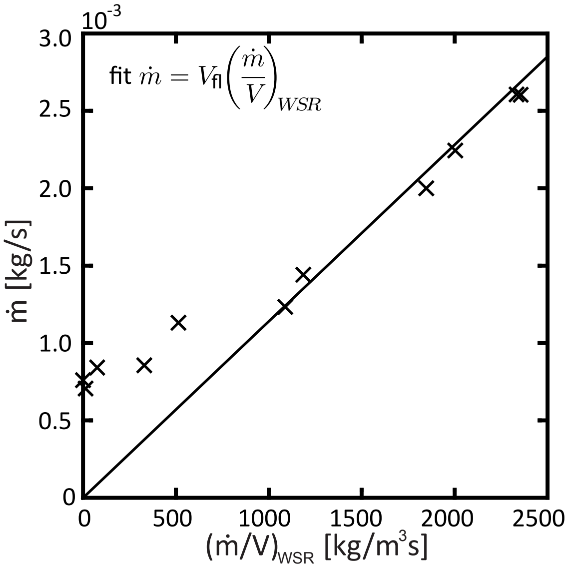

Figure 2.6: Experimental blow-off mass flow rates of the vitiation stage versus their respective WSR result. All experiments and computations were performed at one atmosphere. The slope of a linear fit, forced to pass through the origin, serves as a measurement of flame volume V_{fl}. This volume relates the mass flow rates measured experimentally ($\dot{m}$) to the results of the WSR model ($\dot{m}/V$).

To relate the computational results with those of the experiment, a physical volume, corresponding to the recirculation volume of the flame holder, must be calculated. Figure 2.6 shows the experimental blow-off mass flow rates plotted against WSR results at the same equivalence ratio ϕ_B. In the figure, high values of mass flow rate correspond to near stoichiometric values of ϕ_B, while the smaller values correspond to the lean conditions. These results suggest a constant flame holding volume, particularly for the equivalence ratios closest to stoichiometric. The constant flame holding volume approximation agrees with visual observation of the flame holder during operation. The empirical value V_{fl}, is identified as the slope of the linear fit passing through the origin in Fig. 2.6, and the calculated value of approximately 1 cm^3 corresponds to the physical size of the flame holder. The realistic value for V_{fl} offers some confidence in the computational approach of the present work. Early research of bluff body flame stabilization [28, 101, 87, 91] also suggested constant recirculation volumes for flame holding velocities commensurate to those seen in our experiments.

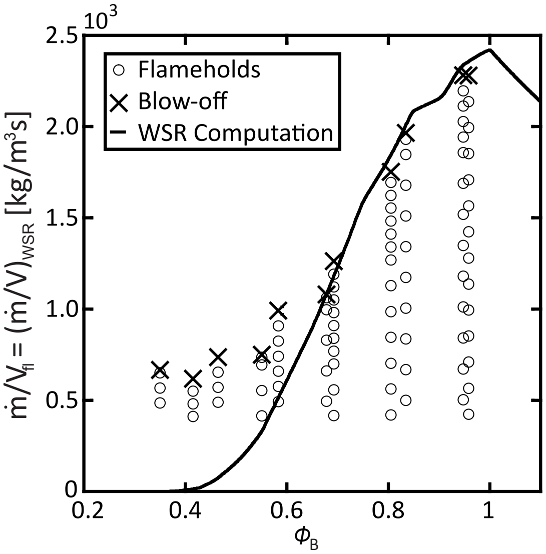

Figure 2.7: WSR results at one atmosphere for methane and air mixtures, as well as experimental flame holding results for the vitiation stage. Circles denote conditions with stable flame holding, while x's denote flame blow-off. The flame holding volume used for normalizing the burner mass flow rates was $V_{fl} = 1.13$ cm^3.

The experimental data can be recast in terms of $\dot{m}/V_{fl}$ using the determined value of V_{fl}, and compared to the computed blow-off limits of the WSR model in terms of $(\dot{m}/V)_{WSR}$, as seen in Fig. 2.7. Good agreement between the experimental and computational results can be seen for higher mass flow rates and equivalence ratios. Disagreement between the the experiments and computations at low equivalence ratios can be attributed to the low mass flow rates, and hence velocities, of the experiments. The most likely explanation for this discrepancy is the low velocity and inadequate mixing of fuel and oxidizer before the flame holder. Based on this explanation, the mixing and burning is completed downstream of the flame holder, thus resulting in bigger - non constant - volumes.

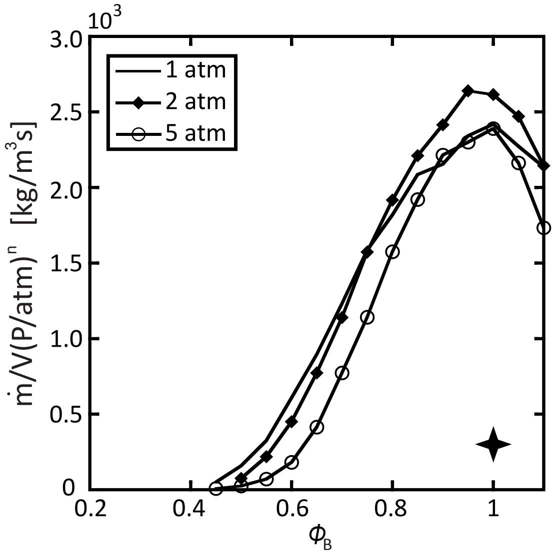

Figure 2.8: WSR blow-off results at 1, 2, and 5 atmospheres for methane and air mixtures scaled to one atmosphere using an overall reaction order $n = 1.44$. Also shown is the burner's designed operation mass flow rate, normalized by V$_{fl}$, and adjusted for pressure effects; $P = 5$ atm, $\dot{m} = 2.93$ g/s, $V_{fl} = 1.13$ cm^3, and $\phi = 1$.

Although acceptable agreement has been established between experimental and computational results at one atmosphere, our analysis needs to extend to higher pressures used for burner operation. To that end, further simulations of the WSR were performed at 2 and 5 atmospheres, representing the operational envelope of the burner. Results from all three pressure computations are shown in Fig. 2.8. The flame holding limits were evaluated using the scaling parameter $\dot{m}/VP^n$. The overall pressure sensitivity of $\dot{m}/V$ was determined numerically from the computations, giving rise to a power law P^n with a value of n approximately 1.4. This is less than the value expected for a second order reaction ($n = 2$) as a result of the detailed chemistry kinetics [99].

The approximate collapse of the computations to a scaling of the form $\dot{m}/VP^n$ lends credence to the traditional model of Longwell *et al.* [67]. It should be noted that more modern approaches may be more relevant in explaining the details of the reacting flow field within the flame holder. As already mentioned, the parameter of interest for the WSR model is the transient timescale $m/\dot{m}$ which has a direct correlation to the characteristic timescale for extinction that leads to blowoff[91]. Considering that the classic scaling of Longwell *et al.* has been used extensively in the past, and is still being used today as a guideline for combustor designs, the present study aimed at examining its applicability.

The chosen burner operational point at 5 atmospheres, as seen in Fig. 2.8, lies well within the flame holding boundaries of the vitiated burner. The present burner serves its design objectives by providing adequate flame holding at the necessary conditions, but future experiments can clearly operate at much higher mass flow rates – and/or lower pressures – or lower equivalence ratios. The design allows for flame holding at very high flow rates, and as will be seen subsequently, high pressure ratios and exit Mach numbers for the supersonic flames of interest. Future work will concentrate on these conditions, while the present study examines the feasibility of generating miniature supersonic flames.

An early approach for predicting flame holding limits was based on a one-dimensional laminar propagating flame. In a one-dimensional configuration, the mass consumption of a flame $\dot{m}$ is calculated by the equation

$$\dot{m} = \rho_u S_L A, \tag{2.2}$$

where ρ_u is the density of the reactants, S_L is the laminar flame speed, and A is the area of the flame. Laminar flame solutions for ρ_u and S_L were computed over the range of the flammability limits using full chemical kinetics. To relate the computational results with those of the experiment, a physical area, corresponding to the area of the wrapped flame, must be calculated. Figure 2.9 shows the experimental blow-off mass flow rates plotted against laminar flame results ($S_L\rho_u$) at the same equivalence ratio ϕ_B. Similar to the WSR calculations, a linear fit can be passed through most of the data at higher mass flow rates, and hence equivalence ratios. The slope corresponds to the area of the wrapped flame in the recalculations region, as it was shown in Fig. 2.4, and is approximately 64 cm^2.

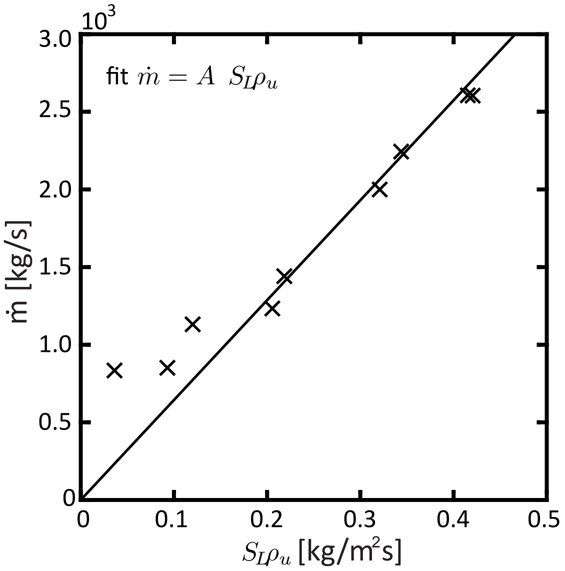

Figure 2.9: Experimental blow-off mass flow rates of the vitiation stage versus their respective laminar flame result ($S_L\rho_u$). All experiments and computations were performed at one atmosphere. The slope of a linear fit, forced to pass through the origin, serves as a measurement of flame area A. This area relates the mass flow rates measured experimentally ($\dot{m}$) to the results of the laminar flame.

Although the laminar flame method of blow-off prediction did have merit, the well stirred reactor method was ultimately chosen for pressure scaling because of the flexibility of the model. Inputs into the laminar flame only include pressure, initial temperature, and equivalence ratio, which do provide a means for controlling any timescale of the system to induce extinction. Extinction is only parametrically observed at the flammability limits for the laminar flame model. The WSR, as mentioned previously, gives enough user control to alter reactor timescales, and extinction can be induced, even at close to stoichiometric equivalence ratios. It is for this reason that the WSR was chosen as the final model for pressure scaling the blow-off limits of the reactor.

2.2.3 External flame generation

The main objective of the present work is the generation of optically accessible supersonic flames. As shown in Fig. 2.4, the output of the vitiation burner, which includes combustion products (P_V) and excess air (A_E), is combined with an additional stream of methane fuel (external F_E). The vitiated flow is hot enough to initiate reactions that result in a supersonic flame issuing from the nozzle. The amount of external fuel added is tailored to produce a variety of equivalence ratios (ϕ_E) for the external supersonic flame. In what follows we use the range of equivalence ratio (ϕ_E) from 0.59 to 1.94. As a result the supersonic flames span the range of lean to rich premixed, and also, to rich partially premixed [92] when the premixture ϕ_E corresponds to non flammable conditions (rich flammability limit ~ 1.57 [38]). In what follows, the main experimental parameters that were varied were stoichiometry and total mass flow rate issuing through the nozzle. For example, the picture inset in Fig. 2.4 shows a particular supersonic flame of ϕ_E equal to 1.3.

The laser diagnostics will be applied as near to the exit as possible, and estab-

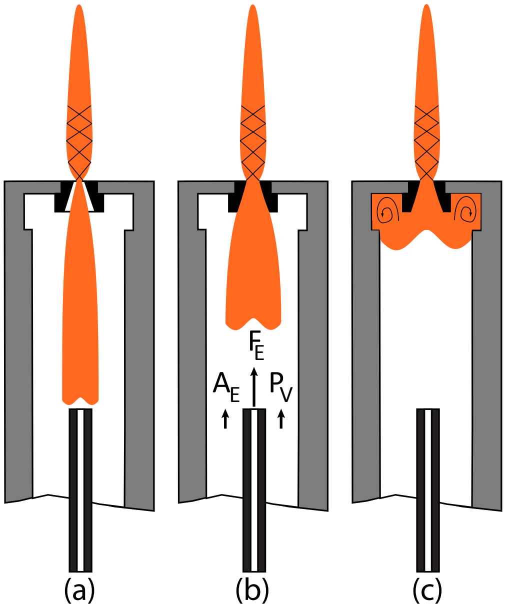

Figure 2.10: Schematic of external supersonic flame stabiliztion. Possible mechanisms include: (a) attached non-premixed flame; (b) lifted partially premixed flame; (c) premixed recirculating flame near the exit.

lish an initial condition, while downstream scans will examine the supersonic flame progress. But before this, it is imperative that we understand the mode of combustion, the manner of flame holding, as well as the phenomenology of the external flames. The flame holding of the second stage may take place in any of the three modes shown in Fig. 2.10. The first one corresponds to a classic attached non premixed flame [84, 85], where the central fuel (F_E) is diffusing radially outwards and burns at stoichiometric conditions with the vitiated products (A_E + P_V). It should be noted that in all experiments presented here, the overall equivalence ratio of the vitiated product stream was kept constant ($\phi_V \simeq 0.42$), and as a result the temperature within the burner is approximately constant, at least if one discounts the effects of the combustion of additional fuel (F_E). The large bulk velocity within the second stage ($\sim$ 15 m/s) prohibits the anchoring of a flame onto the fuel tube, and hence the non-premixed flame mode is unlikely. The second mode, shown in Fig. 2.10(b), corresponds to a lifted flame that is stabilized far from the fuel tube [85, 51]. Lifted flames are thought to be anchored either by back propagation of the partially premixed front to a stable position [14, 15], or by autoignition of flame kernels [102]. Neither of these can take place within the small confines of the second stage of the burner, which does not allow for sufficient flame lift off height [51], thus making the classic lifted flame an unlikely scenario as well. The most likely scenario to take place is presented in Fig. 2.10(c). The burner geometry provides for recirculation regions near the nozzle, and allows for additional fuel and vitiated products to mix and burn in a premixed mode due to the high vitiation temperatures. In many respects this mode is an extension of the lifted flame concept, where the recirculation streaklines act as additional lift off height for the flame.

2.3 Supersonic flames

As mentioned previously, we vary two major parameters of the external supersonic flame, namely overall mass flow rate $\dot{m}_E$ – i.e. chamber pressure – and equivalence ratio ϕ_E, and examine the overall flame phenomenology. Fig. 2.11 shows one such result of increasing overall mass flow rate $\dot{m}_E$, while keeping ϕ_E constant ($\simeq 1.94$). In all cases one can notice the formation of Mach diamonds, i.e. regions where supersonic and subsonic flows are separated by shock and expansion waves [96, p. 283]. Even at the lowest mass flow rate, the converging nozzle has a nominal exit Mach number of one, i.e. the flow is always choked. As the mass flow rate and chamber pressure increase, the overpressure at the jet exit increases and so does the level of underexpansion in the jet [44]. As a result the strength of the ensuing shock waves increases, and they become more distant. Light regions in the pictures correspond to post-shock subsonic areas where the flowfield is slow and reactions may take place, while dark regions denote supersonic flow with frozen reactions. Future

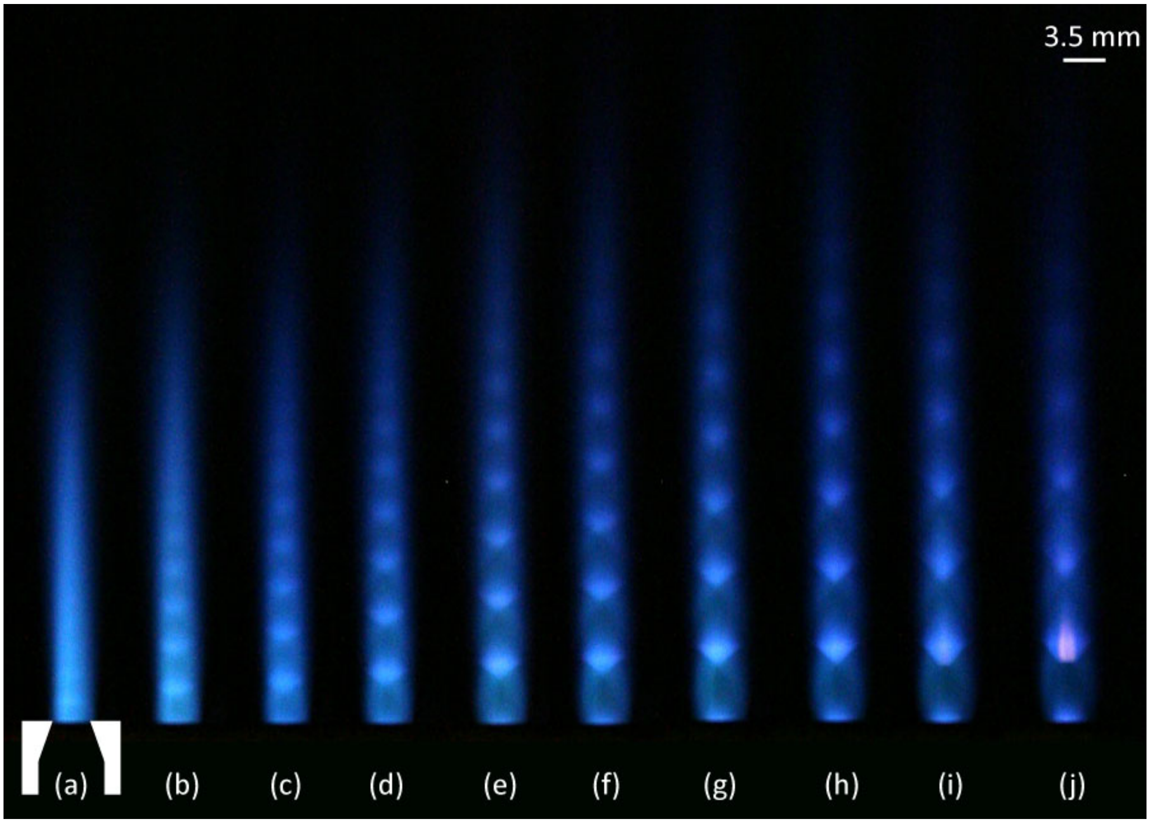

Figure 2.11: Chemiluminescence images of external supersonic flame. Equivalence ratio $\phi_E = 1.9$ corresponds to partially premixed conditions. Total flowrate increases from left (a) to right (j) and takes values shown in Fig. 2.12.

work will provide laser diagnostics measurements of the chemical composition within the flowfield. These in turn will allow us to quantify the level of burning, and identify the sources of radiation that are seen in the picture.

Figure 2.12 shows the combined results of the experimental parametric study. All equivalence ratios ϕ_E show the same trend of increasing flame length with increasing mass flow rate $\dot{m}_E$ and chamber pressure. This trend is reversed, as shown in both Figs.2.11 and 2.12, for mass flow rates above approximately 5 g/s. Also evident in Fig. 2.12 is a relationship of flame length to equivalence ratio ϕ_E for constant mass flow rate: lengths are maximum for stoichiometric flames, while both lean and rich premixtures lead to shorter flames. Both results can be explained qualitatively

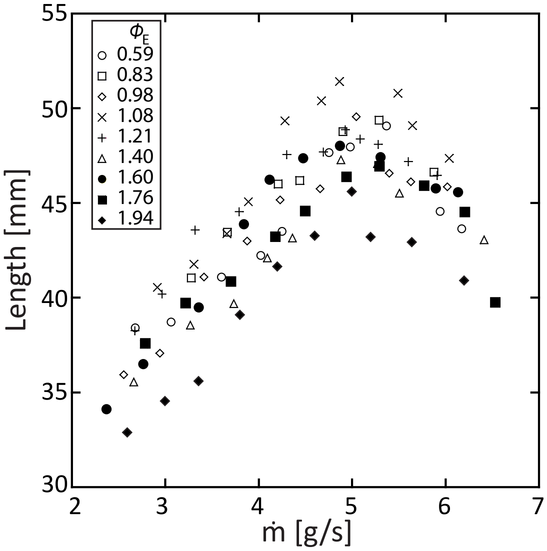

Figure 2.12: External supersonic flame lengths for different equivalence ratios ϕ_E and total mass flowrates.

as follows. Following a Lagrangian approach, we may track a reacting parcel as it moves from the recirculation within the chamber to the supersonic flow past the exit. The parcel experiences a local velocity $u(t)$ which gives rise to distance upon time integration. If the integration is carried out over the maximum chemical timescale τ_c, the resulting distance would correspond to the flame length L_{flame}.

$$L_{flame} \equiv \int_0^{\tau_c} u(t)dt \propto u_{avg}\tau_c \propto S_L\tau_c \tag{2.3}$$

It is clear from the previous description of the flow field that the flame parcel experiences a wide variety of conditions, both supersonic and subsonic, corresponding to low and high pressures respectively. If we introduce the average parcel velocity u_{avg}, the flame length may be expressed in the equation above. This fluid velocity must be related to an average flame speed S_L because the fluid parcel is continuously reacting. It is the well known relationship of flame speed to equivalence ratio [38] that leads to the observed trend of maximum flame length for stoichiometric flames.

Note that this qualitative argument assumes a constant maximum chemical timescale τ_c. This simple phenomenological explanation can be applied to the other observed trend of approximately linear increase of flame length with $\dot{m}_E$. Specifically, the average parcel velocity u_{avg} should be proportional to the mass flow rate issuing from the nozzle, leading to $L_{flame} \propto \dot{m}_E$. This trend is reversed for the highest mass flow rates, possibly as a result of flame extinction due to the high velocities and resulting strains [52].

3. RAMAN LINE IMAGING DIAGNOSTICS

3.1 Raman diagnostic system

3.1.1 Laser delivery system

The second harmonic of a Nd:YAG laser at 532nm capable of delivering pulses of approximately 0.8 J at 10 Hz was used for the Raman line imaging system. Initially, the beam is expanded by a telescope that is comprised of a negative 300-mm plano-concave and 500-mm plano-convex lens, as seen in Fig. 3.1. The result is an expansion of the beam from a 9 mm diameter to 15 mm, and a reduction in the tendency to damage components of the laser delivery system. This is particularly beneficial as any damaged optics in the laser delivery system can result in damage to the laser, and/or an extensive realignment of the system when replacing damaged components.

The enlarged beam diameter results in a tighter focus at the test section. For Gaussian beam propagation this can be seen when calculating the laser waist diameter d by the equation

$$d = \frac{2\lambda f}{D}, \tag{3.1}$$

where λ is the wavelength of the light being focussed, f is the lens focal length, and D is the beam diameter incident on the lens [26]. As it can be seen, an increase of the beam diameter D leads to a reduction of the focal spot diameter. For a 750-mm focusing lens, and a $1/e^2$ diameter equal to 15 mm, eq. 3.1 yields a 53 μm focal point diameter. As will be discussed in this chapter, the beam diameter and profile at the test section are important factors that influence the shape of the spectral signals collected by the spectrometer. A smaller beam diameter would be beneficial

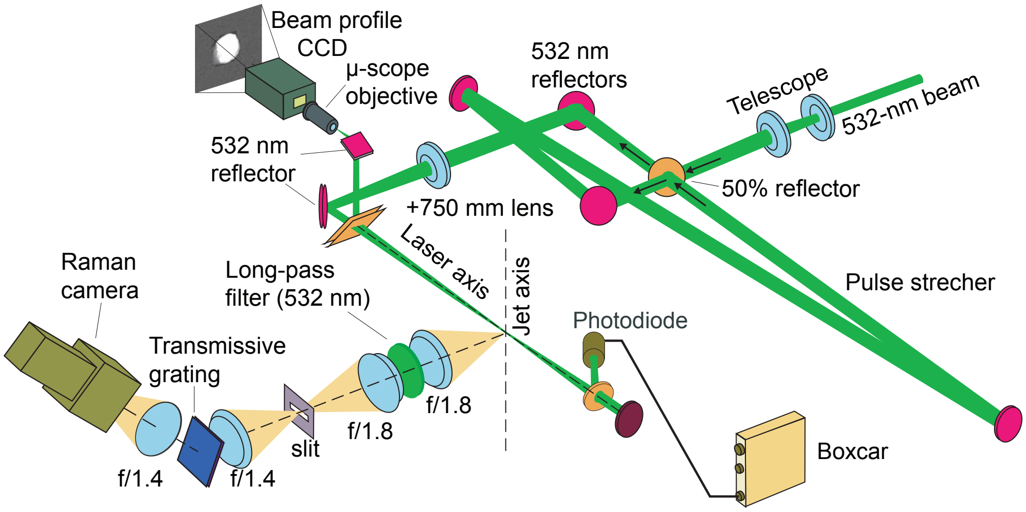

Figure 3.1: Illustration of the Raman line imaging system. Each pulse is first expanded by a Galilean telescope from 9 to 15 mm, and then temporally expanded by a 16-ft pulse stretcher. The beam is then delivered to the test section by a 750-mm focusing lens. Scattered light from the test section is collected and imaged by the Raman line imaging spectrometer.

for resolving individual species vibrational Raman signals where two species reside close to each other spectrally. In practice, the waist diameter is much larger than the one predicted by Gaussian beam propagation, and equal to approximately 195 μm.

A smaller beam focal point increases the tendency of laser-induced dielectric breakdown and plasma generation in the gas medium. The resulting spark from the breakdown process, and hence release of broadband photons, can permanently damage the camera or collected Raman data. Damage to the Raman camera can occur when an individual pixel well-depth is exceeded by the collection of a large amount of photons from the dielectric breakdown. The dielectric breakdown threshold of air for a laser pulse at 532 nm has been experimentally found to be approximately 10^{12} W/cm^2 [86]. The calculated intensity of the beam focal point, for a 9 ns pulse width, is approximately $4x10^{11}$ W/cm^2, which is less than the published value. However, the actual beam profile is not a perfect Gaussian, and regions exist with higher energy. These beam "hot spots" can have an intensity that exceeds the dielectric breakdown limit of air when focused, and ultimately result in spark generation.

To avoid exceeding the breakdown threshold we incorporate a single leg pulse stretcher, as seen in Fig. 3.1, that temporally increases the laser pulse width[57, 6, 56]. This decreases the peak power of each pulse, but allows us to maintain the total energy of the beam. The pulse stretcher is built around a 50/50 beam-splitter, with a 16 ft optical delay line. The delay line introduces approximtely 16 ns of spacing between subsequent generations of the original pulse, and results in a temporal broadening of the laser energy. The photodiode response for the original pulse seen in Fig. 3.2 would seem to indicate a full width at half-maximum (FWHM) of approximately 14 ns, and an unsymmetrical energy distribution temporally. However, the unstreched pulse is really 8-9 ns, and this error is due to the imbalance between the fast rise and long fall times of the photodiode itself (1 ns and 140 ns, respectively). The fast rise time is able to match the pulse initially, but the delayed fall time of the photodiode response slightly mischaracterizes the decay of the pulse. As seen in Fig. 3.2, the FWHM of the original pulse increases substantially to approximately 40 ns. This increase of the pulse FWHM is sufficient for reducing the possibility of optical breakdown when the beam is focused by the 750-mm plano-convex lens to an experimentally determined $1/e^2$ waist of 195 μm.

The alignment and position of the laser is monitored in real-time using a CCD camera and microscope objective, as seen in Fig. 3.1. A portion of the focused laser beam is collected from a minor reflection, and the CCD camera/microscope objective combination is positioned such that the sampled beam focuses onto the CCD. The image formed on the CCD array is representative of the main beam focal point, and is viewed continuously on a monitor. Shifts of the beam position on the order of

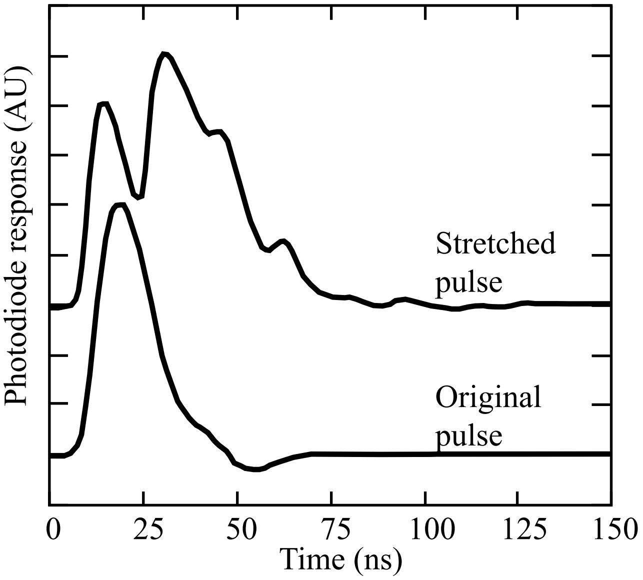

Figure 3.2: Photodiode responses of the laser pulse prior to and after the pulse stretcher. A 16-ft optical delay line introduces an approximately 16 ns delay between laser pulse generations, and can be clearly identified in the temporally stretched pulse.

the beam radius are noticeable, and can be corrected before the measurements by re-aligning the laser. Similarly, misalignments of the pulse stretcher optics are easily identified by the presence of multiple laser focal points on the beam monitor.

3.1.2 Laser energy normalization system

The main advantage of Raman scattering is the species specificity, i.e. the capability of the technique to distinguish spectrally the presence of different chemical species. Hence the collected signal energy E_i depends on species i, and E_i is directly proportional to the energy of the excitation laser E_0, which is expressed phenomenologically as

$$E_i = E_o C_i l \Omega (\frac{\partial \sigma}{\partial \Omega})_i \varepsilon, \tag{3.2}$$

where l is the length of the probe volume being interrogated, C_i is the concentration of species i in the probe volume; Ω is the solid angle defined by the first imaging lens; $(\partial\sigma/\partial\Omega)_i$ is the differential Raman scattering cross section; ε is the efficiency factor associated with the collection optics of the system; and the subscript i is the species [26].

To account for the shot-to-shot fluctuations in the laser energy E_0, as well as long term laser variation, a system to monitor and record the energy of each pulse is implemented. A photodiode samples a minor reflection of the beam that has been attenuated by neutral density filters. The photodiode response is then integrated by a boxcar averager, which holds the value for retrieval and storage by the data acquisition (NI-DAQ) system. The boxcar integration is externally triggered by the laser Q-switch, and its duration is set to a fixed time interval corresponding to the stretched pulse duration seen in Fig. 3.2. During post processing, the laser energies are used for normalization of the collected vibrational and rotational Raman data. Normalization by the laser energy reduces measurement error by accounting for single shot fluctuations of the laser, and ensures consistency between measurements in the presence of long term decay.

3.1.3 Raman spectrometer

The Raman spectrometer, seen in Fig. 3.3, and is constructed using a transmissive diffraction grating, long-pass filter, and SLR lenses. Similar transmissive spectrometer configurations are seen in industry [82, 10] as well as Sandia National Labs [9, 35]. This transmissive configuration is advantageous for Raman scattering applications, with relatively low signals inherent to the technique [26], because of the ability to operate with larger apertures and the higher throughput associated with holographic gratings. A Nikkor 85-mm $f/1.8$ lens pair form the spectrometer's first optical relay. The front collection optic was designed to operate at larger apertures, hence larger solid angle, and allows for more signal collection than traditional Czerny-Turner spectrometers.

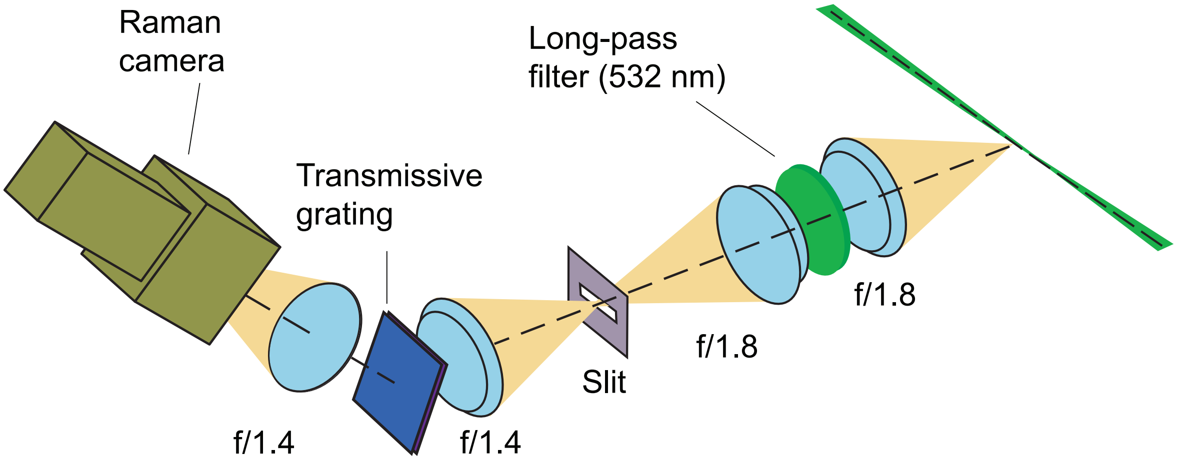

Figure 3.3: A close-up illustration of the Raman spectrometer as seen in Fig. 3.1. Scattered light from the test section is initially collected by an $f/1.8$ 85-mm optical relay. Within the collimated portion of the optical relay the light is filtered by a long-pass filter. The remaining light is then diffracted by a 1200-$lines per mm$ ($lpmm$) optical grating before being imaged onto an EMCCD camera by a pair of $f/1.4$ 35-mm lenses.

A long-pass filter is mounted in the collimated region of the first optical relay to reject Rayleigh scattered signal. The Electron Multiplying Charge Coupled Device (EMCCD) used for Raman imaging is susceptible to damage when exposed to very high signals such as Rayleigh scattering (about 10^3 times greater than Raman [61]). In order to preserve the S-branch rotational Raman signals for independent temperature measurements, a Semrock razor-edge filter is used because it allows for operation very near the Rayleigh wavelength. The nominal filter cutoff at 536 nm allows a small portion of the collected rotational Raman signal, but can be optimized by angle tuning for better performance closer to the laser wavelength, as seen in Fig. 3.4. Altering the angle of incidence (AOI) of the filter with respect to the axis of the optical relay, θ, results in a spectral shift of the filter response, and can be calculated by the equation

$$\lambda_\theta = \lambda_0 \sqrt{1 - (sin\theta / n_{eff})^2}. \tag{3.3}$$

Here n_{eff} is the effective index of refraction of the filter, λ_0 is the initial filter wavelength, and λ_θ is the shifted wavelength after angle tuning [64]. By angle tuning the filter closer to 534-nm we are able to preserve more rotational Raman signal for temperature determination, as evident in Fig. 3.4.

The effective index of refraction n_{eff} for angle tuning is dependent upon the polarization of the incident light, and will be an important factor when modeling rotational Raman spectra. Two types of polarization are possible with respect to the incidence plane formed by the light propagation direction and the filter normal vector. The polarization is referred to as P polarization when the electric field is parallel to the incidence plane, and S polarization when the electric field is perpendicular [90]. The excitation laser used in the experiments is linearly polarized, with its electric field vector oriented in the vertical direction, and thus P polarization is experienced by the filter.

A 250-μm slit at the focal point of the second 85-mm lens of the first optical relay defines the laser probe volume being interrogated. The slit accommodates the width of the beam at the waist, and prevents excessive background illumination (i.e. flame chemiluminescence) from reaching the Raman detector. A pair of Sigma 30-

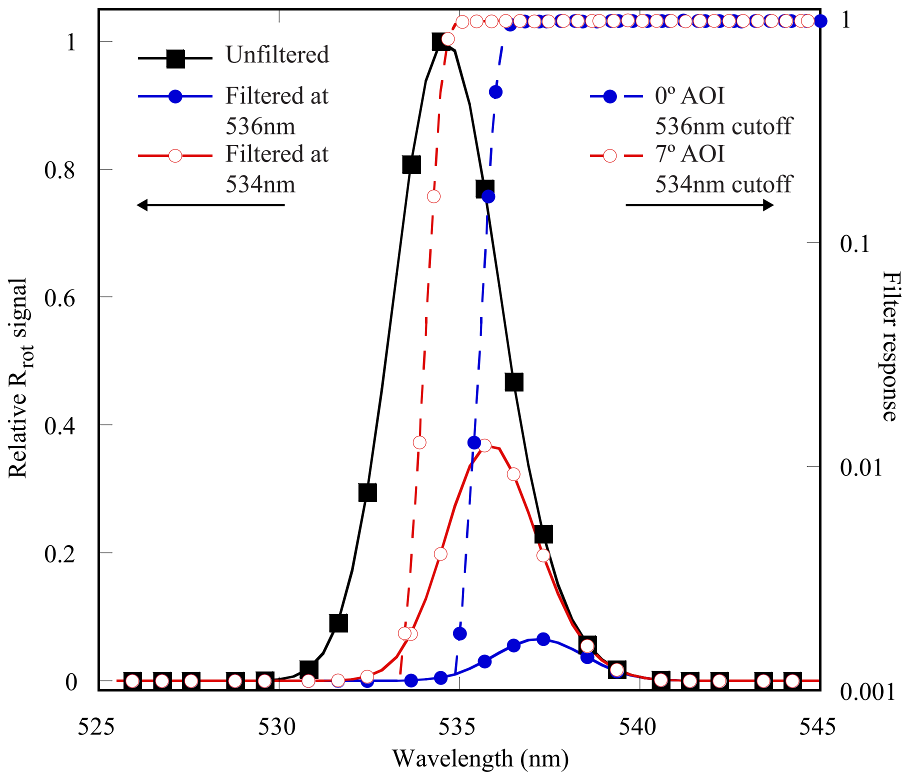

Figure 3.4: Relative rotational Raman profiles of air at STP, and response of the razor edge filter at 0 and 7^o AOI. The synthesized rotational profiles shown are for an unfiltered response, filtering at 536 nm, and then with the filter tuned at 7^o AOI to preserve more of the signal.

mm $f/1.4$ lenses form the second optical relay of the line imaging spectrometer. Dispersion of the collected signal is achieved using a holographic diffraction grating (Wasatch Photonics) within the relay, with a central (blaze) wavelength of 600 nm and a dispersion of 1200 $lpmm$. The incident and diffracted angles (θ_{inc} and θ_{diff}, respectfully) can be calculated by the equation

$$m_B \lambda = \Lambda(sin\ \theta_{incident} + sin\ \theta_{diffracted}) \tag{3.4}$$

where m_B is the Bragg diffraction order, λ is the wavelength of the incident light, and Λ is the line spacing (inverse of frequency or dispersion). When the Bragg condition is satisfied ($\theta_{inc} = \theta_{diff}$), first order diffraction at the central wavelength yields an incident and diffracted angle of 21^o. The result is a 21^o rotation of the holographic diffraction grating with respect to the optical axis to satisfy θ_{inc}, as seen in Fig. 3.3. The final relay lens and camera are inclined an additional 21^o with respect to the holographic diffraction grating to capture the central wavelength at θ_{diff}, for a total of 42^o.

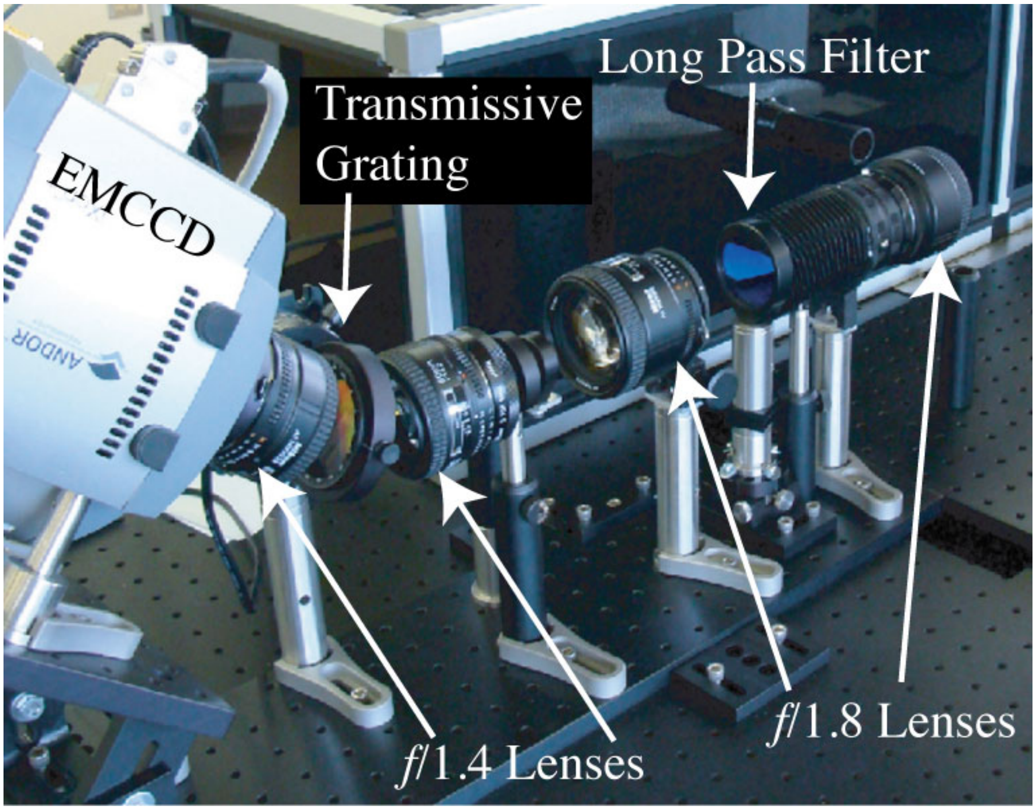

Figure 3.5: A image of the constructed spectrometer prior to light-tight enclosure.

The EMCCD images the dispersed signal, and has an exposed focal plane array of 512 by 512 square pixels, each16 μm in size. The horizontal axis of the spectral image formed on the detector corresponds to physical space along the laser, and the vertical axis yields the spectral distribution of the collected signal. Figure 3.6 shows the resulting vibrational Raman signals of O_2 and N_2 in ambient air at STP, as well as their combined rotational Raman signal. Curvature of the spectral lines is attributed to symmetry breaking of the optical axis at the transmissive grating, and has also been exhibited in similar transmissive-grating spectrometers [103, 35].

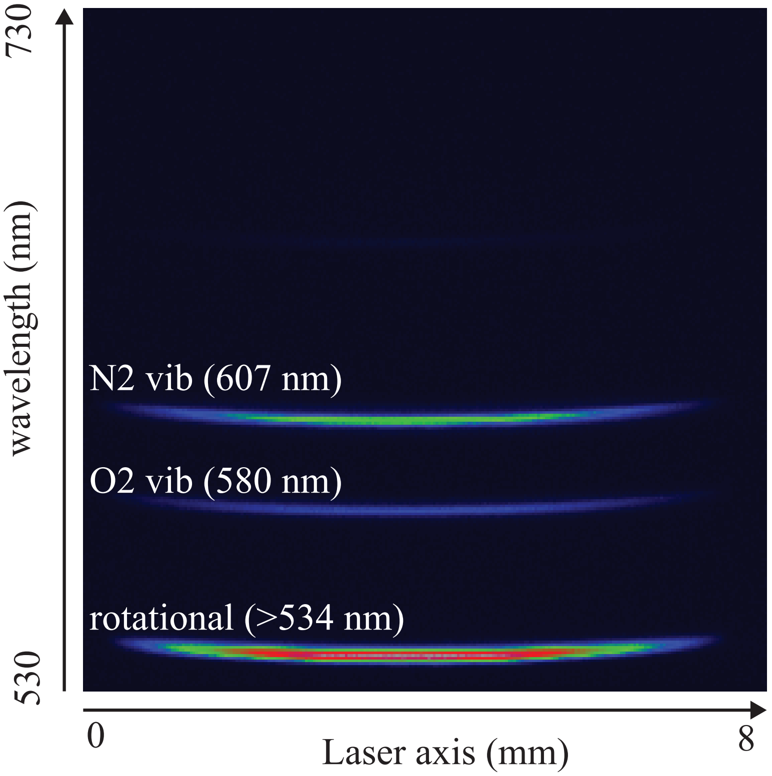

Figure 3.6: Spectral image formed on the EMCCD for air at STP conditions. The N_2 and O_2 vibrational lines, as well as their combined rotational response are indicated.

The theoretical dispersion of the spectrometer can be calculated using a thin lens approximation for the final focusing lens, and ray tracing from the lens to the focal plane array (FPA). First, the thin lens approximation is applied to the lens between the transmissive grating and EMCCD, and in matrix form is given by the equation

$$\begin{bmatrix} \rho_2 \\ \theta_2 \end{bmatrix} = \begin{bmatrix} 1 & 0 \\ -1/f & 1 \end{bmatrix} \begin{bmatrix} \rho_1 \\ \theta_1 \end{bmatrix}, \tag{3.5}$$

where ρ is the distance of the ray from the optical axis; θ is angle the ray makes with the optical axis; f is the focal length of the lens; and the subscripts 1 and 2 represent the state of the ray prior to and after interaction with the lens, respectfully. The parameter θ_1 is wavelength specific because of the dispersion that occurs prior to the lens, and is calculated using the diffraction angle given by eq. 3.4. Based on the geometry of the diffraction grating and final focusing lens, θ_1 is the difference between the diffraction angles of the wavelength being calculated and central wavelength ($\theta_{diff(\lambda)}$-$\theta_{diff(600nm)}$). Finally, ray tracing through a uniform medium is applied to calculate the physical distances between wavelengths on the FPA, and is given by the equation

$$\begin{bmatrix} \rho_3 \\ \theta_3 \end{bmatrix} = \begin{bmatrix} 1 & d \\ 0 & 1 \end{bmatrix} \begin{bmatrix} \rho_2 \\ \theta_2 \end{bmatrix}, \tag{3.6}$$

where d is the distance traveled by the ray to the FPA; and the subscript 3 indicates the state of the ray at the FPA, with $\rho_3 = 0$ corresponding to the midpoint on the array. For the thin lens approach, the distance d is equivalent to its focal length f.

The O_2 and N_2 vibrational Raman transitions are used to calculate the dispersion of the spectrometer because their wavelengths are well known (580 and 607.3 nm, respectively), and they can be easily measured by the laser diagnostics system for verification. In fact, 'positioning' the N_2 and O_2 vibrational lines onto the FPA is a part of the every day calibration procedure for the system. Using the given parameters of the system, and eqs. 3.4, 3.5, 3.6, the theoretical distance between the two wavelengths on the FPA is calculated to be 1.05 *mm*. This yields a theoretical dispersion of 26 *nm*/*mm* on the FPA, and is comparable to the experimentally determined value of 25.1 *nm*/*mm*. The 3.5% error can be attributed to the thin lens approximation that was applied to relatively thick SLR style lenses. An initial spectrometer configuration utilized a pair of Nikor 55-*mm* $f/1.4$ lenses for the second optical relay, and provided a dispersion of 15.1 *nm*/*mm*. Although these lenses were capable of producing spectra, the reduced dispersion eliminated the possibility of capturing all species signals on the same FPA, namely the H_2 vibrational Raman signal.

3.1.4 EMCCD

A back illuminated EMCCD (Andor iXon 897) was chosen for the experimental setup because of key features that help increase the signal-to-noise ratio (SNR). These features include (1) quantum efficiency∼93%, (2) frame transfer capability, (3) on chip pixel binning, (4) thermoelectric cooling, and (5) electron multiplication (EM) amplification. For any FPA the SNR is defined as

$$SNR = \frac{SQ}{\sqrt{SQ + \dot{B}Q\tau + \dot{D}\tau + N_{read}^2}} \tag{3.7}$$

where S is the collected signal, Q is the quantum efficiency of the camera, $\dot{B}$ is the collected background signal, $\dot{D}$ is the dark current, τ is the exposure time, and N_{Read} is the readout noise [71]. The signal term S is not given a time rate dependence due to the short lifetime of Raman scattering ($\sim 10^{-11}$ s [25]) relative to the minimum exposure of the camera (10^{-5} s). The background and dark current noise terms are continuous signals, and are integrated on the detector pixels during acquisition time τ, hence their contribution is written in a time dependent form ($\dot{B}Q\tau + \dot{D}\tau$).

Applications with large amounts of signal that overcome the noise terms become shot-limited, and the SNR can be described by Poisson statistics as $SNR = S^{1/2}$. Low level techniques such as incoherent Raman, however, are not afforded this advantage, and must rely on the capabilities of the imaging chip in order to increase the SNR.

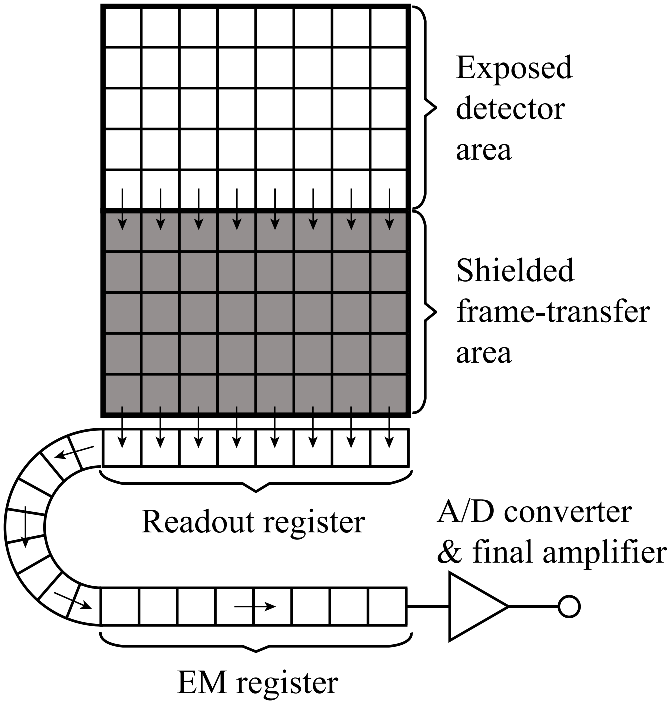

Figure 3.7: Schematic of a CCD array with frame transfer capability, and EM amplification register.

Frame transfer capability is achieved with a shielded array, adjacent and identical to the one used for imaging, that receives the collected signal immediately after acquisition, as seen in Fig. 3.7. Once the image acquisition and transfer processes are complete, the pixels no longer accumulate background signal, and the readout process begins. Read noise injected during the analog to digital (A/D) conversion is strongly dependent upon the read rate [24], and is minimized when using the slowest rate available. Slow readout rates, however, result in a prolonged exposure time (τ), and a consequent increase in background signal, for detectors without frame transfer capability.

This compromise is avoided when operating with a frame transfer capable chip that can operate on two independent shift clocks. The time necessary for transferring the charge completely to the secondary array is dependent upon the vertical shift clock of the array. A vertical shift durration of 0.5-μs per transfer, like the one used in the actual experiment, yields a transfer time of approximately 256-μs necessary for transferring all 512 rows of the exposed array. Once the charge has been transferred to the shielded array, a slower read clock can be used for the A/D conversion. Finally, the presence of the fast vertical shift clock suppresses the background and thermal noise terms by reducing τ in Eq. 3.7. This is done without the need for complicated mechanical shutters like the ones used in other studies [75, 8, 52]. The presence of a second, slow readout rate suppresses the readout noise term directly (N_{read} in Eq. 3.7).

Back illuminated CCD arrays yield a higher quantum efficiency when compared to commensurate front illuminated arrays, but typically exhibit higher amounts of dark current [81]. Typical values for front-illuminated arrays range from 20-60%, while the back-illuminated detecttors can reach values close to 100% (in the present study: 93%). As can be seen in Eq. 3.7 the quantum efficiency has a direct effect on SNR, and for this reason multiscalar measurement techniques utilize back-illuminated detectors almost exclusively. This noise contribution source is extremely temperature dependent, and can be reduced by cooling of the detector array [46]. Thermoelectric cooling, with additional liquid cooling support, is used to achieve detector temperatures as low as -100^oC, and effectively minimizes the dark current contributions (the

$\dot{D}$ term in Eq. 3.7).

Hardware pixel binning yields an effective reduction of noise per pixel by summing the collected charge of grouped pixels prior to A/D conversion. Thus, read noise is injected only once for the pixel grouping, rather than for each individual pixel. A posteriori software pixel binning cannot achieve the same level of noise reduction as hardware pixel binning, because the read noise has already been incorporated into the recorded value of photons (counts) for every pixel. Pixel binning of a specified number of pixels (M) sums up all the charge collected by the pixels, including any background signal $\dot{B}$ and thermal dark noise $\dot{D}$ contributions. Examining eq. 3.8, M is a multiplication factor that would be applied to all terms except N_{Read}^2. Therefore, we can suppress read noise contributions and make the term negligible by hardware binning large groups of pixels on the detector. This, of course, comes at the expense of spatial resolution.

$$SNR = \frac{MSQ}{\sqrt{MSQ + M\dot{B}Q\tau + M\dot{D}\tau + N_{read}^2}}, \tag{3.8}$$

Further read noise suppression is achieved by EM amplification prior to A/D conversion. An EM register, positioned between the readout register of the array and the final A/D converter, performs the signal multiplication over many individual stages that generate new electrons by the process of impact ionization [24, 81, 49, 48]. Higher voltage amplitudes applied at the EM register generate more electrons, and result in higher amplification [49, 48]. The result is an overall gain, G, of the signal passed through the EM register. Read noise is not amplified because the EM register is placed before the A/D converter that injects the readout noise. This configuration suppresses the readout noise, indirectly, by increasing every other term in the SNR equation (Eq. 3.9) except N_{read}. However, the EM gain process amplifies all signals that are processed through the register, including background and dark noise contributions.

The combined effect of the EM gain and pixel binning can be seen in the modified SNR equation,

$$SNR = \frac{GMSQ}{\sqrt{GMSQ + MG\dot{B}Q\tau + MG\dot{D}\tau + N_{read}^2}}, \tag{3.9}$$

where the factors M and G are shown multiplying the relevant terms. When substantial EM gain is applied during readout, and large amounts of pixels are binned together on the chip, the read noise term N_{read} essentially becomes negligible when compared to the other terms. If the dark current is effectively removed by thermoelectric cooling, and the background signal is minimized by the fast frame transfer, the EMCCD can provide an SNR that effectively scales as

$$SNR = \sqrt{GMSQ}. \tag{3.10}$$

Therefore, the EMCCD is the first detector that can operate in a shot-limited fashion, even for extremely low light levels. When this type of detector was first coming into production, experiments could be carried out with photon counting using a planar array, without an intensifier, like the one that can be found in reference [73].

3.1.5 Hardware pixel binning

On-chip hardware pixel binning provides a means of increasing SNR by rendering injected noise at A/D conversion negligible, as previously discussed. The hardware architecture of EMCCD arrays poses limitations on the means by which hardware binning can occur. Vertical binning on an EMCCD array, as shown in Fig. 3.7, occurs at the readout register beneath the shielded transfer array. Multiple rows of pixels can be effectively summed up, in the vertical direction, by transferring their charge onto the readout register all at once. This places the restriction that channels of binned pixels across the width of the EMCCD must be the same height.

As seen in Fig. 3.6, the spectral image formed on the FPA exhibits strong curvature due to the symmetry breaking introduced in the optical axis. This in turn increases the complexity of applying hardware binning. Custom pixel binning schemes cannot be developed that conform to the curvature of the of the signals due to the restriction of the detector architecture. Large pixel binning schemes that encompass the curvature of the entire spectral line will integrate erroneous contributions to background noise. Conversely, it is not advantageous to use smaller pixel binning schemes and perform software pixel binning, since this approach would be detrimental to the SNR, as previously discussed. Rather, a hybrid between large and small vertical pixel binning is used, as shown in Fig. 3.8. Large vertical pixel groups capture the main portion of the Raman signals, while smaller pixel groups are combined with software binning to account for curvature effects where necessary. It should be noted that pixel binning in the horizontal direction is always performed in 16-pixel groups across the detector, corresponding to a horizontal resolution of 256 μm. Following the usual convention [6], the pixels that are hardware-binned (on-chip) are called ‘superpixels’.

Gas mixture calibrations were carried out to map the curvature of each individual species, as well as examine the cross-talk interactions between CO_2 & O_2, as well as CO & N_2. The calibrations were carried out at atmospheric conditions using known mixtures of gases, and included the species CO_2, O_2, CO, N_2, and CH_4. Vibrational Raman spectra for H_2O and H_2 were synthesized using RAMSES, and an estimation of the field curvature was provided by the rotational Raman line.

High resolution spectral images (2x2 pixel binning) of the calibration gases were

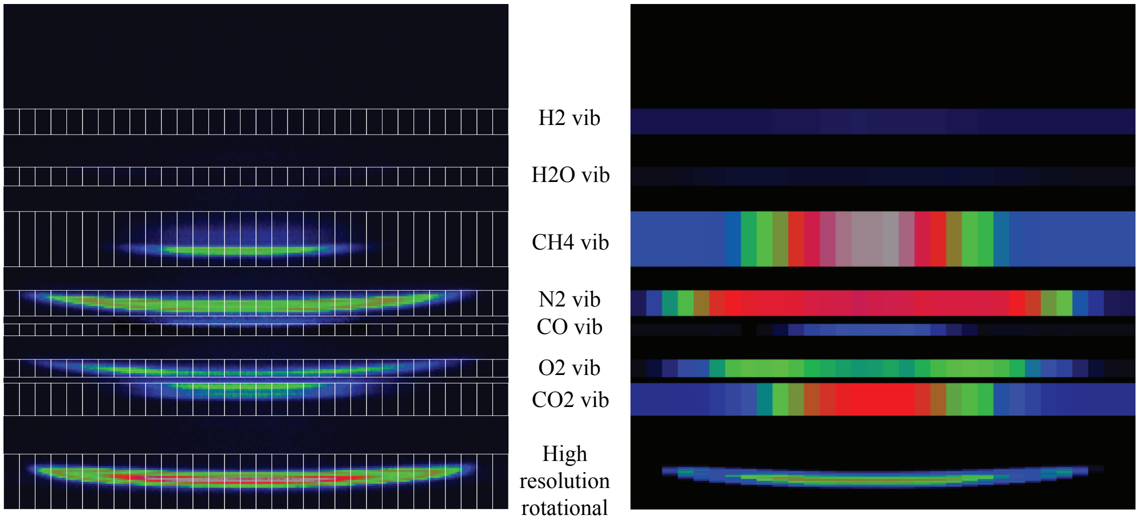

Figure 3.8: Composite spectral image showing species CO_2, O_2, CO, N_2, and CH_4. The hardware pixel binning configuration used for experiments is applied to the composite image. The species vibrational channels, as well as their combined rotational signals are noted in the figure.

collected and averaged together to examine the extent the various species, as seen in Fig. 3.8(a). The curvature of the spectral lines extends upwards as much as 12 pixels from the center of the FPA to the periphery. Measurements will take place within a limited region close to the center of the FPA, as will be discussed in the next two sections. Within the measurement region, the curvature is smaller, and extends upwards only 2 pixels from the central value. Superpixels for the vibrational Raman lines were formed to capture the the spectral width of the signals within the region of interest. At the periphery, portions of the vibrational signals are not captured by their respective superpixels, and are collected using adjacent superpixels that are smaller in size (higher resolution). The adjacent pixels are binned in software with the main superpixel during post-processing. The result of the superpixel scheme can be seen in Fig. 3.8(b).

Cross-talk interactions between the vibrational/rotational spectra of CO_2 & O_2

as well as CO & N_2 increases the difficulty of the technique, even in the absence of curvature. The R_{vib} signals of the paired species overlap spectrally due to the closeness of their Raman vibrational frequencies, and the presence of rotational lines that broaden the observed spectra. As a results it is difficult to identify the signal contributions of each species, as can be seen in Fig. 3.9. A matrix inversion technique has been used in similar experiments in the past [6], and is capable of discerning the spectral contributions in the crosstalk region. The technique requires extensive calibrations, is computationally intensive, and requires additional instrumentation. To avoid the complexities of this technique, high resolution pixel binning is performed between the main superpixels of the crosstalk pairs. Curvature of the crosstalk is captured by the high resolution region between the main superpixels of the species. When the two neighboring species are present, the contributions to each are calculated by finding the local minima of the signal within the crosstalk region. The pixel where the minima resides is treated as the 'dividing line' between the two species, and the signal within the high resolution crosstalk region is split at this pixel location. The signals within the cross talk region are then combined with the main superpixel of their respective species. Due to superpixel binning, little spectral information is available within the crosstalk region to perform complex analysis of the spectral profile decays. However, a compromise between improved SNR and crosstalk calculation must be made, and thus the simplified method will suffice for the purpose of this work.

The rotational Raman signal is captured with vertical binning of 2 pixels to preserve as much of the rotational profile as possible. Methods in which temperature can be extracted from the rotational signal include using the signal integral, the location of the profile maximum, or examining the decay of the profile. These methods are proposed theoretically in the work by Kojima and Nguyen [57], which measured

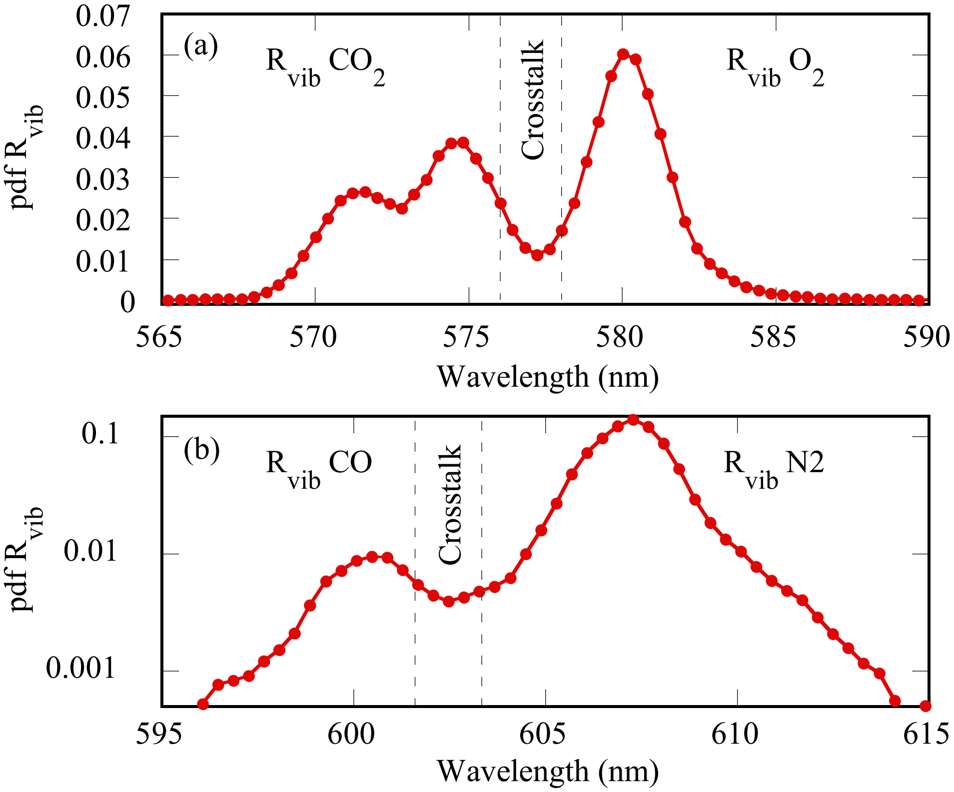

Figure 3.9: Crosstalk regions for the two pairs of neighboring species are shown. (a) The vibrational crosstalk region for species O_2 and CO_2 is shown from experimental data with an O_2-to-CO_2 molar ratio of 1.9:1. (b) The vibrational crosstalk region for species N_2 and CO is shown from experimental data with an N_2-to-CO ratio of 15:1. High resolution spectra correspond to single pixel resolution in wavelength space (0.4 $nm/pixel$) and 256 μm in physical space.

temperature in a constant (elevated) pressure environment using the intensities of highly resolved rotational lines. The technique can overcome the use of smaller superpixels because of the larger differential scattering cross-sections associated with rotational Raman scattering. Two of the three techniques are used in the current experiment, names the integral and maximum location methods. The integral technique would benefit greatly from larger superpixel binning over the rotational signal, but would lose all information pertaining to the detailed signal profile. Therefore, minimal superpixel binning is used for the rotational signal, and the integration of the profile will be performed in software during post-processing.

3.2 Vibrational Raman density measurements

Vibrational Raman scattering for density measurements has been widely used in the past, mostly because of its inherent species sensitivity [9, 6, 37, 40, 17, 78, 36, 79, 4]. The details of the Raman spectroscopy are beyond the scope of the present works, and can be found in Reference [26]. The technique is based on the integrated signals of the Raman vibrational Q-branch transitions of all major species present within the laser probe volume, and can directly measure species concentrations. Vibrational Raman scattering occurs when the vibrational level (denoted by the corresponding vibrational quantum number v) of a molecule changes due to the excitation/de-excitation that takes place during the inelastic Raman scattering process. The selection rules of quantum mechanics allow the vibrational level to change by $\Delta v = -1, 0$, or 1, however the Stokes (Q-branch) transitions used for density measurements occur when $\Delta v = 1$. Stokes scattering is utilized for the incoherent technique because of the relative strength of the red-shifted signal. The blue-shifted, anti-Stokes Raman scattering ($\Delta v = -1$) is quite weak for low temperatures. At high enough temperature (approximately 2600 K for N_2) the anti-Stokes Raman becomes stronger than the Stokes contribution, and the present technique be revised [61].

$$E_i = E_o C_i l \Omega (\frac{\partial \sigma}{\partial \Omega})_i \varepsilon, \tag{3.2}$$

Equation 3.2 shows a phenomenological formula that predicts the Raman energy collected on the detector. The formula applies equally to both vibrational as well as rotational Raman scattering, and the sensitivity to the type being examined enters the equation through the differential scattering cross section $(\frac{\partial \sigma}{\partial \Omega})_i$. The parameters ε, l, and Ω are parameters of the spectrometer that are constant throughout the experiment, and the pulse energy E_0 is continuously recorded as previously discussed. When the parameters of the system are known, or assumed constant, the collected Raman signal $\mathrm{E}_{vib,i}$ becomes a function of the concentration C_i.

3.2.1 Vibrational slit function

The system parameters are measured before data collection using ambient condition calibrations. The E_{vib} signal for N_2 in ambient air is used to calculate the system parameters because of its abundance and strong signal at Standard Temperature and Pressure (STP) conditions. Ambient calibrations measure the term $E_{vib,N2}$ across the width of the detector, while the laser energy E_0 is measured simultaneously. Division of the energy collected in each superpixel $E_{vib,N2}$ by the measured laser energy, C_{N2} at STP, and Raman differential scattering cross section $(\frac{\partial\sigma}{\partial\Omega})_{vib,N2}$ yields the constant system parameters, as shown in

$$l\Omega\varepsilon = \frac{E_{vib,N2,STP}}{E_o C_{N2,STP}(\frac{\partial\sigma}{\partial\Omega})_{vib,N2}} \equiv E_{vib,N2}\ slit\ function. \tag{3.11}$$

One-dimmensional measurements of the system parameters, taken across the width of the detector, form the vibrational slit function, and are seen in Fig. 3.10. It is assumed that the same slit function can be applied to all vibrational Raman signals collected, and that the system parameters are constant and invariant for all the species signals collected at the same horizontal superpixel.

In effect, we assume that the vibrational slit function is only a function of space variable, or superpixel number. From Fig. 3.10 it is immediately noticeable that the vibrational slit function is not constant across the detector. Two factors that affect the slit function are the shape of the focused laser with respect to the spectrometer slit, and vignetting due to the optical system. Shown at the top of Fig. 3.10 is an illustration of the shape and size of the focused laser with respect to the slit

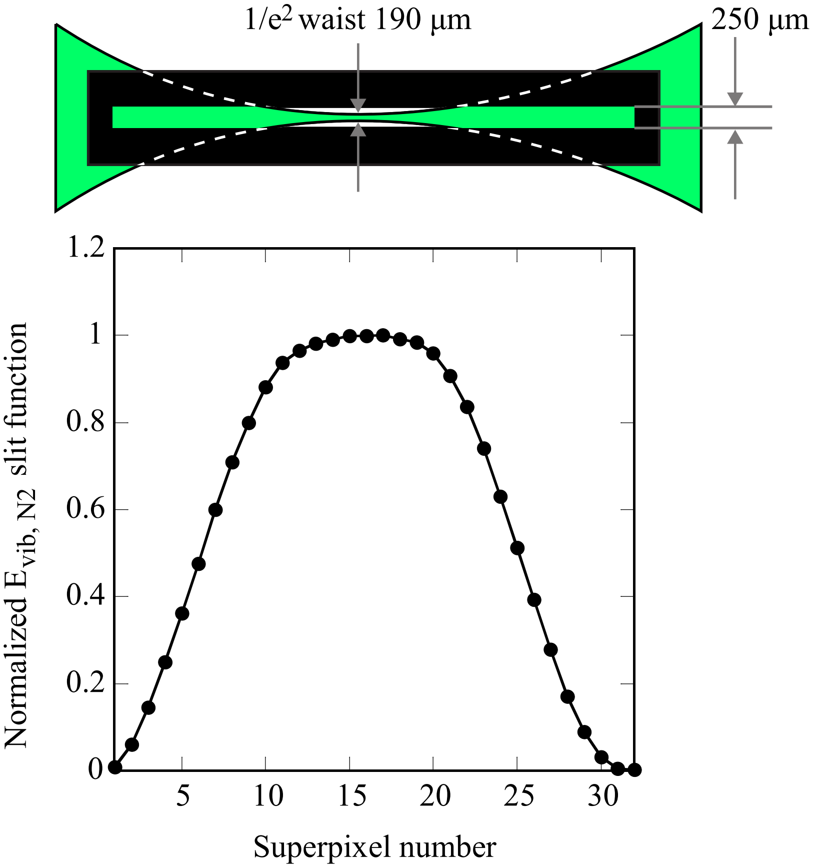

Figure 3.10: The N_2 vibrational Raman slit function, normalized by the maximum value. The illustration above the slit function shows how the fixed width of the slit and varying size of the laser give rise to the shape of the slit function.

within the spectrometer. Light scattered by the laser undergoes a 1:1 conjugation at the first optical relay of the spectrometer, and is focussed onto a 250-μm slit. The laser waist is easily admitted through the slit since the waist diameter $(1/e^2)$ of 190 μm is smaller than the slit width of 250 μm. At the same time, the varying size of the laser due to focusing and defocusing causes portions of the scattered signal to be rejected by the slit, since the laser diameter exceeds 250 μm in size in these locations.. Measurements are not restricted to the portion of the slit function where the laser is completely admitted, but rather can be extended by several superpixels in both directions by proper characterization of the slit function. The measurements at these extended points, however, come at the expense of reduced SNR due to signal attenuation.

Signal attenuation at the periphery (edge of the slit) is also attributed to vignetting within the spectrometer optics. Vignetting is a common problem with the Sigma 30-*mm* $f/1.4$ lenses used in the present study, but occurs at the far edges of the detector when the lenses are at maximum aperture, as was the case here. The effect does place limitations on rotational Raman signals (E_{rot}), which will be discussed in the next section, but it also has detrimental effects on vibrational signals at the top of the detector. A broadband light emitting diode (LED) and band-pass filters were used to examine the extent of vignetting for species with vibrational signals at longer wavelengths, namely H_2O and H_2 at 660.5 and 683 *nm*, respectively. Figure 3.11 shows the superimposed results obtained with 600-*nm* and 700-*nm* band-pass filters, each with a 10-*nm* transmission FWHM. The results were filtered by a threshold function to examine the limits of light acceptance imposed by vignetting. The signal collected at 700 *nm* exceeds the wavelengths necessary to capture H_2O and H_2 vibrational, as shown in Fig. 3.11. On this basis, it is safe to conclude that vignetting is negligible in the vibrational signals collected within the central part of the detector. Since measurements utilized only a portion of the detector from 1 *mm* to 7 *mm*, we may conclude that vignetting does not affect the vibrational Raman technique substantially.

3.2.2 Density and mole fraction calculations

Density calculations are performed for every species using the same vibrational slit function. The collected signal of each species is first normalized by the laser energy collected by the laser energy normalization system (E_0). Shot-to-shot fluctuations

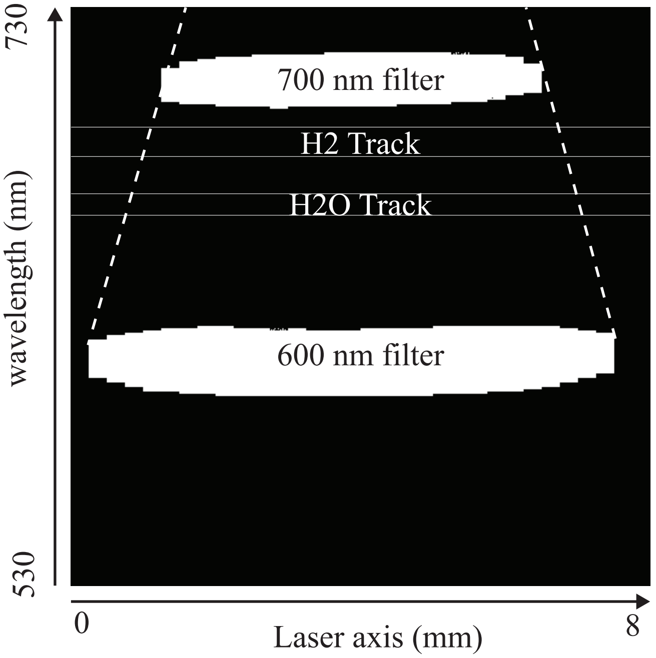

Figure 3.11: Vignetting spatial limitations were examined with 600 and 700-nm band-pass filters. The thresholded results show the spatial limitats where water and hydrogen vibrational Raman signals can be captured.

and long term decay of the laser energy may result in significant error contributions to the data processing. Normalization by the laser energy for each laser shot, prior to averaging, mitigates these effects, and reduces the error of the measurements. Figure 3.12 shows sample vibrational Raman data for air at STP, and lean combustion products from a supersonic jet. The $\mathrm{E}_{vib,N2}$ signal from Fig. 3.12(a) is used to calculate the vibrational slit function based on the known concentration of N_2 at STP conditions, and differential scattering cross section. The species signals shown in Fig. 3.12(b) are already normalized by the energy of the laser, and therefore are representative of

$$\frac{E_{vib,i}}{E_o} = C_i l \Omega (\frac{\partial \sigma}{\partial \Omega})_{vib,i} \varepsilon. \tag{3.12}$$

For each species i, Eq. 3.12 is then normalized by its respective differential scattering cross section,

$$\frac{E_{vib,i}}{E_o(\frac{\partial\sigma}{\partial\Omega})_{vib,i}} = C_i l\Omega\varepsilon. \tag{3.13}$$

Calculation of concentration (i.e. number density) is achieved by dividing the Eq. 3.14 by the vibrational slit function ($l\Omega\varepsilon$), which is calculated based on known ambient conditions (Eq. 3.11)

$$C_i = \frac{E_{vib,i}}{E_o(\frac{\partial\sigma}{\partial\Omega})_{vib,i}(l\Omega\varepsilon)}. \tag{3.14}$$

For each species this calculation is performed for each superpixel along the laser axis, as it was seen in Fig. 3.10 that the vibrational slit function varies across the width of the detector.

The vibrational differential scattering cross sections used for density measurements at 532-nm, as well as vibrational frequency, are shown in Table 3.1,[45] as found in [26]. The values for 532-nm were calculated from the original tabulated values at 337-nm by applying a frequency scaling that follows (ν_0 - ν_k)^4, where ν_0 is the laser frequency and ν_k is the vibrational frequency of the molecule [26]. As shown in Fig. 3.8, both CH_4 vibrational frequencies are binned together into the same hardware superpixel because of their close proximity, and therefore both differential scattering cross sections are summed up when calculating the concentration. The same situation also occurs for the ν_1 and $2\nu_2$ vibrational frequencies of CO_2, and thus the two vibrational transitions are integrated on the imaging chip as well.

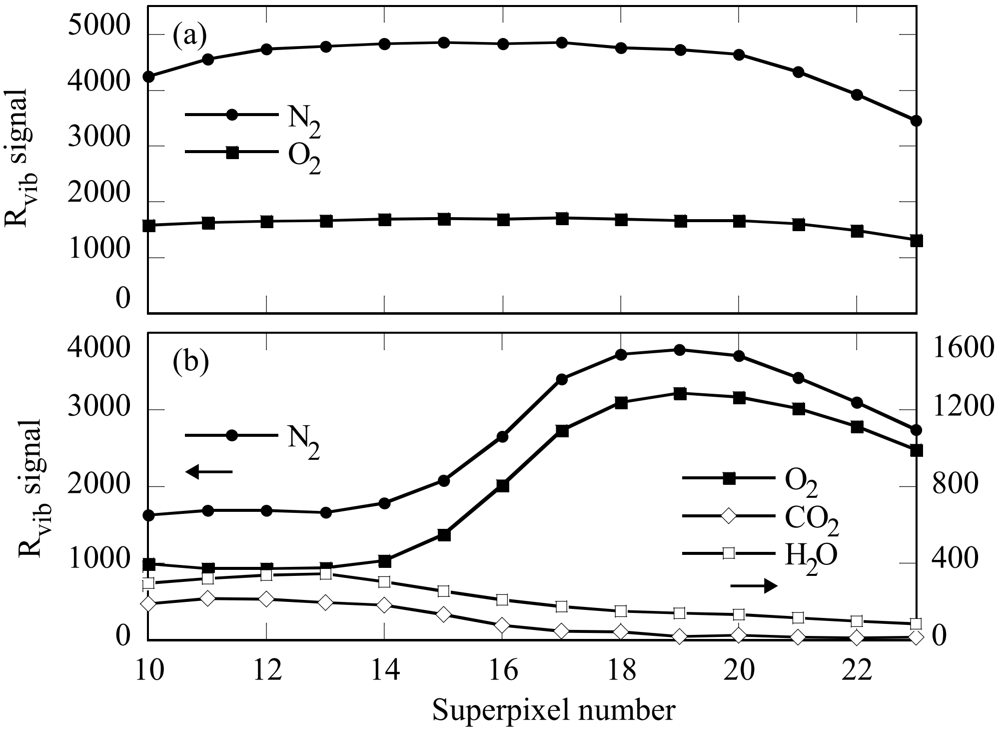

Figure 3.12: Vibrational Raman signals for (a) ambient air at STP conditions, and (b) hot vitiation combustion products. The data shown here have been energy normalized and averaged over 100 shots.

Table 3.1: Vibrational differential Raman scattering cross sections and frequencies for the major species of combustion.

Species	Vibrational differential scattering cross section (10^{-30} cm^2/sr)	Vibrational frequency (cm^{-1})
N_2	0.46	2330.7
H_2	0.943	4160.2
O_2	0.65	1556
CO	0.48	2145
CO_2, ν_1	0.6	1388
$CO_2, 2\nu_2$	0.45	1285
CH_4, ν_1	2.6	2915
CH_4, ν_3	1.7	3017
H_2O	0.9	3657

The concentrations of the combustion species show in Fig. 3.12(b) are calculated using the differential scattering cross sections listed in Table 3.1, and are shown in Fig. 3.13(a). Mole fractions of each species X_i can be calculated simply by the equation

$$X_i = \frac{C_i}{\sum_j C_j}, \tag{3.15}$$

and are shown in Fig. 3.13. The mixture molecular weight (MW_{avg}) and fluid density (ρ) at each point along the laser axis are then calculated using the equations

$$MW_{avg} = \sum_i X_i MW_i, \tag{3.16}$$

$$\rho = MW_{avg} \sum_i C_i, \tag{3.17}$$

where MW_i is molecular weight for species i. Signal to noise ratios and errors for various species signals are discussed with the results of both not reacting and vitiated flow measurements. The SNR is directly proportional to the number density of the species being measured, thus SNR and error will vary greatly depending on the flow being interrogated.

3.3 Rotational Raman for temperature measurements

Temperature measurements can be performed with the previously discussed vibrational density technique, however it relies on the assumption of known constant pressure [89] and cannot be applied to non-isobaric flows. The S-branch rotational Raman signals are used for independent measurements of temperature along the laser axis. Previous temperature measurements that utilize the S-branch rotational Raman signals have been based on the intensities of individual transitions [100, 65, 22, 21, 30], the slope of the spectral decay [59], and the band width of the

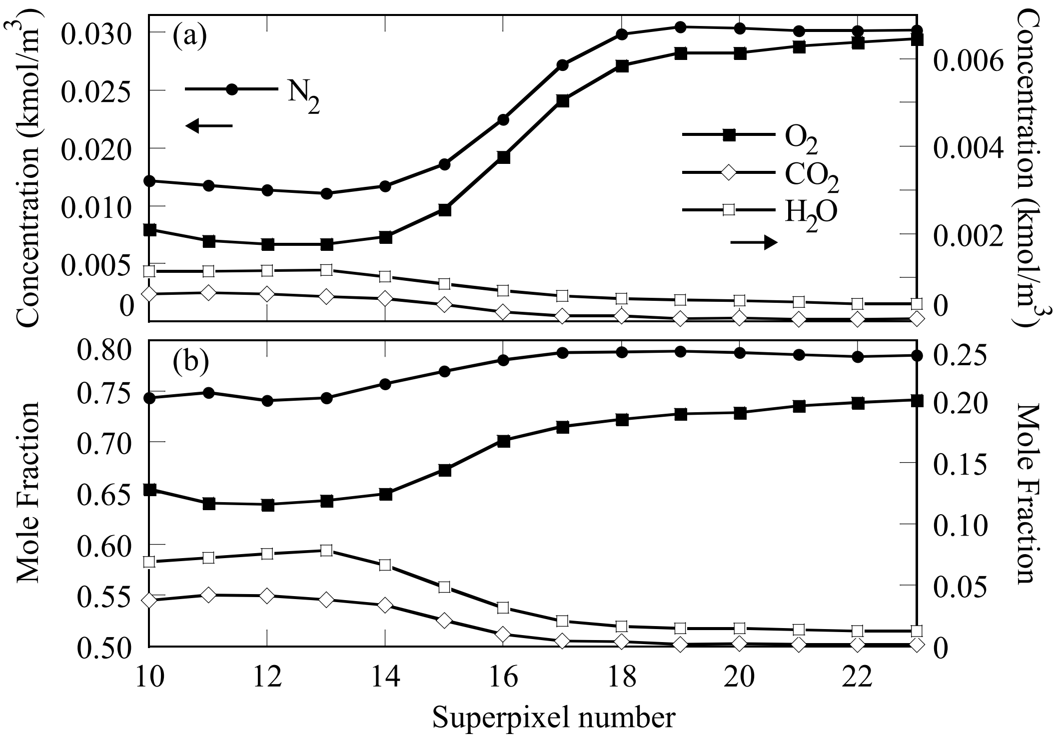

Figure 3.13: (a) Calculated vitiation product concentrations from Fig. 3.12(b). Data from Fig. 3.12(a) were used to calculate the vibrational Raman slit function. (b) The corresponding species mole fractions calculated using the concentrations and Eq. 3.15.

of the rotational profile [58]. Rotational Raman scattering for temperature measurements presents two advantages, namely larger scattering cross sections[29, 83] and fast equilibration, when compared to the vibrational degrees of freedom [43].

Figure 3.14 shows how the S-branch rotational population distribution develops as temperature increases for N_2. The population of each rotational state N_J is given by a Boltzman distribution as

$$N_J = \frac{N g_I (2J+1) e^{-BJ(J+1)hc/kT}}{Q_{rot}} \tag{3.18}$$

$$Q_{rot} = \sum_{J=0}^{\infty} g_I (2J+1) e^{-BJ(J+1)hc/kT}, \tag{3.19}$$

where J is the rotational state, N is the total number density, g_I is the nuclear spin degeneracy, B is the species rotational constant, h is Planck's constant, c is the speed of light, k is Boltzmann's constant, and Q_{rot} is the rotational partition function. Details can be seen in Reference [26]. As it can be seen from Fig. 3.14 and Eq. 3.18, higher rotational states become more populated as temperature increases. Noticeable changes of the distribution peak and decay slope can be observed as the population distribution shifts with temperature. This population shift is the basis for our temperature measurements, as the observed rotational signals are proportional the rotational populations. The two methods discussed in this section utilize the integrated rotational Raman energies (I_{rot}) and spectral position of the profile maximum.

3.3.1 Spatial limitations of methods

The two rotational Raman techniques have different spatial limitations to which they can be applied. Figure 3.15 shows the I_{rot} signal profile and average rotational profile maximum (RPM) location on the detector for air at STP. It is immediately noticeable that the I_{rot} signal in Fig. 3.15(a) bears a similarity with the integrated vibrational Raman slit function (N_2 at STP). Shown at the top of Fig. 3.15 is the same illustration also seen in Fig. 3.10, depicting the shape and size of the focused laser with respect to the slit within the spectrometer. Signal rejection due to the fixed width of the slit attenuates the collected I_{rot} signal as the laser diameter grows, and limits temperature measurements using the integrated R_{rot} signal to the region where the laser is completely accepted through the slit (indicated by the dashed lines).

A clear measurement of the average rotational profile maximum location can be made across most of the detector, even in the presence of signal attenuation due to the

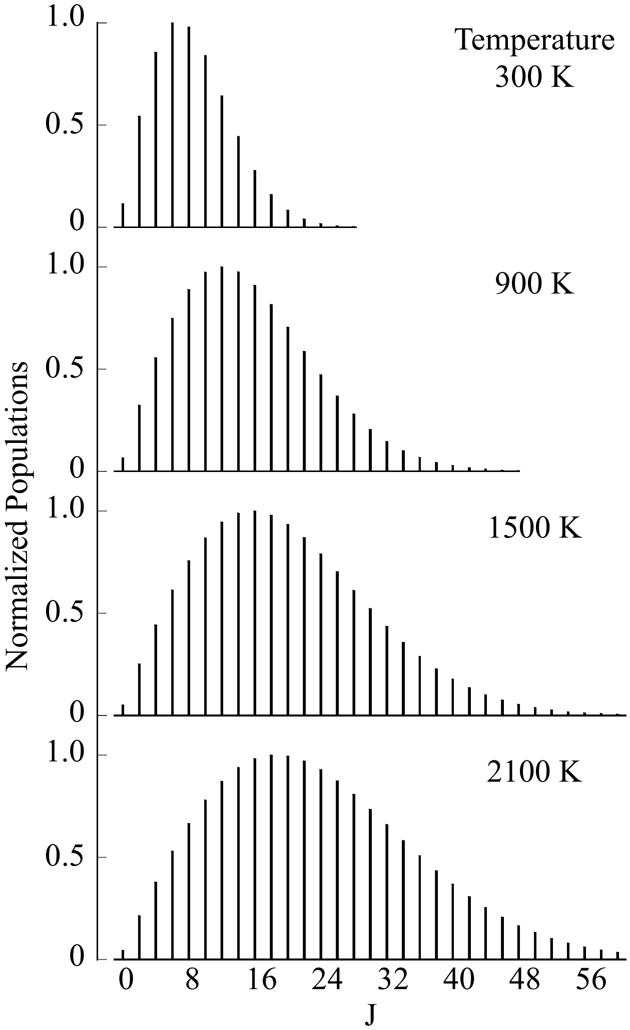

Figure 3.14: Normalized rotational population distributions (N_J/N_{max}) for even N_2 rotational states. As temperature increases, a noticeable shift in the profile peak (position of N_{max}) is observed, as well as a decrease in the decay slope. Both are anticipated by Eq. 3.18.

slit. Measurements of the profile maximum are performed with a 5-point centroiding method in order to circumvent the discreteness of the EMCCD pixels. The rotational profile maximum location at STP is indicative of the curvature of the system, and shows the extent to which the technique can be applied. The effects of vignetting can be seen at the far edges where there is a sharp drop-off of the discernible profile maximum location. Although the average location of the rotational profile maximum

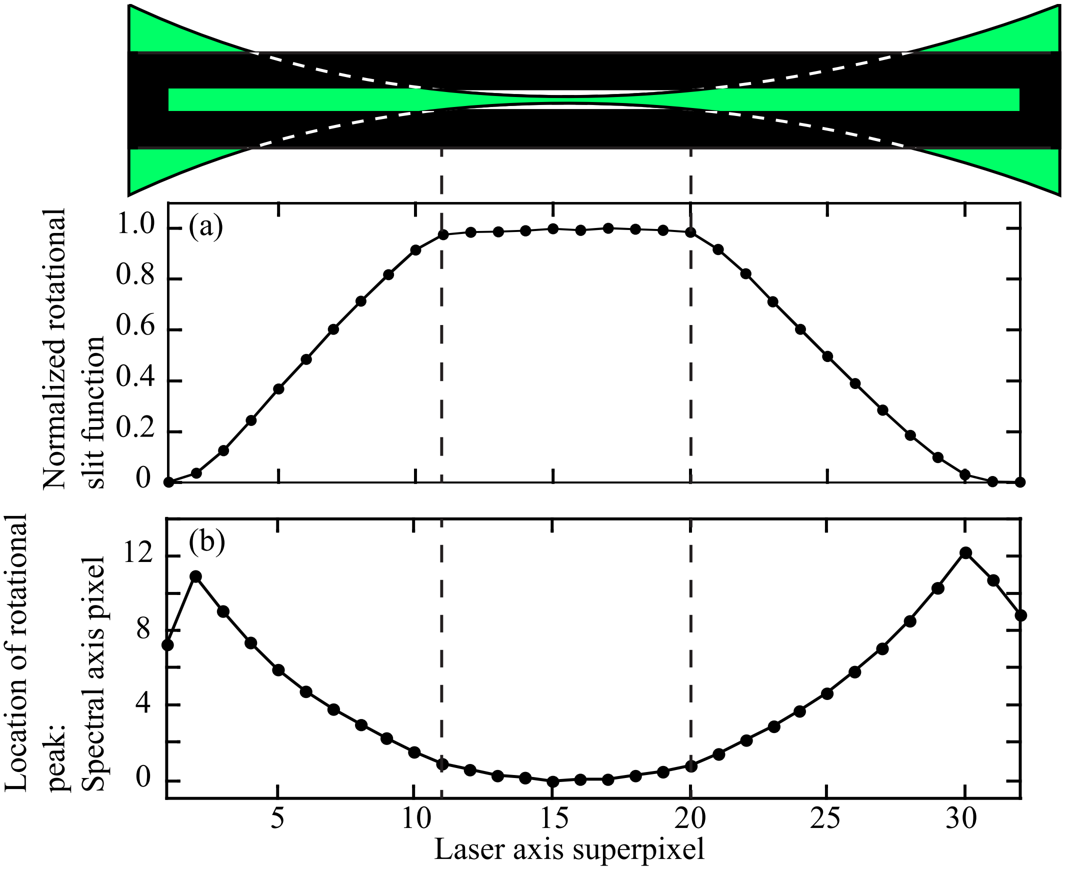

Figure 3.15: (a) The response of the integrated rotational Raman signal for air at STP normalized by the maximum value. This is representative of the rotational slit function, and reveals the edges where the laser no longer completely passes through the spectrometer slit, indicated by the dashed lines. (b) The location of the rotational Raman peak along the laser axis, for the same data set as figure (a). Even beyond the edges of where the laser 'fits' completely through the slit, i.e. outside of the region denoted by the vertical dashed lines, a smooth and continuous rotational peak can be identified. This allows us to extend temperature calculations using the peak method into regions where the integral method becomes problematic. Also worth noting is the limit behavior of the peak position. One point at the left side of the array (superpixel 1) and two points at the right side of the array (superpixels 31 and 32) show erroneous results, even for the peak location. These points cannot be used in the temperature measurements by the rotational techniques.

can be determined across most of the detector, the technique cannot be applied in a shot-to-shot manner due to fluctuations of the laser position.

3.3.2 Species measurement limitations

The lack of rotational raman contributions from several species places limitations on the types of flames and mixtures the rotational Raman techniques can be applied to. The species which have little or no rotational contribution are CH_4, H_2O, and CO_2, for varying reasons. Methane is not rotationally Raman active because of its spherical symmetry, and therefore does not contribute any signal to the rotational techniques [26]. This immediately excludes the application of the rotational techniques to methane diffusion flames, at least where methane is the only species present. Independent temperature measurements along the pure methane centerline would not be possible because the absence of any rotational Raman signal, and would have to rely on either a constant pressure assumption, or a different diagnostic technique.

The rotational Raman spectrum of water is extremely weak because of its smaller differential scattering cross section, which is approximately two orders of magnitude smaller than nitrogen [77, 3], and is spread over a wide range of rotational states [22]. Carbon dioxide does possess a rotational Raman spectrum, but because of the small rotational constant of the molecule, the rotational spectrum appears very near the laser wavelength (532 nm), and as a result it is practically eliminated by the long-pass filter.[30, 22, 58]. The two species, which are the main products of combustion, limit the rotational Raman technique to measurements in flames with N_2 as part of the composition. Premixed $CH_4 - O_2$ flames would have rotational signal contributions from O_2 alone in the reactants, allowing for independent temperature measurements. However, as the measurements carry over to the products, the lack of rotational signal would make temperature measurements all but impossible.

The temperature measurement technique is essentially limited to flames which have some amount of nitrogen throughout the flame. As will be discussed, the code used for synthesizing our rotational Raman spectra does not include the rotational Raman spectra of CO_2 and H_2O. Although this should not be of concern for CO_2 since its signal is practically eliminated, the rotational temperature technique will incur a small error that scales with the mole fraction of water. The error in the technique should be on the order of 1% due to the rotational scattering cross section of water being two order of magnitude smaller than nitrogen, which is typically a large constituent for methane-air flames.

3.3.3 Spectral synthesis

Spectral synthesis of the major combustion species is performed using a converted version of the RAMan Spectra Efficient Simulation (RAMSES) program [41]. The converted code is customized to match the specifications of the spectrometer, and is packaged in a dynamically linked library (DLL). For the purposes of this work the converted spectral synthesis code was given the designation 'Raman Synthesis' (RamSyn). This is not meant to detract from the importance of the original contribution [41]. Simple diatonic gases (N_2, O_2, H_2, and CO) are synthesized *ab initio* calculations, while the remaining species (H_2O, CH_4, and CO_2) are synthesized based on experimental data generated by past experimental studies. The version of the software used in this study did not include the evaluation of rotational spectra for water and carbon dioxide. However, as mentioned in the previous sub-section this should have little or no effect on our measurements. The response of the long-pass filter was included in the synthesis process during the code conversion, and allows for angle tuning as an input. As will be shown subsequently, the synthesized signals are convolved with a Gaussian function that closely mimics the beam profile. The DLL is imported into LabView, which provides a framework for simplified user interface, as well as automated data post-processing.

Figure 3.16 shows S-branch Raman fractional populations (N_J/N) for N_2 at STP conditions. The individual line spikes can be converted from the discrete rotational levels (J space) to their corresponding Raman frequency shift $\Delta\bar{\nu}$ using the relation

$$\Delta\bar{\nu} = -4B(J + \frac{3}{2}). \tag{3.20}$$

Doppler and pressure broadening convolve the individual transitions with Gaussian and Lorentzian lineshapes, respectively. For N_2 at one atmosphere, the overall linewidth FWHM has been calculated to vary be between 0.1 cm^{-1} at 300 K and 0.03 cm^{-1} at 2000 K[69]. However, the individual spectral transitions of our synthesis are not convolved with Gaussian or Lorentzian profiles of this size, but with a Gaussian function that represents the physical profile of the laser beam.

To interpret the rotational measurement appropriately, we must realize that any signal registered onto the detector along the vertical spectral axis is not solely the effect of diffraction through the holographic grating, but also the effect of straight forward imaging under 1:1 conjugation through the optical relays. This, of course, is the effect of the finite width slit used in the spectrometer. In the limit of an infinitely thin slit, the signal on the detector corresponds to pure diffraction through the grating. In the opposite limit of no slit used within the spectrometer, the image formed onto the detector corresponds to a convolution of diffraction *and* imaging through the optical relays.

The laser profile, based on the Rayleigh signal of air at STP, was measured with the spectrometer without the slit or the long-pass filter. As a consequence, the full laser waist could be imaged without restrictions by the slit, and furthermore, the elastic light (Rayleigh) image of the laser could be formed onto the detector.

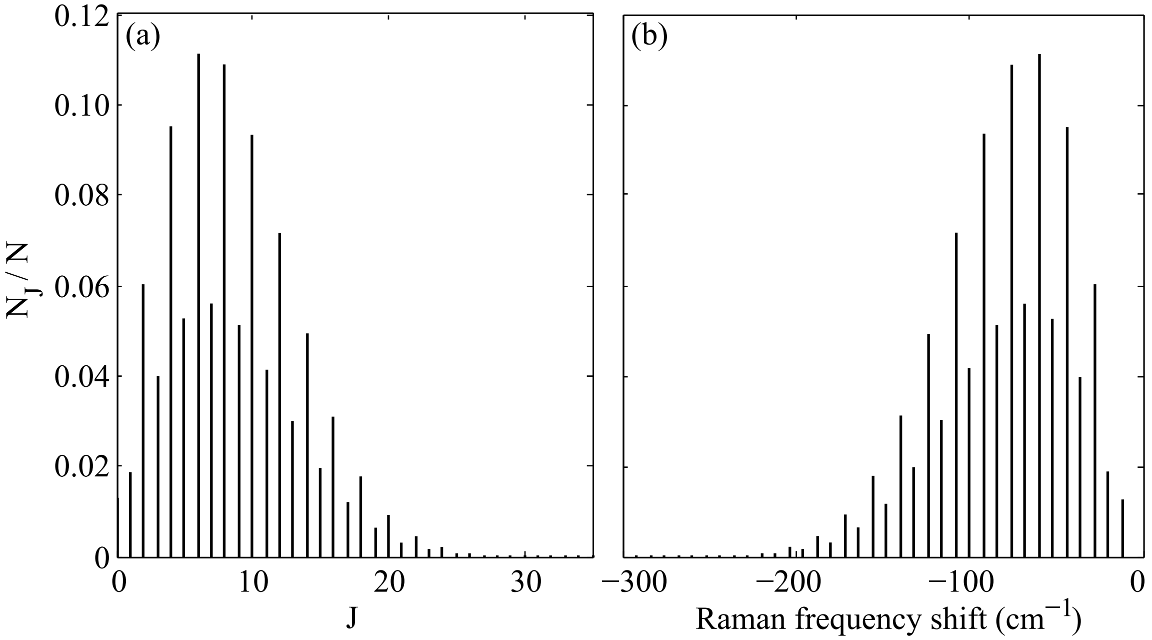

Figure 3.16: Synthesized rotational population distribution for N_2 at 300 K. (a) Population distributions are first calculated for each rotational state J, (b) and then are converted into Raman frequency shifts using Eq. 3.20.

Figure 3.17 shows the measured beam profile, and a fitted Gaussian based on the approximate FWHM of the Rayleigh profile. The horizontal axis shown is converted from spectral axis pixels to nm based on the known dispersion of the spectrometer. The corresponding FWHM of the beam is 9 detector pixels (i.e. 144 μm beam waist), which correlates to an approximately 3.6 nm on the spectral axis of the spectrometer. While this image of the laser is generated by simple imaging through the optical relays, it registers as broadening along the wavelength axis of the detector. It can be interpreted as corresponding to broadening of approximately 127 cm^{-1} in width. This broadening is much larger than either pressure or collisional broadening, and merely represents the physical width of the laser waist. This broad profile is not due to pressure or collisional effects, but merely represents the physical width of the laser. The width of the beam profile, and low resolution of the spectrometer, results in spectral profiles that do not reveal individual rotational transitions. For this reason, the spectral synthesis does not convolve the individual line signals with Doppler or pressure broadened profiles, but rather a profile that closely remembers that of the laser.

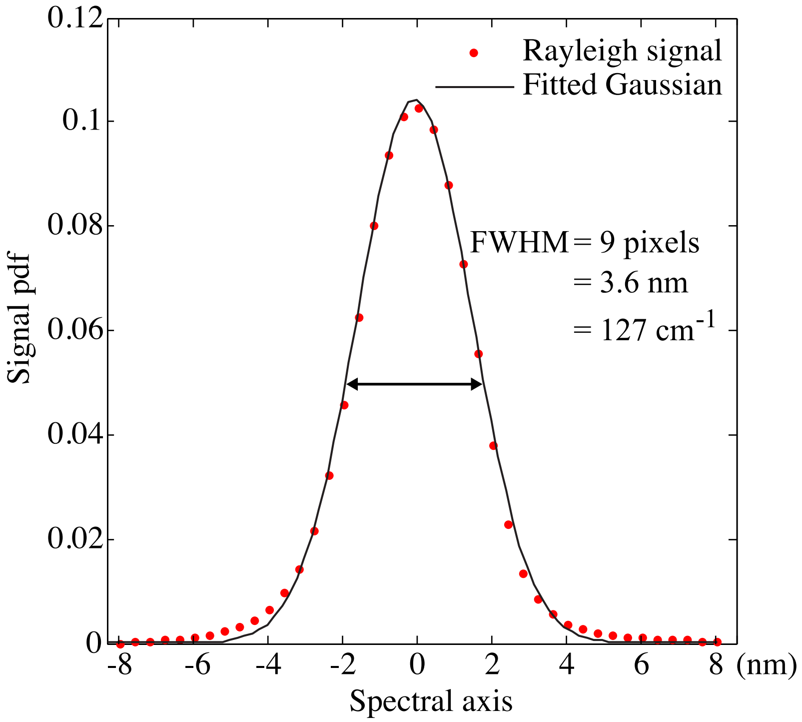

Figure 3.17: Measured Rayleigh profile using the Raman spectrometer, and fitted Gaussian. The FWHM of the Rayleigh signal is measured to be approximately 9 physical pixels on the EMCCD, or approximately 3.6 nm on the spectral axis. This width corresponds to approximately 127 cm^{-1}, and is the predominant source of broadening in our system.

3.3.4 Integral method for temperature measurement

Summation of the S-branch rotational populations, Eq. 3.18 as previously seen, over all rotational states ($J = 0$ to inf) yields the total population, i.e. $\sum_{J=0}^{\infty} N_J = N$. Therefore, the summation over all rotational states should be independent of the temperature, when normalized by the total rotational population N. However, as it was shown earlier in Fig. 3.14, the rotational population shifts towards higher rotational states (i.e. wavelengths) at higher temperatures. If a long-pass filter is introduced, the summation of the collected rotational populations becomes temperature sensitive. As temperature increases, more of the population signal becomes visible beyond the filter, and the integral of the rotational populations increases. At extremely high temperatures (greater than 10^4 K), most of the population distribution is at rotational states and wavelengths that exceed the cut-off of the filter. As the temperature increases, the summation of the visible rotational profile approaches a constant value which corresponds to the total population N.

Addition of the long-pass filter to the spectrometer makes the integrated signal of the collected rotational Raman energy (E_{rot}) sensitive to temperature, giving rise to our independent method of measurement. The profile of the collected rotational energy is a function of both wavelength and temperature ($\mathrm{E}_{rot} \propto f(\lambda, T)$), and as previously shown by Eq.3.2, the amount of collected energy is directly proportional to the concentration C_i of the species present. If the filtered rotational Raman profiles (FE_{rot}) are normalized by the measured concentration (i.e. density), the strength and shape of the profiles become functions of only wavelength and temperature. Figure 3.18(a) shows the progression of synthesized filtered rotational profiles for air with increasing temperature, and normalized by their respective densities. Two noticeable effects can be seen with increasing temperature are an increase in the integral, and a shift in the rotational profile maximum as temperature increases. The latter of the two will be discussed in the next subsection.

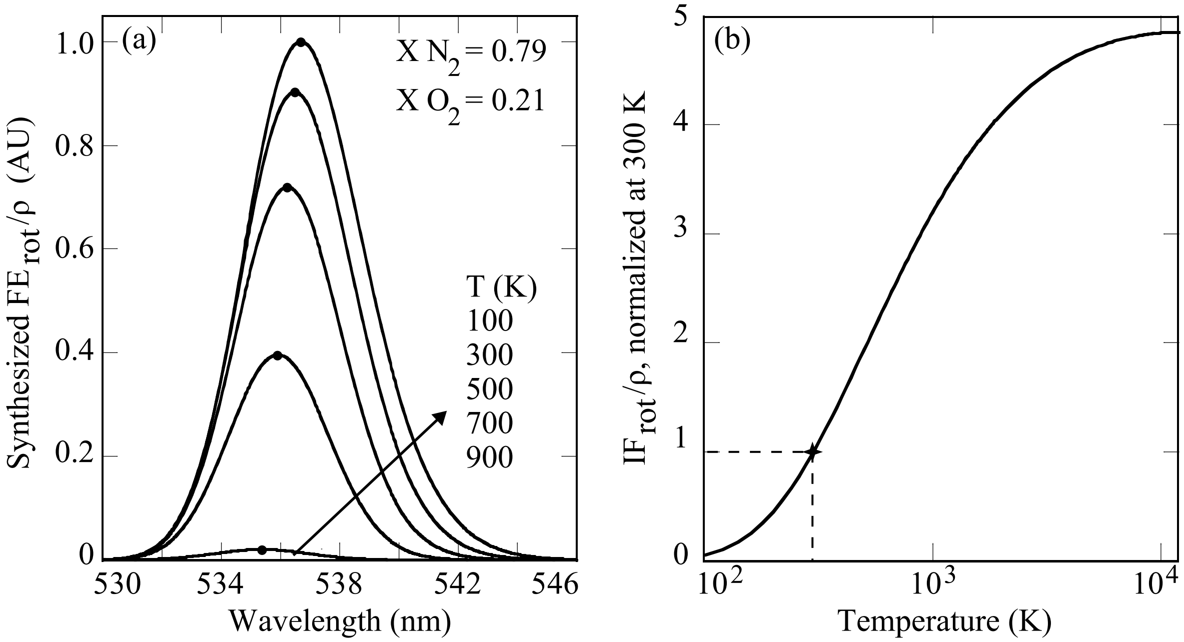

Figure 3.18: (a) Synthesized filtered rotational profile for air, normalized by density. The profiles shown are synthesized for the indicated temperature, and at one atmosphere. (b) Integrated filtered rotational profiles for air that have been normalized by density, over a wide range of temperature. The overall results are normalized by the results at 300 K (indicated on the figure). As temperature increases to high values, it is observed that the results approach a constant value.

Figure 3.18(b) shows how the result of integrating the filtered signals (IF_{rot}) is a function of only temperature when normalized by density. The results shown are normalized by conditions at 300 K, and are carried out to 12,500 K to show the expected constant value arrival. Density measurements using the vibrational Raman technique must occur in parallel with the rotational Temperature technique, as the integrated signal must be normalized by the density of the scattering population. Ambient air measurements taken prior to data acquisition form the rotational slit function, and provide the reference point $(IF_{rot}/\rho)_{air,STP}$ for the temperature measurements. During post processing, the collected integrated rotational signal is normalized by the simultaneously measured density and previously recorded slit function to form the relation

$$\frac{(IF_{rot}/\rho)}{(IF_{rot}/\rho)_{air,STP}} = f(T, X_i's), \tag{3.21}$$

Rotational Raman spectra are synthesized and integrated for the measured composition over a range of temperatures. The ratio $(IF_{rot}/\rho)/(IF_{rot}/\rho)_{air,STP}$ is synthetically formed and compared with the experimental value. A bisection method is used to converge on the temperature that gives the best agreement between the synthesized and experimental results. Approximations of error and SNR for the technique are discussed in the results chapter. Similar to the vibrational technique, the values of error and SNR will vary depending on the type of flow being interrogated.

3.3.5 Spectrum maximum location method

As it was shown in Figs. 3.18 and 3.14, the rotational profile maximum location varied based on the temperature of gas. The filtered rotational profile shifts to longer wavelengths as temperature increases, and changes in the profile maximum location can be tracked using a 5-point centroid method. Figure 3.19 shows the shift of the profile maximum location for air as temperature is increased from 100 to 1500 K. For the temperature range shown, the shift in the maximum location covers a rage of approximately 1.6 nm, which corresponds to 4 physical pixels on the EMCCD along the spectral axis. High resolution pixel binning is maintained over the rotational profile for this reason specifically. The resolution is slightly reduced by 2-pixel binning, but benefits the SNR of the collected spectra. The underlying rotational profile maximum is estimated by the 5-point centroiding algorithm, and allow us to extend the method beyond the discreteness of the pixel binning.

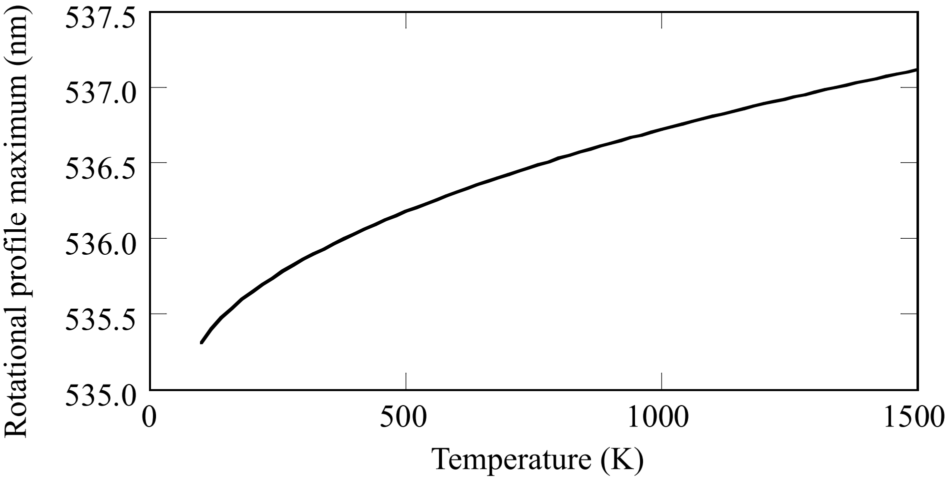

Figure 3.19: Location of the rotational Raman peak vs. temperature for air. As temperature increases, the rotational profile shifts to longer wavelengths, and the location of the profile maximum can be tracked.

The rotational profile maximum location is not a function solely dependent upon the gas temperature, however, and is also dependent upon the mixture of the gas. Variations in the gas composition can induce a shift in the profile maximum location, at constant temperature conditions, because of differences between the species rotational constants. Two approaches to the method can be applied when measuring temperature between points, and are outlined in Fig. 3.20. Rotational profile maximum locations for air at STP and a vitiation product jet are shown in Fig. 3.20(a). The example shown here is from the same data set previously shown in Figs. 3.12 and 3.13 for vibration Raman measurements.

A sample measurement of temperature will be made at superpixel location 19, and a zoomed in view of the pixel neighborhood is shown in Fig 3.20(b). The

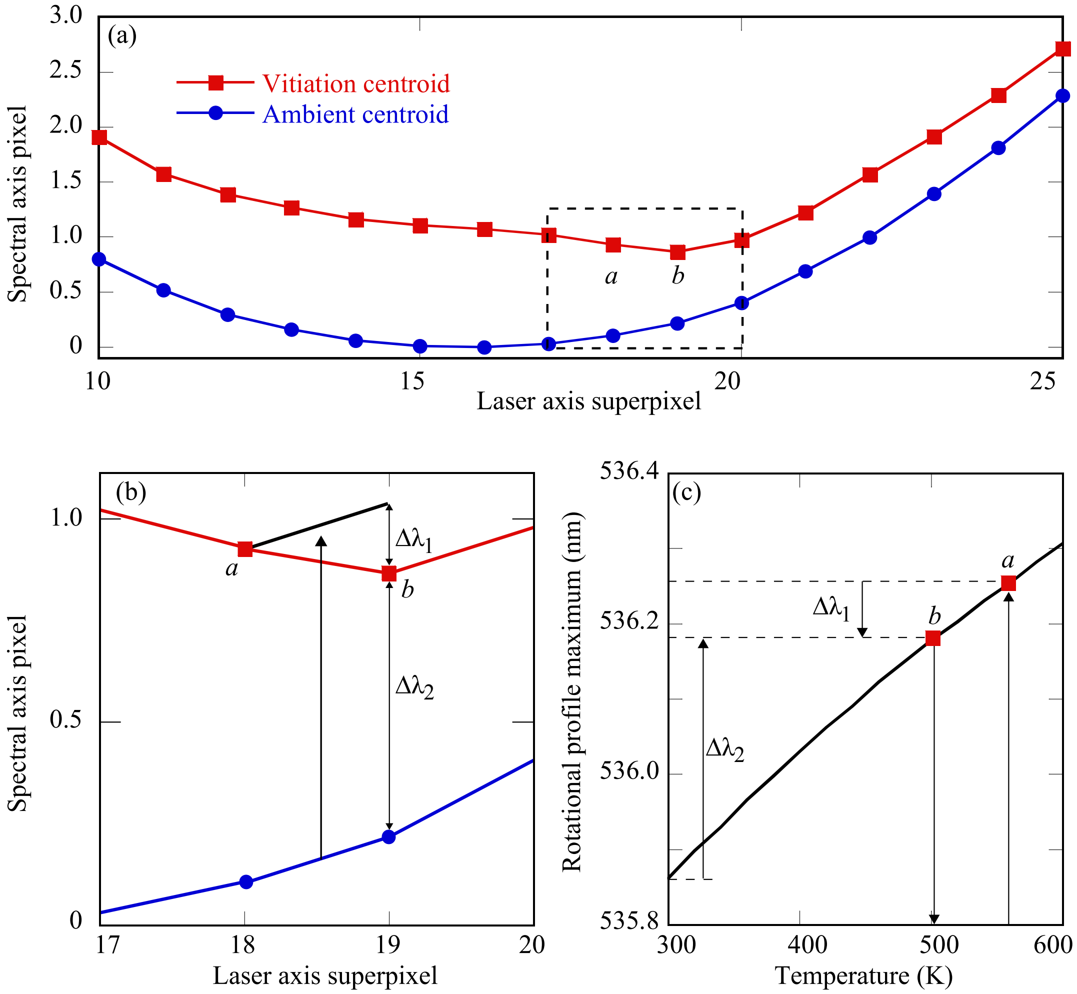

Figure 3.20: (a) Rotational profile maximum locations for ambient air and hot vitiation products. A sample temperature calculation is carried out at point b in the figure. An expanded view of points a and b is shown in figure (b). Temperature calculations can be carried out using the change in spectral location based on the nearest neighbor and ambient conditions ($\Delta\lambda_1$), or based on the overall shift of the rotational profile ($\Delta\lambda_2$). (c) A visual representation of the sample temperature calculation at point b using both methods of measurement.

first approach relies on prior temperature measurement of a neighboring pixel, and assumes that the composition does not vary significantly between the two points. Based on the results from the vibrational Raman section, it is safe to assume that the composition of pixels 18 and 19 is approximately that of air. The temperature at the neighboring pixel can be measured by either rotational technique, but is required for the approach. Pixels 18 and 19 will be referred to as a and b, respectively, so that the technique can be described in general terms.

Knowledge of the the ambient condition rotational profile maximum location provides the profile curvature for a constant temperature and composition. If the ambient condition slope between pixels a and b is superimposed on the measured rotational profile maximum location of pixel a, as shown in Fig. 3.20(b) by the black line, the end point at pixel b would represent the theoretical maximum location if the temperature remained constant. However, because there is a change in temperature between the two pixels, the maximum location has shifted, and is measured as $\delta\lambda_1$ based on the known dispersion of the spectrometer. Figure 3.20(c) shows the rotational profile maximum location versus temperature for the composition of the two pixels of interest. Pixel a is approximately 560 K based on previous temperature measurement, and is marked in Fig. 3.20(c). The temperature at pixel b is measured by applying the change of the rotational profile maximum location $\Delta\lambda_1$ to pixel a's peak location, and is approximately 505 K.

The second approach for temperature measurement based on the rotational profile maximum location is simpler and more robust. The method is not limited to constant composition restrictions, and is simply measured by the spectral shift of the rotational profile maximum. Figure 3.20(b) shows how $\Delta\lambda_2$ is measured directly between the two rotational profile maximum location curves. During post processing, spectral synthesis of the rotational profile based on the measured experimental composition is performed over a range of temperatures. The temperature which produces the closest spectral shift of the profile maximum location to $\Delta\lambda_2$ is chosen as measured value. Because the example shown in Fig. 3.20(c) closely corresponds to air, this example can be easily shown. If the value $\Delta\lambda_2$ is added to the profile maximum location at

300 K, the corresponding value along the synthesized curve in Fig. 3.20(c) would indicate a measured value of about 505 K. It should be noted that the rotational profile maximum locations reported here are averaged over 100 shots. Shot-to-shot fluctuations of the laser position prevent the technique from being applied in a single shot manner, and must rely on the average spatial location of the laser.

4. EXPERIMENTAL RESULTS

4.1 Supersonic air jet

Initial experiments were conducted with an underexpanded air jet, and provided a means for calibration of the system. The structure of the jet is well known, as previously discussed, and provides oscillating over- and underexpansion regions within the flow. Oscillations of density, temperature, and pressure along the jet axis can be measured by the Raman spectrometer, as well as computed using commercial computational fluid dynamics (CFD) code. The non-reacting composition of the jet simplifies the complexity of the experiment for both the experiments and CFD, and provides a suitable platform which the two can be used together. The CFD results for calibration were performed by Dr. Paulo Grego from University of Sao Paulo, Brazil.

The rotational Raman technique is not absolute because of the inclusion of the long-pass filter, and must be calibrated against the CFD temperature results. Temperature calculation results are strongly dependent upon the filter-tuning angle (and hence cut-off wavelength) of the filter. The angle of the filter is measured with precision on the order of $\sim 1^o$, and can be improved with calibrations for better accuracy. Although knowledge of the AOI is important for temperature calculations, the calibrations can occur during post-processing since the AOI does not vary with time.

The measured jet emanates from a converging nozzle, with a 3.5 mm throat diameter and total pressure of 20.3 $psig$. Dry air, also known as zero grade air, was used to prevent Mie scattering from corrupting the rotational Raman data. The Reynolds number based on the throat diameter, and sonic velocity of the throat is approximately Re = 115,000. Despite the high Reynolds numbers, the macroscopic structure of the flow is steady and stationary, which allows for measurements to occur over an extended period of time. A scan along the jet axis (z) was performed over 50 locations, with 100 laser shots collected and averaged at each. The scan was initiated 3.5 mm downstream of the nozzle throat, with approximately 254 μm between each location. Measurements closer than 3.5 mm to the jet exit were not possible because of excessive reflections from the nozzle. Horizontal hardware binning on the EMCCD was performed over 16 pixels, or 256 μm along the jet radius. The composition of the jet was measured at each point of the scan, rather than assumed to be air, and was used to synthesize theoretical spectra for temperature measurements.

4.1.1 Thermochemistry results, and comparison with computations

Figure 4.1(a) shows CFD and schlieren results for the same air jet case that was measured. Similarities can be seen between the CFD calculated density gradient and schlieren image with regards to the size and shape of the structure. The two results develop at different rates however, and is clearly visible in the mismatch between the 'Mach diamonds' at $z \sim 15$ mm. The difference in development rates is possibly attributed to the lack of entrainment in the CFD calculations, and the choice of turbulence model used. Although there is a difference in the rates in which the CFD and experiments develop, the oscillating levels of the thermodynamic properties (ρ, T, and P) should be approximately the same.

The densities measured by the vibrational raman technique are shown shown in Fig. 4.1(b). A clear distinction between the core of the jet and the ambient atmosphere can be observed, as there is a steep density gradient between the two. This jet boundary is also observed in the CFD density gradient, and follows the same contour as the experimental result. The Mach diamonds shown in the schlieren

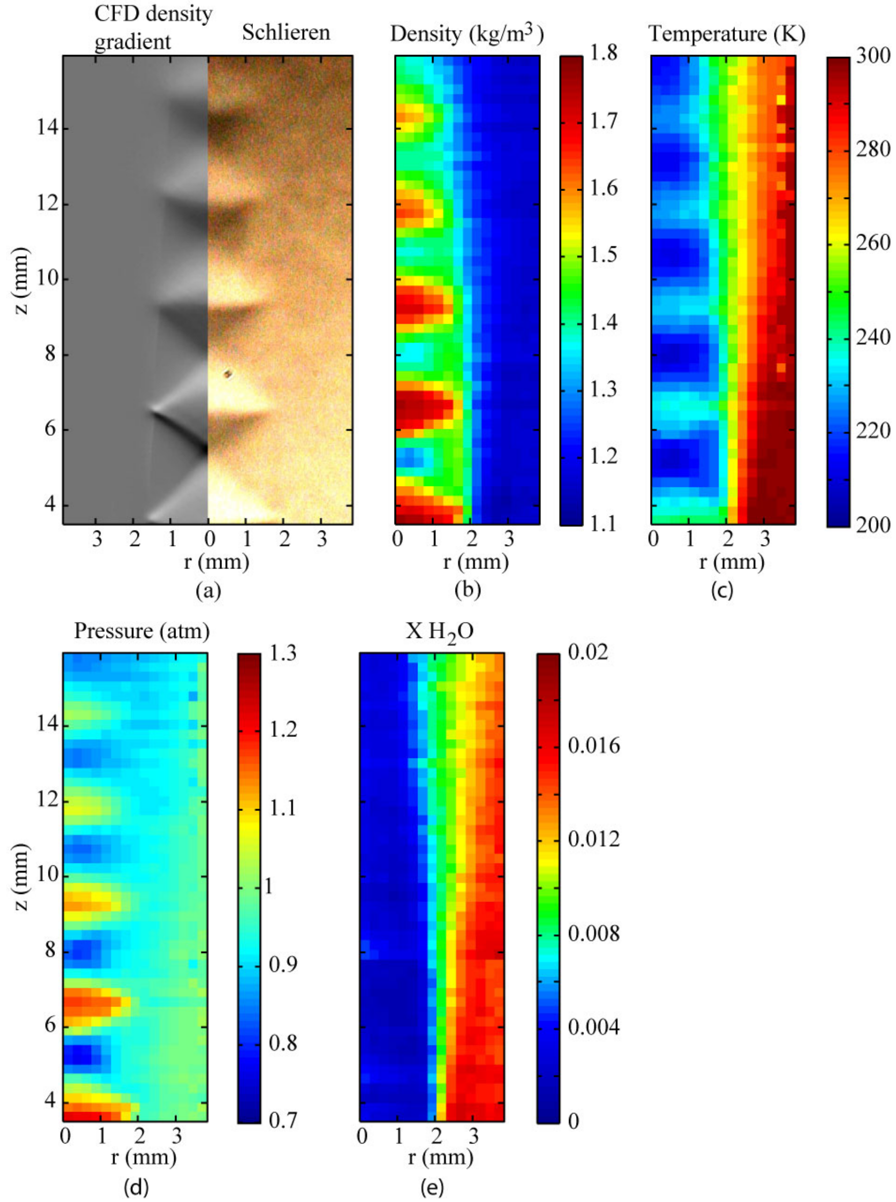

Figure 4.1: CFD and experimental results for the underexpanded air jet, with *Re* = 115,000. The jet emanates from a converging nozzle with a 3.5 *mm* exit, and total back pressure of 20.3 *psig*. The scan was performed over 50 locations along the jet axis z, starting at $z = 3.5$ mm. (a) Side-by-side comparison of the calculated CFD density gradient and schlieren image of the experimental jet. Measurements of density, temperature, pressure, and water mole fraction are shown in Figs. (b) through (e), respectively.

image are discernible, and identified by the high density regions within the jet core.

Centerline values of the density are shown in Fig. 4.2(a) for both the CFD and experimental results. A good agreement between the overall levels of the measured density can be seen up to approximately 9 mm down stream of the jet exit. Additionally, good agreement between the two density profiles is observed within this region. Beyond 9 mm of the jet exit, the experimental results show a dampening of the density oscillation, and also highlight the faster development of the experimental jet. This is shown by the local maxima of the experimental density values, and the increasing discrepancy between those of the CFD results. The last measured local maxima occurs at approximately 0.5 mm prior to the local maxima calculated by the CFD. As it was previously mentioned, however, this discrepancy is possibly due to the lack of entrainment in the computational results, and allow the flow to dampen at a slower rate.

Temperature measurements are first calibrated against the CFD results for the first expansion encountered. This region is used because of the small disagreements observed between the measurements and computations further down stream. The filter angle of incidence used for synthesizing the rotational Raman, as previously mentioned, is measured to a precision on the order of $\sim 1^o$. Further precision of the filter AOI is necessary in order to increase the accuracy of the temperature measurements. Figure 4.3 shows a comparison between the CFD centerline temperatures and processed rotational Raman results for AOI between 5^o and 6^o using the integral method. A one degree difference in AOI is capable of producing temperature results that differ by approximately 10 K. As it can be seen in Fig. 4.3, the filter AOI that agrees the best with the CFD is approximately 5.2^o. This AOI is used for all rotational Raman temperature calculations presented in this chapter.

Independent temperature measurements, shown in Fig. 4.1(c), reveal the same

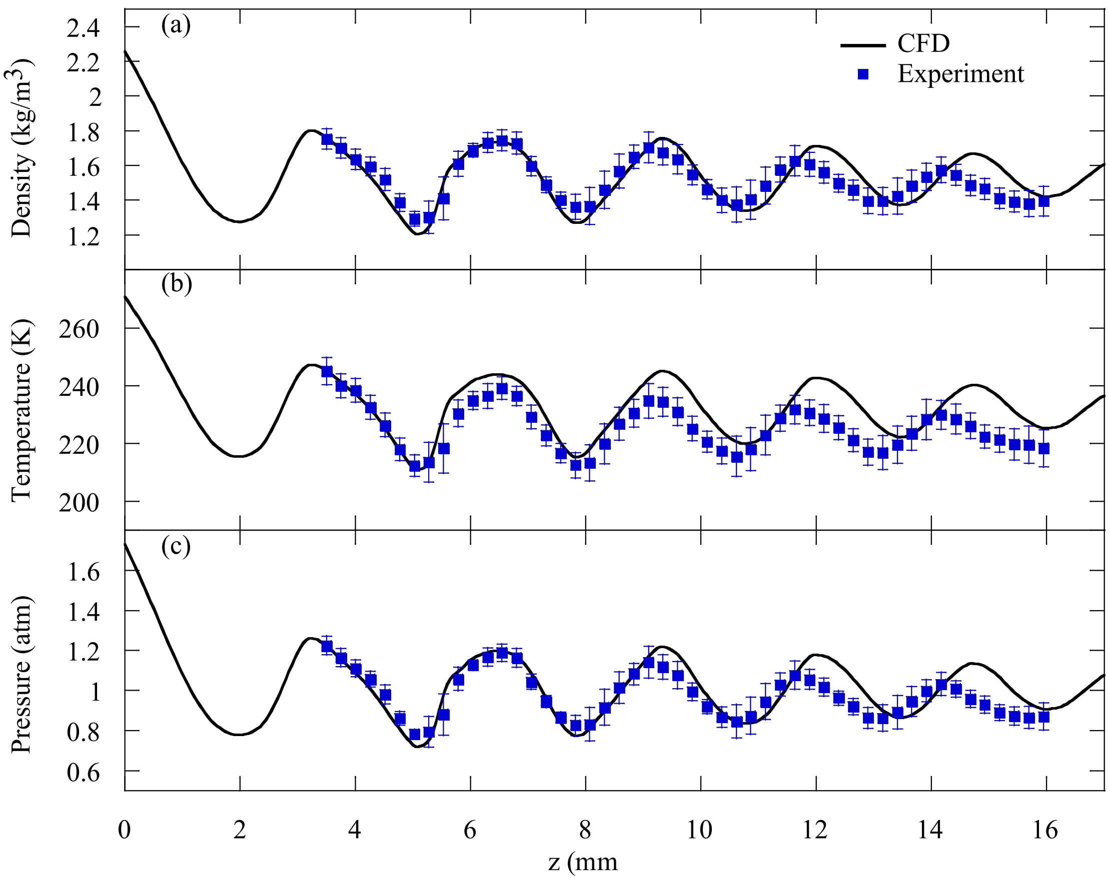

Figure 4.2: Centerline CFD and experimental results for (a) density, (b) temperature, and (c) pressure. Single-shot statistics were performed to calculate the standard deviations of the measured values, and are shown as the error.

flow structure previously seen Figs. 4.1(a) and (b). A very clear and discernible slip stream, with a temperature at about 235 K, can be seen that defines the inner jet core. As mentioned, temperature measurements between $r = 0$ to 3 mm were calculated using the rotational Raman integral technique, whereas the measurements out at the jet periphery were performed using the rotational profile maximum. A visible result of the measurement, not seen in the density results, is the growth of the jet downstream of the nozzle exit. Although the jet core remains intact, the turbulent mixing layer of the jet can be seen increasing in size.

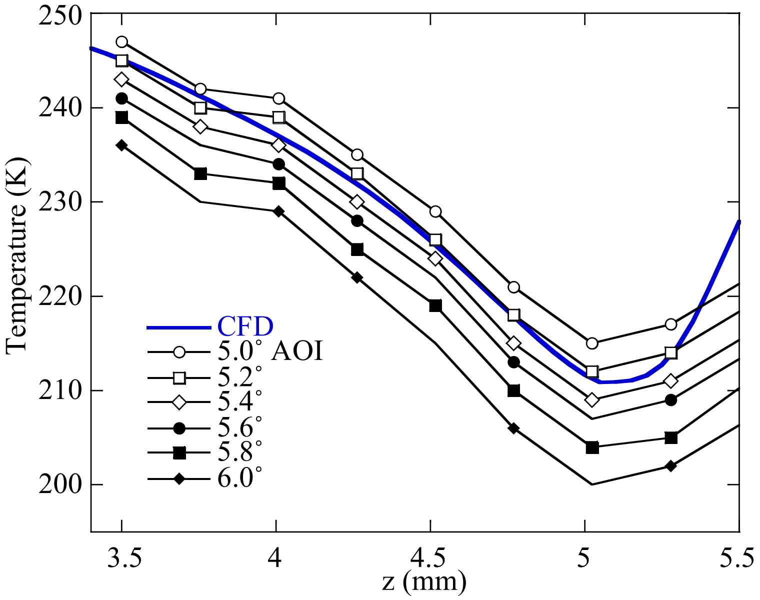

Figure 4.3: Angle tuning calibrations for rotational temperature measurements. CFD calculated temperature at the first expansion is compared with the post-processed results for different filter tuning angles. A suitable match is found with a filter AOI at 5.2^o

Measurements along the jet centerline for temperature, shown in Fig. 4.2(b), show a temperature profile that bears resemblance to the CFD results. The behavior of the experimentally measured temperatures, when compared to the CFD results, is similar to that seen with the flow density. The temperature profile along the centerline shows good agreement with regards to level of the measurement, and overall profile shape, up till 9 mm past the nozzle exit. Beyond this point the measured flow temperatures become out of phase with the oscillations of the calculated CFD temperatures, and the overall level of the measured temperature peaks diverges by approximately -14 k

The ideal gas law is used to calculate the flow pressure profiles based on the species densities that were measured using the vibrational Raman technique, and the flow temperatures calculated using the rotational techniques. The calculated pressure profiles for each scan location, seen in Fig. 4.1(d), clearly show the high and low pressure lobes that are expected in an underexpanded jet. Figure 4.2(c) also highlights the pressure variation along the jet axis. A level of underexpansion is seen at the beginning of the measurements, where the pressure is greater than the atmospheric conditions. Shortly thereafter, Prandtl-Meyer expansion fans over expand the flow, and the pressure along the jet centerline falls below 1 *atm*. Pressure along the jet centerline behaves similarly to the density and temperature, with the measured jet profile developing much faster than the CFD results. The derived pressure results between 3.5 and 9 *mm*, however, show excellent agreement with the CFD calculated values. The mixing layer growth towards the jet periphery is also observed in Fig. 4.1(d), as the slightly lower pressure of this region expands into the STP lab conditions.

Dry air was used for the measurement originally to prevent Mie scattering, but was shown to be useful for viewing the extent of the jet spreading. The jet spreading observed in the temperature and pressure results is corroborated by the water mole fraction, shown in Fig. 4.1(e). Ambient measurements indicate that the mole fraction of water content in the lab atmosphere was approximately 0.015 on the day the measurements were taken. Vibrational Raman measurements show no water content is present in the jet core, which is expected and clearly seen in Fig. 4.1(e). As the jet spreads, small amounts of water content can be seen within the mixing layer. This result suggests that water content from outside the jet (and hence ambient air) is entrained by the jet as it develops.

4.1.2 Isentropic expansion

An alternating series of expansions and compressions compose the structure of the supersonic jet. Prandtl-Meyer expansions within the oscillating series are treated as isentropic, which can be verified using the measured properties of the jet. Density, temperature, and pressure for an isentropic process can be calculated between two points (x and y) from the well known relations[42]

$$\frac{\rho_x}{\rho_y} = \left(\frac{T_x}{T_y}\right)^{\frac{1}{\gamma-1}} = \left(\frac{P_x}{P_y}\right)^{\frac{1}{\gamma}}. \tag{4.1}$$

Temperature and pressure along the centerline expansions will be calculated based on the measured density, since the vibrational Raman technique is considered to be absolute. Point x will be taken to be the first point of the expansion being examined for the measured parameters, and the isentropic calculations will be propagated along the jet axis. The results of the isentropic calculations for temperature and pressure are shown in Fig. 4.4.

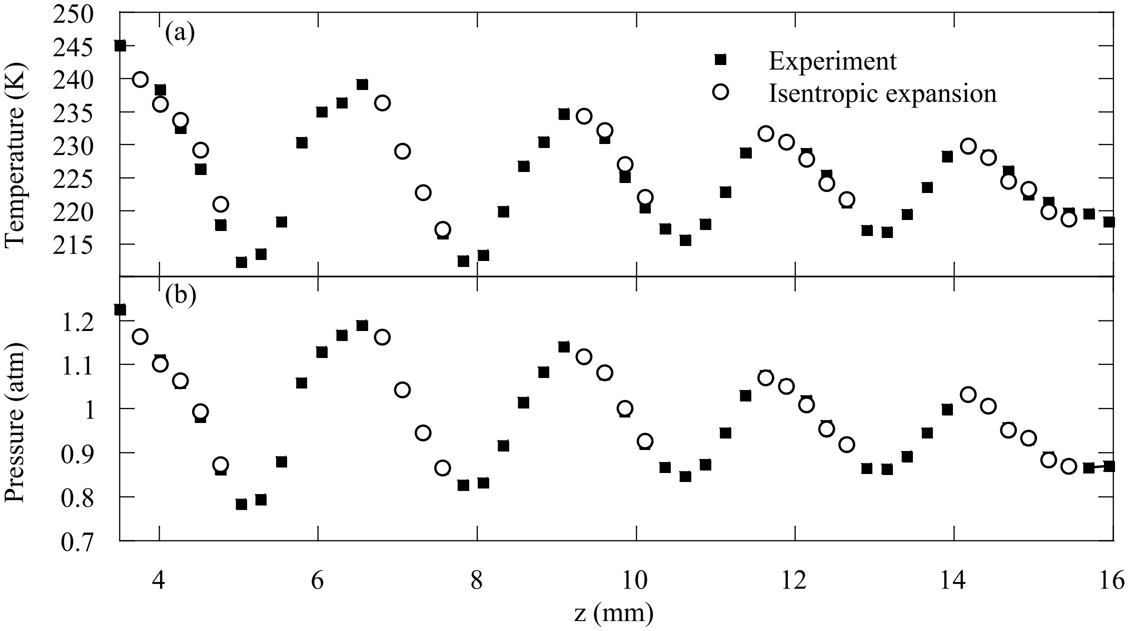

Figure 4.4: Calculated isentropic expansions vs experimental data for (a) temperature and (b) pressure. The isentropic expansions were calculated based on density measurements, and a constant specific heat ratio $\gamma = 1.4$.

Isentropic calculations of temperature, shown in Fig. 4.4(a), show agreement with the measured values to within 1 or 2%, depending on the expansion being examined. In the case of the first expansion, the steep temperature gradient seems to diverge (on the order of 2%) from the isentropic calculations as it moves further away from the jet exit. However, the expansions with milder temperature gradients downstream show better agreement with the calculated isentropic values. Pressure, shown in Fig. 4.4(b) shows better agreement all around with the calculated isentropic values. This is partly due to the fast that pressure is directly derived from the measured density, which is also used to calculate the isentropic expanded values. Overall, the isentropic values for temperature and pressure along the centerline agree to within 2% of the calculated isentropic values, and it can be concluded that the measurements of temperature and pressure capture the isentropic expansions.

4.1.3 Error and SNR

Figure 4.5 the averaged results of density, temperature, and pressure for the first scan location of the supersonic jet. Single-shot calculations of density, temperature, and pressure were performed to examine error and signal to noise ratio of the measurements within the jet. The error bars shown in Fig. 4.5, as well as Fig. 4.2, are the calculated standard deviations of the respective properties shown. For the single location shown in Fig. 4.5, the relative error across the measurement is fairly constant for all three properties, except for at the jet boundary. The resolution of the technique along the laser axis is not capable of fully resolving the strong gradient as the measurement crosses the jet boundary. Density, for example, has a relative error of approximately 3-4% across the measurement shown in Fig. 4.5(a), except at the jet boundary where error can be as high as 5.5%. Larger errors in density measurements are seen along the jet centerline when shocks are encountered. This is due to the thickness of the laser being being much larger than the size of the shocks (on the order of mean free paths[43]). The relative error of density can be as high as about 8% when compression is seen along the jet centerline. However, this is only in isolated cases where the density is at a local minima (i.e. low signal), and shocks occur immediately afterwards.

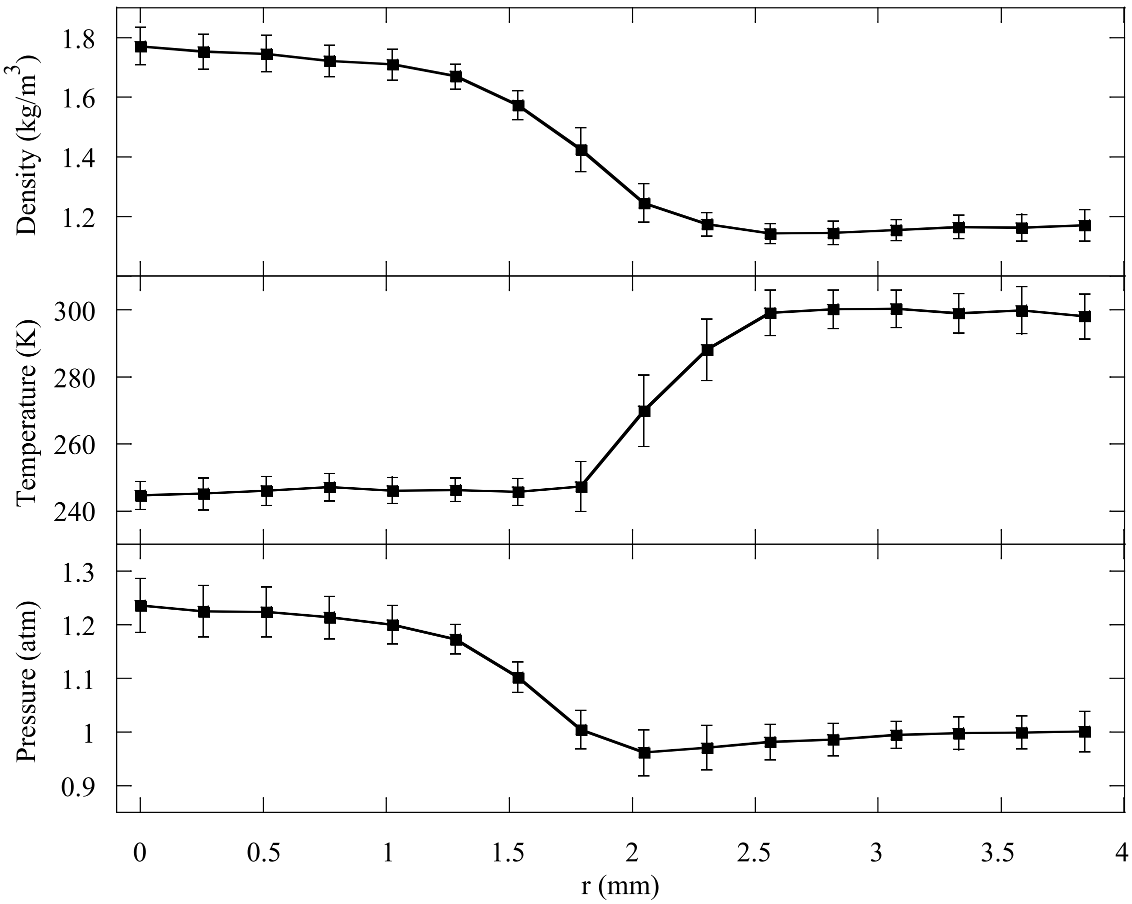

Figure 4.5: Single scan location measurements and errors (standard deviation) at z = 3.5 mm for (a) density, (b) temperature, and (c) pressure. Single-shot statistics were performed to calculate the standard deviations of the measured values.

The signal to noise ratios of the individual species used to calculate density, are calculated based on the species signal means and standard deviations [71]. The main species present in the current measurement are N_2, O_2, and H_2O, and their respective SNR's shown in Table 4.1. These are the best possible cases of SNR that will be seen for the individual species, as experiments in higher temperatures will suffer from reduced number densities, and hence reduced species signals.

Table 4.1: Air jet vibrational and rotational signal to noise ratios. Mean values shown are averaged over the length of the jet scan. Vibrational Raman SNR's are reported for the individual species listed in the table.

Species	Mean SNR inside supersonic region	Mean SNR at jet periphery	Max. SNR observed	Min. SNR observed
N_2	20.7	19.6	38.0	8.6
O_2	16.5	14.5	27.8	8.0
H_2O	1.9	4.0	7.1	1.3
IF_{rot}	16.1	17.5	34.6	6.5

The behavior of temperature and pressure relative errors follow very closely with those of density. For the single scan location shown in Fig. 4.5(b), the relative error is approximately 2%, except at the jet boundary where the value increases to about 4%. The relative errors of temperature are sightly better than those calculated for density, and this can be expected due to the larger differential scattering cross-sections, and hence larger signals, of the rotational Raman technique [26]. Along the jet centerline, the highest values of temperature relative error are calculated to be approximately 4%, and occur at the shock locations, as was also seen with density. Pressure measurements reported for the single scan location have a relative error of approximately 3-4.5%, depending on the location of the measurement. Just as with density and temperature, however, the largest errors of pressure are seen along the jet centerline where shocks are present. At these locations, the relative error of the calculated pressure can be as high as 11.6% (observed at $z = 5.5\ mm$), but the high values of error only persist for small measurement regions. As it was noted with the species SNR's, these are the best case scenarios for error that will be encountered, due to the high number densities within the flow and simple chemistry of the jet.

Table 4.2: Air jet centerline signal to noise ratios for density, temperature, and pressure. Mean values shown are averaged over the length of the jet scan.

Property	Mean SNR along centerline	Max. SNR observed	Min. SNR observed
Density	22.8	36.6	12.4
Temperature	45.7	45.7	24.8
Pressure	19.9	44.8	8.6

4.2 Supersonic vitiation products

The simple air jet allowed us to calibrate the filter AOI in order to improve the accuracy of temperature measurements, and hence pressure as well. Although the composition was measured throughout the experiment, only three species were present during the experiment (N_2, O_2, and H_2O). A vitiation jet was used to produce a flow with hot combustion products that could be used to examine the spectrometer's vibrational Raman technique with varying pressure. The vitiation stage burned methane and air with a very lean equivalence ratio of $\phi_v = 0.42$, and operated at 20.3 *psig* to match the pressure the underexpanded air jet operated at to be consistent. Equilibrium calculations using Cantera yield an adiabatic flame temperature of approximately 1300 K, and molar based composition of approximately 75.6% N_2, 11.7% O_2, 8.4% H_2O, and 4.2% CO_2 for the major species. Methane, carbon monoxide, and molecular hydrogen are not present in the products, which is expected for lean combustion products. The hot supersonic flow also tested the rotational techniques capabilities for measuring flows at an elevated temperature.

The hot jet is produced from the same converging nozzle that used for the cold jet to be consistent between the data sets. The Reynolds number based on the hot conditions of the flow is approximately $Re_{hot} = 30{,}000$. This is noticeably lower than the value calculated for the corresponding cold jet, and is primarily due to the effect of temperature on the gas viscosity. Although the Reynolds number is considerably high, the macroscopic structure of the flow remains steady and stationary for measurements. A scan along the jet axis, commensurate to the air jet, was performed over the same 50 locations, with 100 laser shots collected and averaged at each. All other parameters of the scan were kept consistent with those of the previously discussed air jet.

4.2.1 Thermochemistry results

Figure 4.6 shows the supersonic vitiation jet scan results for density, temperature, and pressure. Right away it is noticeable in Fig. 4.6(a) that the measured density of the vitiation jet is considerably lower than the cold air jet. Because the collected Raman energy is directly proportional to the number density within the probe volume, this reduced density will affect the SNR of both the vibrational and rotational Raman techniques. This will be discussed in the immediately following sub-section. The recognizable Mach diamond pattern is clearly noticeable within the core of the jet, as the density oscillates due to the flow mechanics. The oscillation is also seen in the centerline trace of the density, shown in Fig. 4.7(a).

The core of the supersonic jet is very well defined in Fig. 4.6(a), and can be identified by a constant density contour. As the jet develops downstream of the

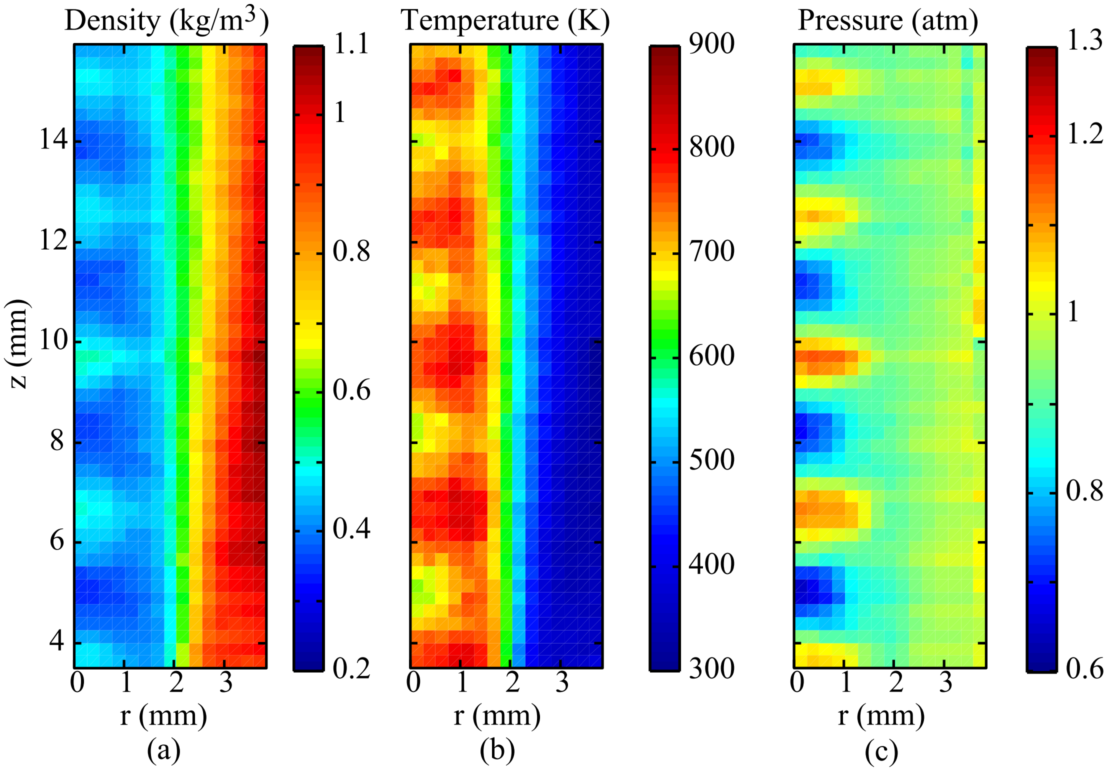

(a)
(b)
(c)

Figure 4.6: Experimental results for the underexpanded vitiation jet, with Re_{hot} = 30,000. The jet emanates from a converging nozzle with a 3.5 mm exit, and total back pressure of 20.3 $psig$. The scan was performed over 50 locations along the jet axis, starting at $z = 3.5$ mm, and 0.254 μm between each scan location. Horizontal pixel binning on the EMCCD yields a pixel size of 256 μm along the jet radius. Density, temperature, and pressure results measured by the line imaging spectrometer are shown in Figs. (a) through (c), respectively.

nozzle exit, the supersonic core contracts, and the mixing layer is observed to grow slightly. The density at the periphery, does not fully achieve the level expected at atmospheric conditions. This is due to heat transfer from the burner surface to the surrounding air in the experiment test section.

Temperature and pressure measurements of the jet and its periphery are shown in Figs. 4.6(b) and (c). Both sets of data show the oscillations between over- and underexpansion in the jet core, and can also be seen in Figs. 4.7(b) and (c). With

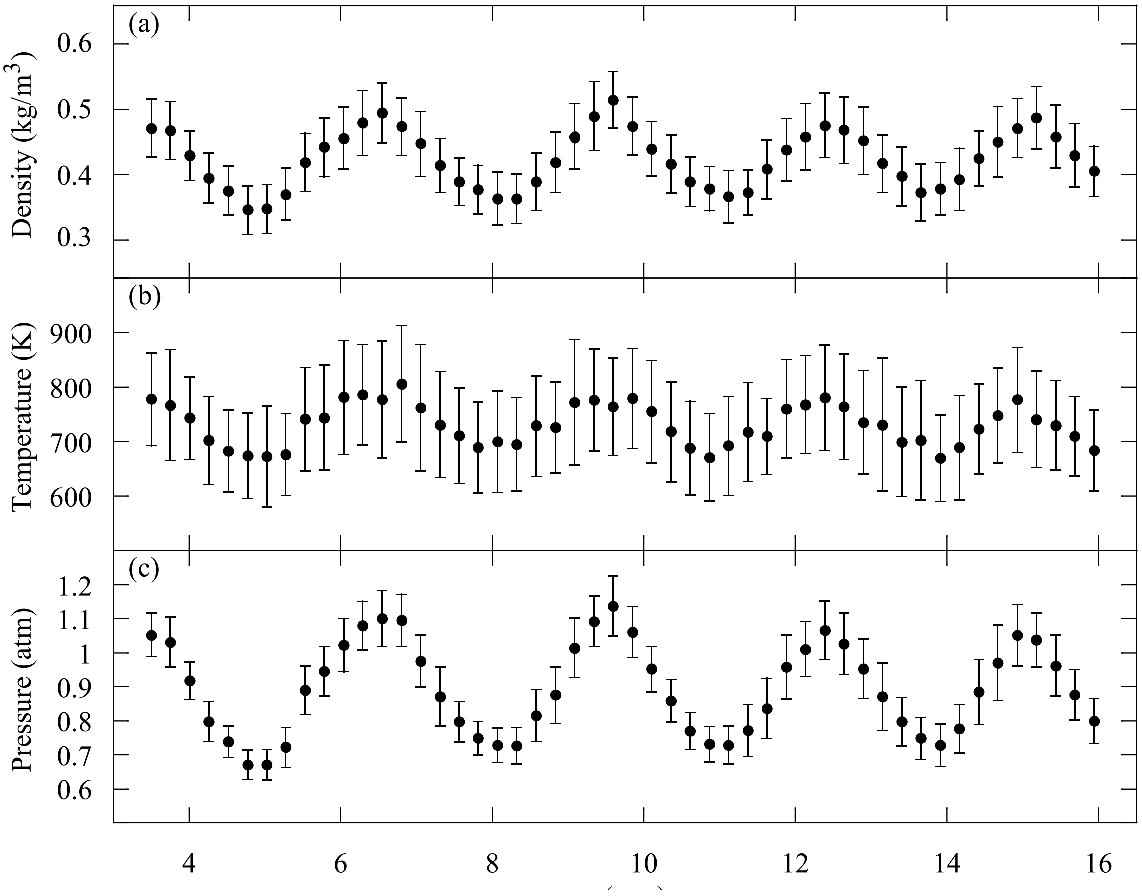

Figure 4.7: Centerline experimental results of (a) density, (b) temperature, and (c) pressure for the vitiation jet. Single-shot statistics were performed to calculate the standard deviations of the measured values, and are shown as the error.

regards to temperature, this repeated behavior is easily seen by oscillatory behavior between 700 and 900 K throughout the well defined jet core. An isotherm at approximately 600 K clearly identifies the extent of the jet core, and agrees with the core seen in the density measurement.

Examination of the calculated pressures does not reveal an outline of the supersonic core, but does give insight into the subtle spreading of the jet mixing layer also seen in the density results. The high and low pressure lobes caused by the jet under- and over expansions are clearly seen in both Figs. 4.6 and 4.9. The overall level of the pressure oscillation, and profile shape, bears similarity with the results from the cold jet. Although the density and temperature do not fully attain atmospheric conditions at the jet periphery, the pressure does approach one *atm*, if not fully arriving at it.

The mole fractions of the main vitiation species are shown in Figs. 4.8(a) through (d). Entrainment of ambient air in the mixing layer is evident when examining the mole fraction results for oxygen, water, and carbon dioxide. Within the mixing layer the mole fraction of oxygen increases to levels closer to the ambient atmosphere, and both water and carbon dioxide decay. It is difficult to see the effect of entrainment in the mixing layer by examining nitrogen, mostly due to its small variation between the vitiation products and ambient air.

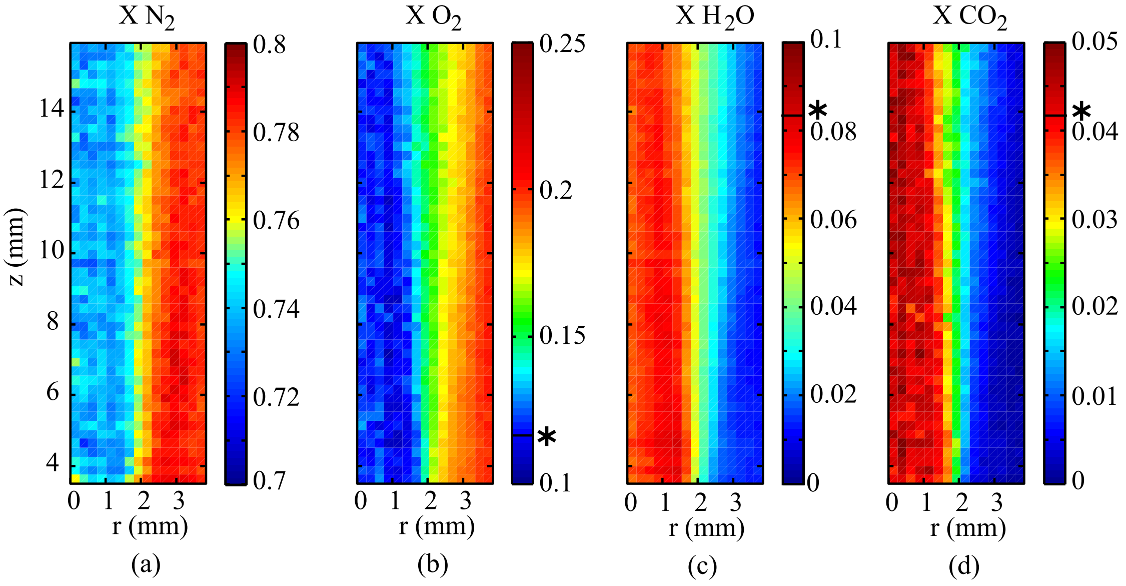

Figure 4.8: Measured mole fractions for the expected species of the vitiation jet shown in Fig. 4.6. The species measured were (a) N_2, (b) O_2, (c) H_2O, and (d) CO_2. Equilibrium calculated mole fractions are indicated by asterisks on the individual legends.

4.2.2 Error and SNR

Single scan location results at $z = 6.3\ mm$ are shown for density, temperature, and pressure in Fig. 4.9. This location was chosen for it's relatively high centerline pressure and density values. Density shows an interesting result, where the fluctuations and error outside the jet are much greater than inside. This is counterintuitive given that measured density inside the jet is less than half of what is seen in the outside of the jet. The turbulent mixing layer, and jet interaction with the quiescent atmosphere, introduce fluctuations in the local density with a relative error of about 13% . Within the supersonic region of the jet, however, the quasi-laminar flow and stationary structure produce a flow that shows less fluctuation in density (relative error approximately equal to 9%). Data for the individual species' SNRs throughout the measurements can be found in Table 4.3.

Table 4.3: Vitiation jet vibrational and rotational signal to noise ratios. Mean values shown are averaged over the length of the jet scan. Vibrational Raman SNR's are reported for the individual species listed in the table.

Species	Mean SNR inside supersonic region	Mean SNR at jet periphery	Max. SNR observed	Min. SNR observed
N_2	10.7	7.1	14.5	4.9
O_2	3.1	5.2	9.3	2.2
H_2O	7.2	5.4	11.5	2.9
CO_2	2.1	1.1	3.3	0.2
IF_{rot}	16.7	19.2	29.3	9.0

The behavior of temperature error within the jet is a compound effect between fluctuations in the IF_{rot} signal collected (proportional to fluctuations in density), and errors in the mixture mole fractions. The two are connected directly to species

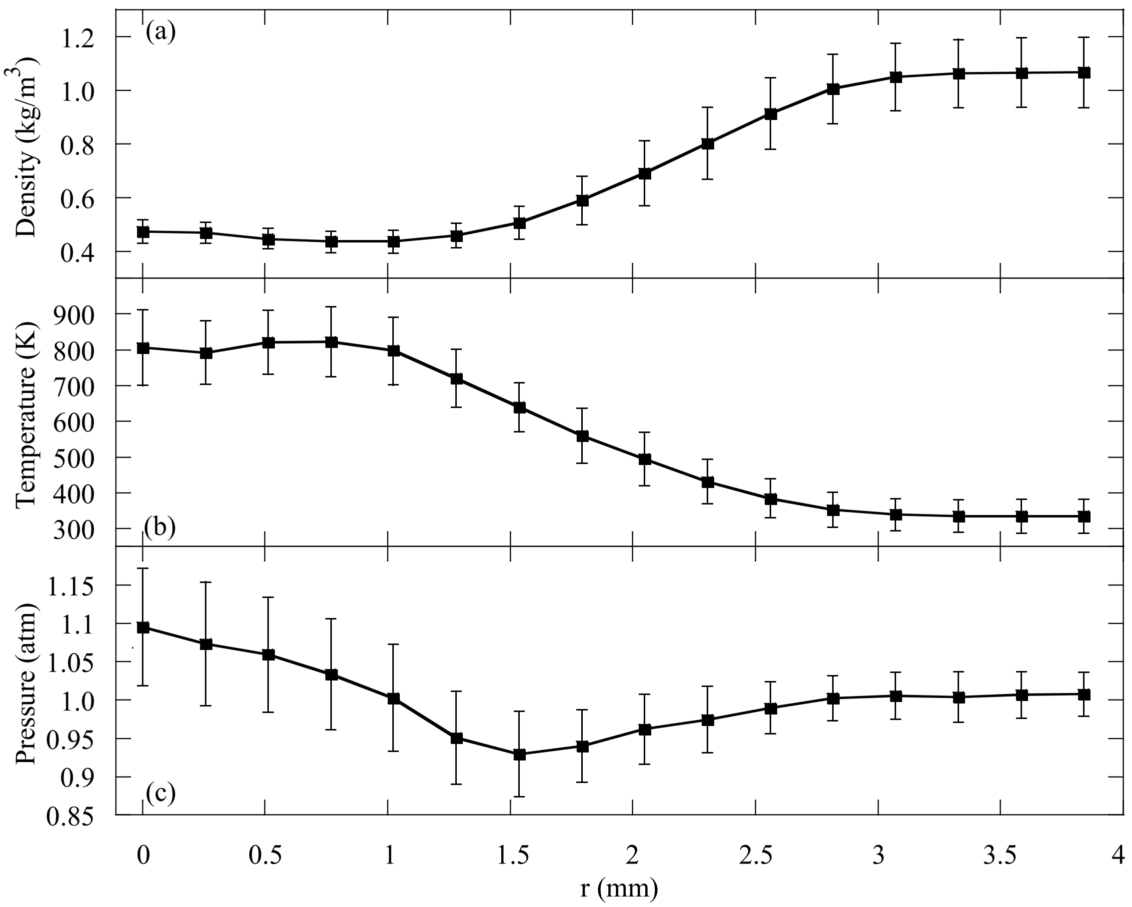

Figure 4.9: Single scan location measurements and errors (standard deviation) at z = 6.3 mm for (a) density, (b) temperature, and (c) pressure. Single-shot statistics were performed to calculate the standard deviations of the measured values.

concentrations measurements. Measured species concentrations at the same scan location as Fig. 4.9 are shown in Fig. 4.10. The relative errors of nitrogen and oxygen concentrations decrease within the supersonic jet for the same reasons mentioned for density. Water and carbon dioxide appear in relatively small quantities overall, and are practically nonexistent at the jet periphery. The large relative errors of these two species concentrations measurements are predominantly due to their low level signals.

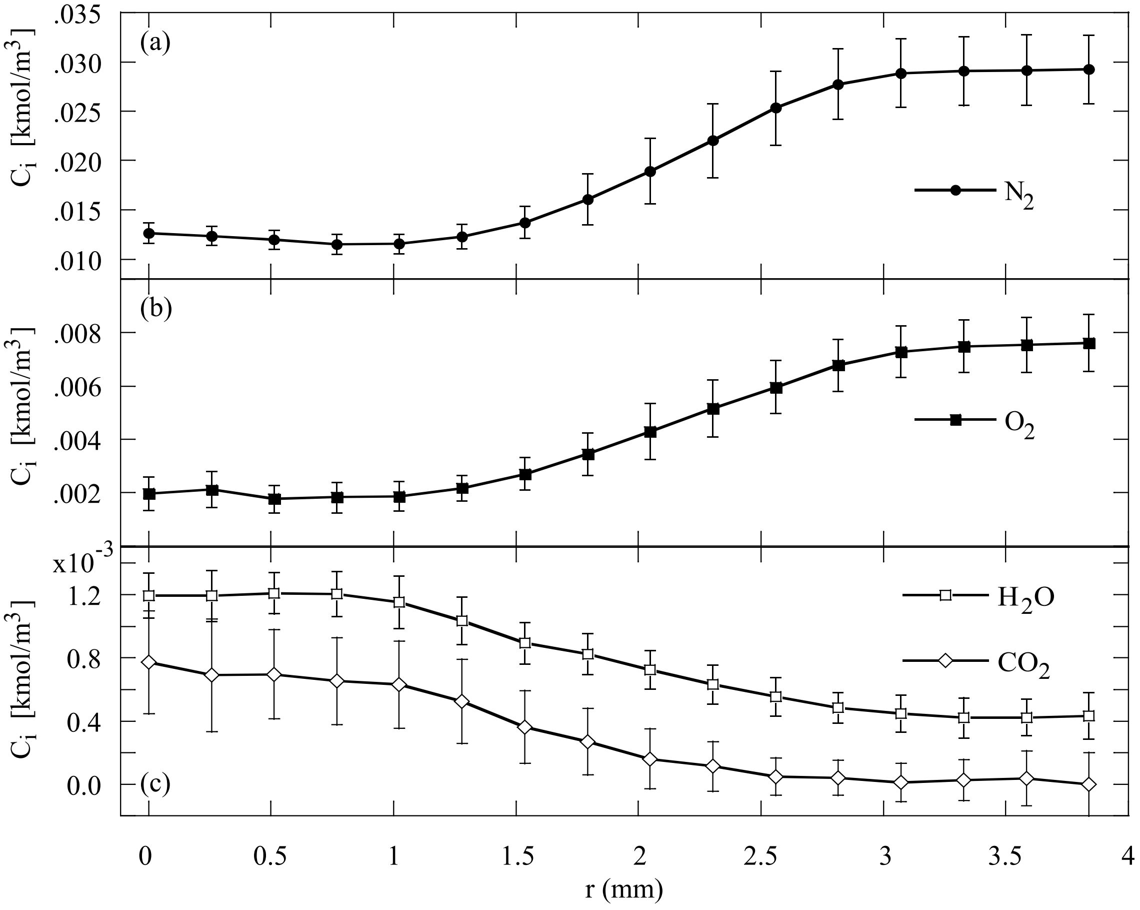

Figure 4.10: Single scan location measurements and errors (standard deviation) at $z = 6.3$ mm for species concentrations of (a) N_2, (b) O_2, (c) H_2O, and CO_2. Single-shot statistics were performed to calculate the standard deviations of the measured values.

Temperature calculations rely on accurate knowledge of the flow composition in order to synthesize rotational Raman spectra. Since the rotational Raman technique is not sensitive to water and carbon dioxide, single shot errors due mole fraction fluctuations are only sensitive to oxygen and nitrogen (for the current composition). Figure 4.11 shows the averaged mole fractions at $z = 6.3$ mm, as well as the error calculated from single shot statistics. The errors of all the species concentrations become relevant when calculating single species mole fractions. Although nitrogen and oxygen concentrations exhibited smaller relative errors within the supersonic region of the jet, their respective mole fractions show the opposite behavior. This is attributed to the mole fraction formulation, as seen in Eq. 3.15. The presence of water and carbon dioxide inside the jet, and their concentration fluctuations, contribute to the single shot errors seen for nitrogen and oxygen. Within the supersonic region of the jet, the compound effects of mole fraction and rotational signal fluctuations yield a relative error of approximately 12% for temperature. Temperature measurements at the jet periphery, and within the mixing layer, show larger relative error ($\sim 16\%$) due to turbulence and unsteadiness of the flow in these regions.

Single shot pressure calculations show large fluctuation of the derived quantity in the supersonic region of the jet. Relative errors within this region vary depending on the behavior of the local fluid mechanics, as seen by the centerline calculations in Fig. 4.7(c). Similar to the cold jet, errors within the center of the jet increase when compressions are present within the local flow. The relative error of pressure can vary between 6 and 12% along the centerline, and between 3 to 7% in the jet periphery and mixing layer. Data summarizing the measurement's SNRs for density, temperature, and pressure along the jet centerline can be found in Table 4.4.

Table 4.4: Vitiation centerline signal to noise ratios for density, temperature, and pressure. Mean values shown are averaged over the length of the jet scan.

Property	Mean SNR along centerline	Max. SNR observed	Min. SNR observed
Density	10.0	13.2	8.0
Temperature	8.1	10.1	6.0
Pressure	12.7	16.7	8.8

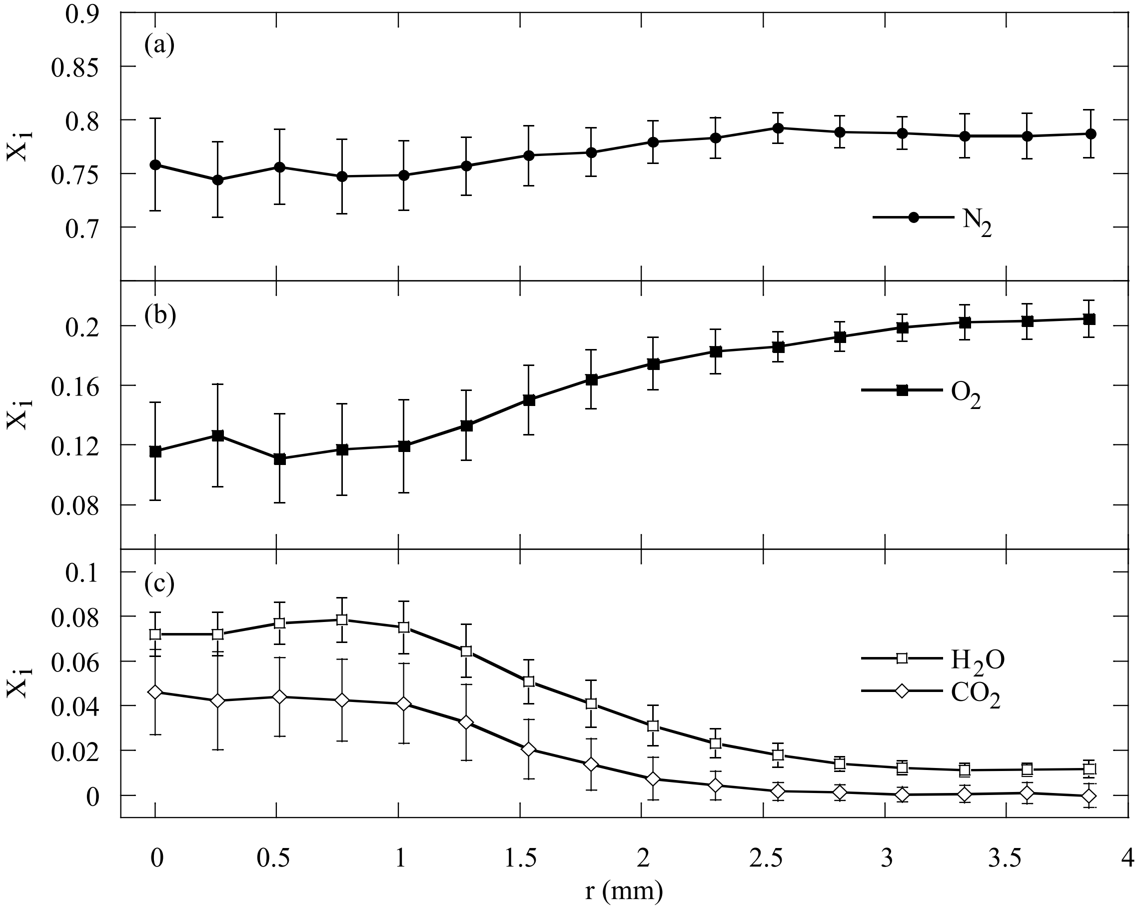

Figure 4.11: Single scan location measurements and errors (standard deviation) at $z = 6.3\ mm$ for species mole fractions of (a) N_2, (b) O_2, (c) H_2O, and CO_2. Single-shot statistics were performed to calculate the standard deviations of the measured values.

4.3 Discussion

Both sets of results for the underexpanded air and vitiation jet show the same underlying jet structure, as it is expected. The oblique shock pattern, or 'Mach diamonds', is visible in the density, temperature, and pressure results for both flow cases. Although the two experiments are formed by flows with contrasting density and temperature, the calculated pressures bear resemblance with each other. Centerline values for the thermodynamic properties confirm the similar oscillation between the two cases, and results from the cold jet show good agreement early in the jet development with the CFD results. For the cold results, the SNRs of the three thermodynamic properties, allow us to obtain precision that is suitable for measurements where a shock is not present. The low number densities of the hot vitiation results negatively effect the SNRs of all species and thermodynamic properties, and hence precision of our measurements.

The subtle decease of the centerline pressure measurements, oscillating about 1 *atm*, indicate that the jets are close the supersonic core termination. This is also apparent in both flows as the high density, temperature, and pressure lobes all shrink in radius as the flow develops. Once the flow can no longer recover from the oblique shocks, it will become fully turbulent and no longer exhibit a stationary structure beyond that point. Entrainment of the ambient air into the center of the jet will increase beyond this point, and the jet will expand at a much faster radial rate.

Entrainment of ambient air into the supersonic regions is impeded, and is clearly visible when the mole fractions are examined. A mixing layer develops in the subsonic region of the flow, and can be seen spreading as the jet develops. For the cold air jet, spreading is observed in the temperature and water mole fraction results, and appears to reach the width of the measurement. The lack of water vapor in the jet provides an indicator of entrainment in the mixing layer, as shown in Fig. 4.1(e). The growing mixing layer clearly incorporates water, and hence ambient air, early on in the entrainment and spreading process. The supersonic region of the jet, however, is clearly defined by the lack of water vapor throughout the length of the jet scan. This is also seen for the vitiation jet in Fig. 4.6, where the supersonic core of the jet maintains approximately constant mole fractions.

5. SUPERSONIC FLAME EVALUATION

5.1 Supersonic flame

Preliminary measurements have been performed in the exhaust of a single supersonic flame. Experiments were conducted with the same converging nozzle used for the previously mentioned supersonic flows, and at the same combustor pressure (20.3 *psig*). The vitiation stage was operated with the same lean equivalence ratio of $\phi_v = 0.42$, and the external equivalence ratio was selected operate at $\phi_e = 0.82$. A lean external equivalence ratio was chosen for the initial examination to avoid visible radiation from heavy sooting and laser-induced fluorescences from polycyclic aromatic hydrocarbons (PAH) [70, 72]. The effects of both could be subtracted if we choose to run a rich flame, but this would still adversely affect the already diminished SNR of the experiment.

The flame used for the experiment can be seen in Fig. 5.1, as well as corresponding schlieren results. The structure of the underexpanded jet can be clearly seen in both images, and bears resemblance to the structure seen in the two previous sets of results. Hot and cold Reynolds numbers for the previous two experiments, based on the length scale of the exit diameter, yielded values of 30,000 and 115,000, respectively. The hot Reynolds number for the current jet will depend on the amount of fuel consumed prior to exiting the nozzle (i.e. exit temperature), but will most likely be on the order of the value calculated for the vitiation jet.

Two additional species, methane and carbon monoxide, will be expected in the measured flame composition. Methane is obviously expected due to the injection of external fuel prior to the nozzle exit. Although some methane will be consumed prior to where the measurements begin, a measurable amount is expected to be observed.

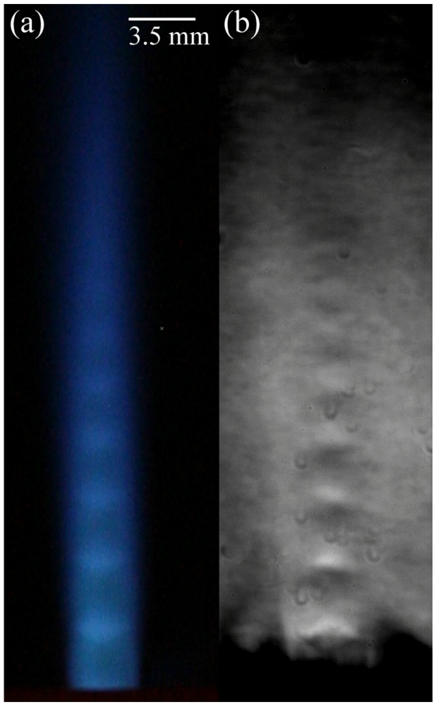

Figure 5.1: (a) Chemiluminescence and (b) schlieren images of the supersonic flame examined by the line imaging spectrometer. Operational parameters of the jet include vitiation equivalence ratio $\phi_v = 0.42$, external equivalence ratio $\phi_e = 0.82$, and 20.3 *psig* chamber pressure.

Carbon monoxide is an intermediate combustion species, and can appear in regions where reactions are allowed to occur (post shock subsonic regions) or where the chemical reactions become frozen.

5.2 Background subtraction

Unlike the previously discussed results, measurements within the supersonic flames increase in complexity due to background signal from the flame. As it can be seen in Fig. 5.1(a), chemiluminescence from the flame is significant, and will appear as signal on the Raman spectrometer. If it is assumed that the flame chemiluminescence does not vary over time, its signal can be subtracted from the collected Raman data in post processing. However, the chemiluminescence does vary with spatial location, as it can be seen in Fig. 5.1(a), and therefore must be measured at every scan location.

Figure 5.2 shows the process of flame subtraction for a single point within the flame measurements ($z = 4$ mm, and $r = 0$ mm). For every scan location within the flame, the signal from the flame chemiluminescence (no excitation laser) is collected and average over 100 shots. Raman data is then collect with the excitation laser, which also includes background signal from the flame itself. It is important to perform the background subtraction first, before the data images are normalized and averaged. The signal from the flame background is not dependent upon the laser energy, and therefore normalizing by the laser energy first would result in largely negative values when subtraction occurs. The results of flame background subtraction and averaging are shown in Fig. 5.2(c). It should be noted that the results shown in this figure are not normalized by the laser energy.

5.3 Preliminary thermochemistry results

Preliminary results of density, temperature, and pressure measurements within the flame can be seen in Fig. 5.3. Measurements begin approximately 4 mm down stream of the nozzle exit, and are collected over 47 scan locations. The spatial resolution in both directions is matched with the previously discussed experiments. The collected data was first background subtracted to account for flame luminosity, and then shot averaged over 100 laser shots.

The flow structure of the jet can be seen in the density results shown in Fig. 5.3(a). Although the results show significant noise in the supersonic region of the jet, a clear oscillation between 0.2 and 0.4 kg/m^3 can be seen. The oscillating structure is reminiscent of the previously examined supersonic jets, and is expected for an underexpanded flow. A clear and discernible outline of the supersonic jet core can be identified, and as the jet develops a gradual spreading of the jet is observed.

The supersonic region of the jet is also easily identified in the temperature mea-

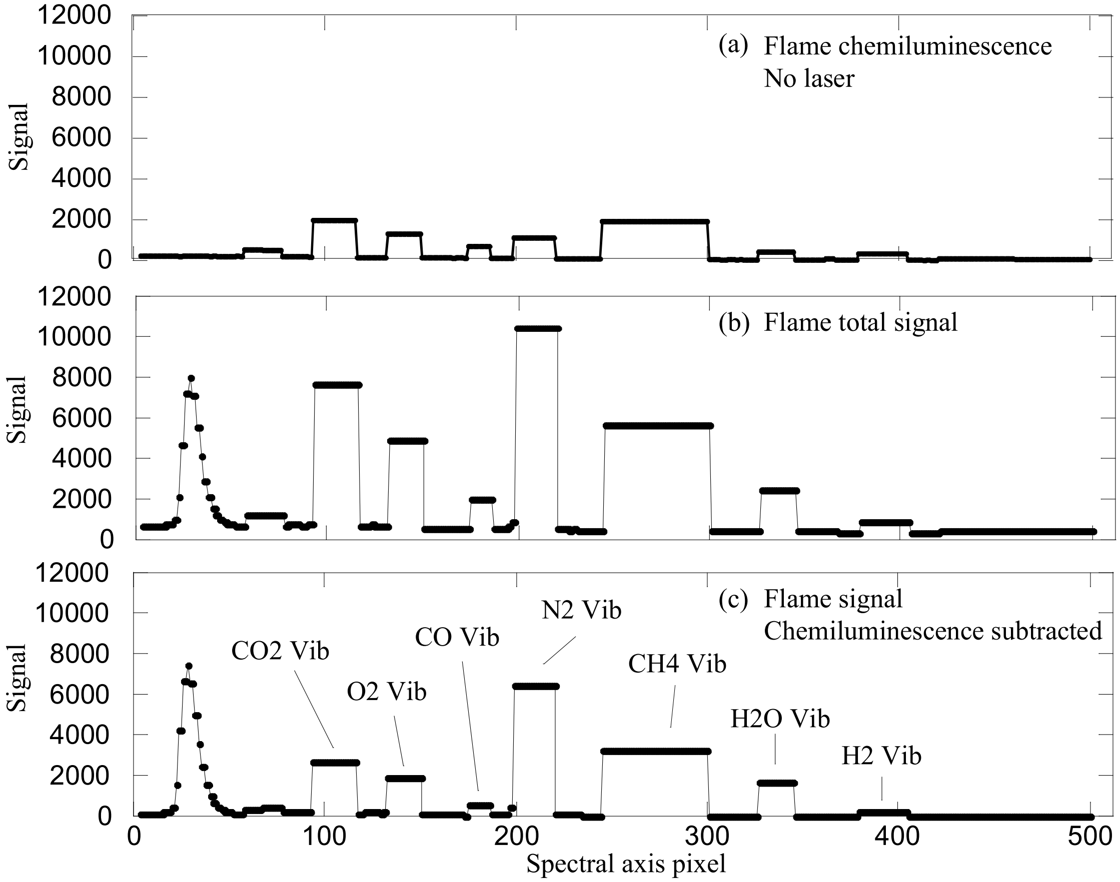

Figure 5.2: Flame chemiluminescence background subtraction process. (a) The flame chemiluminescence is first recorded by the Raman spectrometer. (b) The flame total signal (Raman signal and chemiluminescence) is collected with laser excitation. (c) The recorded chemiluminescence is directly subtracted from the flame's total signal. The data shown here is for flame location $z = 4\ mm$ & $r = 0\ mm$, and is averaged over 100 shots.

surements, shown in Fig. 5.3(b). All the temperatures measured within this region of the jet easily attain values greater than the temperatures previously shown for the vitiation jet. Variations in temperature between 1000 and approximately 1300 K are observed within the supersonic jet, and an oscillating pattern along the center may be discerned amongst all the noise in the data. Temperatures at the jet periphery approach 300 K, but never fully attain that value within the scope of the experiment. Heat transfer from the burner device and the flow itself heat up the surrounding air

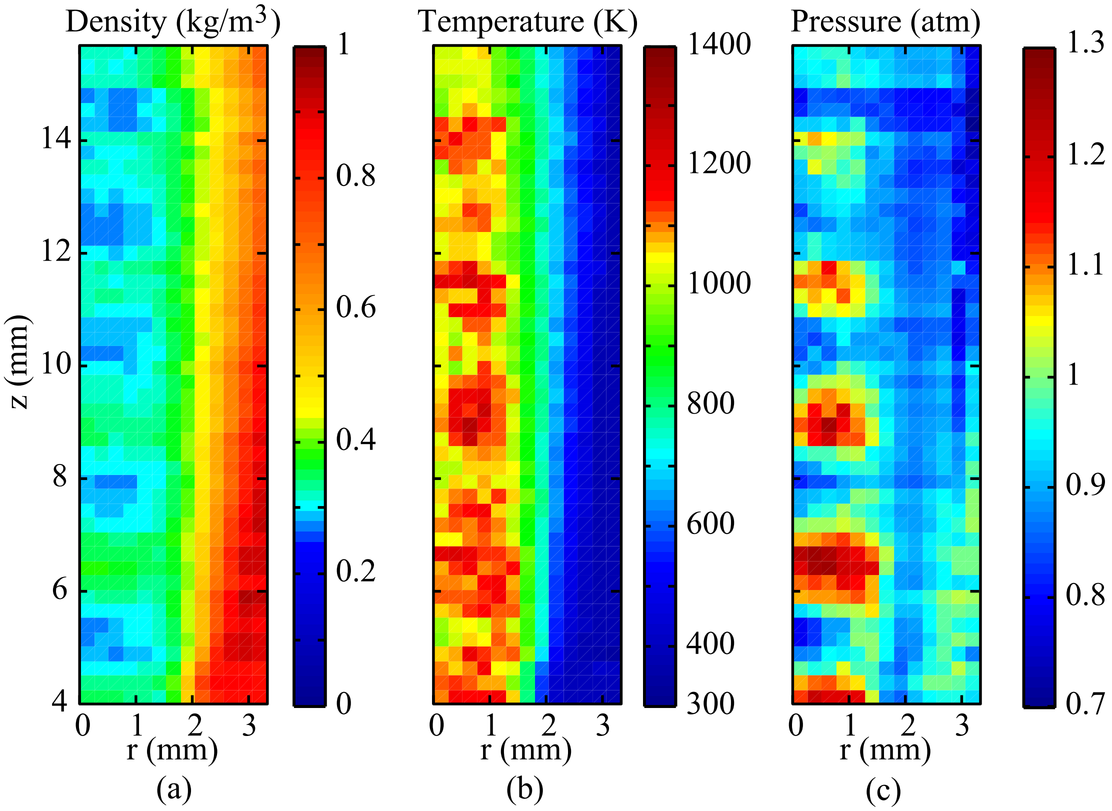

Figure 5.3: Experimental results for the supersonic flame. The flame is generated from a converging nozzle with a 3.5 mm exit, and total back pressure of 20.3 $psig$. The scan was performed over 47 locations along the jet axis, starting at $z = 4\ mm$, and 0.254 μm between each scan location. Horizontal pixel binning on the EMCCD yields a pixel size of 256 μm along the jet radius. Density, temperature, and pressure results measured by the line imaging spectrometer are shown in Figs. (a) through (c), respectively.

to approximately 380 K at the boundary of the measurement.

Pressure within the flame, shown in Fig. 5.3(c), reveals the same jet structure seen in the two previously discussed experiments. An oscillation within the center of the jet is apparent, and can fluctuate between levels of approximately 0.8 and 1.2 atm. Multiple underexpanded regions are easily identified within the supersonic region of the jet, and agree well with high density regions shown in Fig. 5.3(a). Spreading of the jet mixing layer is observed in the calculated pressures, as well as density and the schlieren image in Fig. 5.1(b). The spreading occurs at a rate much faster than previously observed, and may be due to the heat release within the flame.

Species mole fractions measured within the jet are shown in Fig. 5.4. Spatial variations in the methane mole fraction show an interesting result. If it is assumed that the methane is perfectly mixed, the unreacted mole fraction in the vitiation gas should be below approximately $X_{CH4} = 0.05$. However, methane is consumed within the flame, and should take on values less than this. Local regions that reveal high concentrations of methane are most likely due to inhomogeneous mixing within the jet. In the current configuration, methane injection occurs 30 mm prior to the flow exiting the nozzle. This injection distance can be altered, and future experiments will examine the effects of this distance on the resulting flow.

A second interesting result, observed in the jet mole fractions, is the increase of carbon monoxide in down stream regions of the jet. Measurements closest to the jet exit indicate an average carbon monoxide mole fraction of approximately 1.5%, and can reach levels as high as 3.5% downstream. Although the equivalence ratio of the flame is lean ($\phi_e = 0.82$), we observe a buildup of an intermediate species in the flow development. This could be an indication of flame suppression due to the fluid mechanics.

5.4 Feasibility

The primary challenge associated with measurements in a reacting flame is the chemiluminescence background of the flame. Although we attempt to subtract an average of the background seen at every scan location, small fluctuations of the flame will always influence the collected signals. Vibrational and rotational Raman SNR's for the flame scan are shown in Table 5.1. The vibrational Raman responses of nitrogen and water, as well as the integrated filtered rotational response, are the

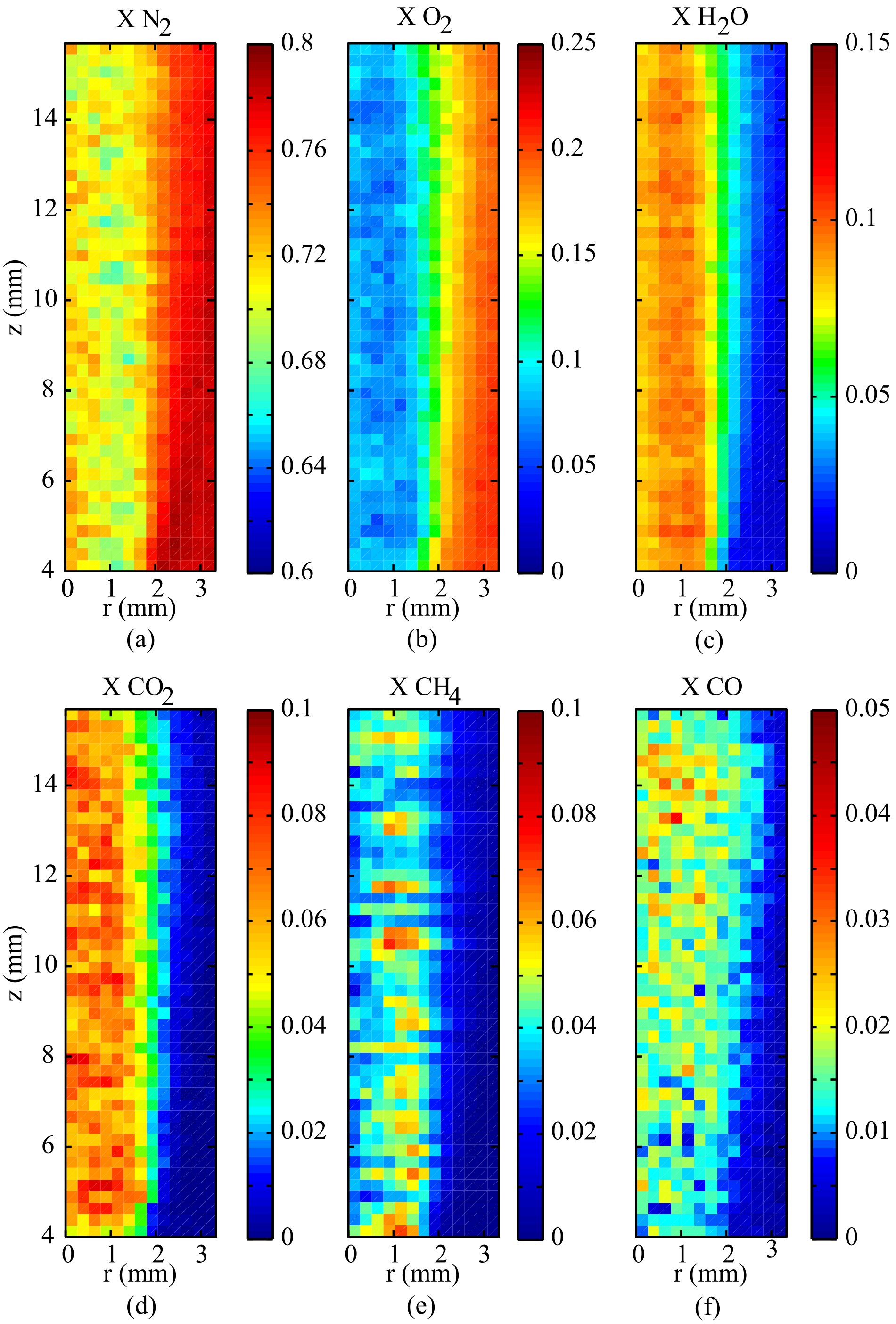

Figure 5.4: Measured mole fractions for the expected species of the supersonic flame shown in Fig. 5.3. The species measured were (a) N_2, (b) O_2, (c) H_2O, (d) CO_2, (e) CH_4, and (f) CO.

only signals that show mean SNR values greater than unity. Even though water has a concentration much less than nitrogen, its differential scattering cross section is approximately two times larger, which allows it to have an appreciable SNR.

Table 5.1: Supersonic flame vibrational and rotational signal to noise ratios. Mean values shown are averaged over the length of the jet scan. Vibrational Raman SNR's are reported for the individual species listed in the table.

Species	Mean SNR inside supersonic region	Mean SNR at jet periphery	Max. SNR observed	Min. SNR observed
N_2	4.1	4.7	7.0	3.2
O_2	0.9	2.8	5.5	0.4
H_2O	3.1	2.8	4.9	1.0
CO_2	0.8	0.6	1.4	0.3
CH_4	0.5	0.5	0.9	0.3
CO	0.4	0.5	1.1	0.1
IF_{rot}	6.3	9.4	20.2	4.4

It is apparent from Fig. 5.3 that density, temperature, and pressure results are hindered by the depreciated species SNR's, reduced signal due to low number density, and flame luminosity background subtraction. The overall supersonic flow structure is discernible when observing the density and pressure results, but is slightly distorted by my noise in the measurements. The post-processed results were software binned in an attempt to try to increase SNR, but unfortunately the reduced resolution concealed the flow structure that was observed. Ultimately the resolution used for all the results present in this work will remain to be able to image flow structure, and techniques for better imaging the flame will have to be implemented. Possibilities for increasing the signal to noise ratio, or reducing flame background signal, include a high speed counter rotating shutter [75], or additional lasers for more excitation energy (refer to Eq. 3.2)

The combination of the new laser diagnostics technique and supersonic flame is still in its early stages. The diagnostics have been applied to the cold and vitiation jets numerous times in the process of developing the technique, and been refined over many trials. Preliminary measurements in the supersonic flames show that the measurements are feasible, band will require careful planning and execution in the future. Implementation of an external rotating shutter may reduce the need for luminosity background subtraction, and could result in better signal to noise ratios.

6. CONCLUSIONS AND FUTURE WORK

A miniaturized combustor has been designed that can be used for the generation of supersonic methane-air flames that are open to the atmosphere, and are therefore accessible to laser diagnostics. The burner is based on a two stage design inspired by jet engine combustors. The first stage is a vitiation burner that provides ignition and flame holding. We explored the salient parameters of operation experimentally, and verified flame holding computationally using a well-stirred reactor model. Both experiments and computations were used to verify a traditional scaling used in jet engine combustor design. Future work will be performed to better characterize the type of flame stabilization that occurs in the second stage of the burner, and to establish initial conditions at the exit of the burner.

A variety of external supersonic flows were examined, with composition corresponding to either vitiation products or external flames. We varied the equivalence ratio of the external supersonic flames, as well as the overall mass flow rate (i.e. average flow Mach number), and examined the flame phenomenology. Future work will examine the thermochemistry for these various flames to examine the effects of initial composition, as well as Mach number.

A rotational and vibrational Raman line imaging spectrometer, capable of full thermochemistry measurements using a single laser and EMCCD, has been developed for measurements in non-isobaric flows. The spectrometer utilizes vibrational Raman signals for species concentration measurements, and measures temperature from the combined rotational signals residing near the excitation wavelength. The independent measurements allow for the calculation of pressure using an equation of state. This system will be used in all future work for measurements of full thermochemistry in various non-isobaric flows.

The Raman line imaging spectrometer measured the exhaust of a simple underexpanded jet, and the thermochemistry measurements were used as a calibration against commensurate CFD results. The density, temperature, pressure, and mole fractions measurements for the supersonic jet agreed well with the computational results, and to the best of our knowledge are the first of their kind.

A vitiated supersonic jet was also measured using the Raman line imaging spectrometer, and results of the full thermochemistry were obtained. The results for species composition show good agreement with what is predicted by equilibrium calculations. The scan of one-dimensional measurements for the supersonic hot flow are the first of their kind. Future experiments in flames will rely heavily on vitiation scans for proper species calibrations.

Initial thermochemistry results were obtained for a lean premixed supersonic flame. These are the first ever measurements of detailed chemistry in a supersonic reacting flow field, and demonstrated the feasibility of applying the Raman line imaging diagnostics to such environments. Future work will apply the laser diagnostics developed in this work to a variety of different supersonic flames. Specifically current work is examining the effect of underexpansion, and consequently exit Mach number, on the flames generated by the supersonic burner. The effect of stoichiometry on flame composition can be quantified using the laser diagnostics system.

REFERENCES

[1] T.C. Adamson and J.A. Nicholls. On the structure of jets from highly underexpanded nozzles into still air. *Journal of the Aerospace Sciences*, 29:16, 1959.

[2] T.J. Anderson and A.C. Eckbreth. Simultaneous coherent anti-stokes raman spectroscopy measurements in hydrogen-fueled supersonic combustion. *Journal of Propulsion*, 8(1):7–15, January 1992.

[3] G. Avila, G. Tejeda, J.M. Fernandez, and S. Montero. The rotational raman spectra and cross sections of H2O, D2O, and HDO. *Journal of Molecular Spectroscopy*, 220(2):259–275, 2003.

[4] R.S. Barlow, R.W. Dibble, and R.P. Lucht. Simultaneous measurement of raman scattering and laser-induced oh fluorescence in nonpremixed turbulent jet flames. *Optics Letters*, 14(5):263–265, 1989.

[5] R.S. Barlow, J.H. Frank, A.N. Karpetis, and J.-Y. Chen. Piloted methane/air jet flames: Transport effects and aspects of scalar structure. *Combustion and Flame*, 143:433–449, 2005.

[6] R.S. Barlow and A.N. Karpetis. Measurements of scalar variance, scalar dissipation, and length scales in turbulent piloted methane/air jet flames. *Flow Turbulence and Combustion*, 72(2-4):427–448, 2004.

[7] R.S. Barlow, A.N. Karpetis, J.H. Frank, and J.-Y. Chen. Scalar profiles and no formation in laminar opposed-flow partially premixed methane/air flames. *Combustion and Flame*, 127(3):2102–2118, 2001.

[8] R.S. Barlow and P.C. Miles. A shutter-based line-imaging system for single-shot raman scattering measurements of gradients in mixture fraction. *Proceedings of the Combustion Institute*, 28(1):269–277, 2000.

[9] R.S. Barlow, G.-H. Wang, P. Anselmo-Filho, M.S. Sweeney, and S. Hochgreb. Application of raman/rayleigh/lif diagnostics in turbulent stratified flames. *Proceedings of the Combustion Institute*, 32:945–953, 2008.

[10] D.E. Battey, J.B. Slater, R. Wludyka, H. Owen, D.M. Pallister, and M.D. Morris. New spectroscopic intrument based on volume holographic optical elements. *Applied Spectroscopy*, 47(11), 1993.

[11] A C. Bayeh and A.N. Karpetis. Feasibility of one-dimensional rotational and vibrational raman in high speed flames. 2012. *50th AIAA Aerospace Sciences Meeting*, Nashville, Tennessee, January 2012, Paper AIAA-2012-0613.

[12] A.C. Bayeh, P. Greco, and A.N. Karpetis. Rotational/vibrational raman line imaging in supersonic flows. *Optics Letters*, In preparation for Opt. Lett.

[13] A.C. Bayeh and A.N. Karpetis. Pressure and thermochemistry measurements in high speed flows using rotational and vibrational raman spectroscopy. 2011. *49th AIAA Aerospace Sciences Meeting*, Orlando, Florida, January 2011, Paper AIAA-2011-1289.

[14] R. Cabra, J.-Y. Chen, R.W. Dibble, A.N. Karpetis, and R.S. Barlow. Lifted methane-air jet flames in a vitiated coflow. *Combustion and Flame*, 143:491–506, 2005.

[15] R. Cabra, T. Myhrvold, J.-Y. Chen, R.W. Dibble, A.N. Karpetis, and R.S. Barlow. Simultaneous laser Raman-Rayleigh-LIF measurements and numerical

modeling results of a lifted turbulent H-2/N-2 jet flame in a vitiated coflow. *Proceedings of the Combustion Institute*, 29:1881–1888, 2003.

[16] K.L. Cashdollar, I.A. Zlochower, G.M. Green, R.A. Thomas, and M. Hertzberg. Flammability of methane, propane, and hydrogen gases. *Journal of Loss Prevention in the Process Industries*, 13(3-5):327–340, May 2000.

[17] T.S. Cheng, J.A. Wehrmeyer, and R.W. Pitz. Simultaneous temperature and multispecies measurement in a lifted hydrogen diffusion flame. *Combustion and Flame*, 91:323–345, 1992.

[18] T.S. Cheng, J.A. Wehrmeyer, R.W. Pitz, O. Jarrett, and G.B. Northam. Raman measurement of mixing and finite-rate chemistry in a supersonic hydrogen-air diffusion flame. *Combustion and Flame*, 99(1):157–173, 1994.

[19] E.T. Curran and S.N.B. Murthy. *Scramjet Propulsion.* AIAA Progress in Aeronautics and Astronautics v. 189, Reston, VA, 2000.

[20] A.D. Cutler, P.M. Danehy, and P.R. Springer. Coherent anti-stokes Raman spectroscopic thermometry in a supersonic combustor. *AIAA Journal*, 41:2451–2459, 2003.

[21] M.C. Drake and G.M. Rosenblatt. Flame temperatures from raman scattering. *Chemical Physics Letters*, 44(2):313–316, 1976.

[22] M.C. Drake and G.M. Rosenblatt. Rotational raman scattering from premixed and diffusion flames. *Combustion and Flame*, 33:179–196, 1978.

[23] J.F. Driscoll, H.H. Hun, Y. Yoon, and J. Donbar. Measured lengths of supersonic hydrogen-air jet flames - compared to subsonic flame lengths and analysis. *Combustion and Flame*, 107(1-2):176–186, 1996.

[24] D. Dussault and P. Hoess. Noise performance comparison of iccd with ccd and emccd cameras. *Optical Science and Technology, the SPIE 49th Annual Meeting*, pages 195–204, 2004.

[25] R.P. Van Duyne, D.L. Jeanmaire, and D.F. Shriver. Mode-locked laser raman spectroscopy. new technique for the rejection of interfering background luminescence signals. *Analytical Chemistry*, 46(2):213–222, 1974.

[26] A.C. Eckbreth. *Laser Diagnostics for Combustion Temperature and Species.* Abacus Press, Cambridge, MA, 1988.

[27] A.C. Eckbreth, G.M. Dobbs, J.H. Stufflebeam, and P.A. Tellex. Cars temperature and species measurements in augmented jet engine exhausts. *Applied Optics*, 23(9):1328–1339, 1984.

[28] R.B. Edelman and P.T. Harsha. Laminar and turbulent gas dynamics in combustors - current status. *Progress in Energy and Combustion Science*, 4:1–62, 1978.

[29] W.R. Fenner, H.A. Hyatt, J.M. Kellam, and S.P.S. Porto. Raman cross section of some simple gases. *JOSA*, 63(1):73–77, 1973.

[30] J.M. Fernandez, A. Punge, G. Tejeda, and S. Montero. Quantitative diagnostics of a methane/air mini-flame by raman spectroscopy. *Journal of Raman Spectroscopy*, 37(1-3), 2006.

[31] R.E. Foglesong, S.M. Green, R.P. Lucht, and J.C Dutton. Dual-pump coherent anti-Stokes Raman scattering for simultaneous pressure/temperature measurement. *AIAA Journal*, 36:234–240, 1998.

[32] J.N. Forkey, N.D. Finkelstein, W.R. Lempert, and R.B. Miles. Demonstration and characterization of filtered rayleigh scatteringforplanar velocity measurements. *AIAA Journal*, 34(3):442–448, March 1996.

[33] J.N. Forkey, W.R. Lempert, and R.B. Miles. Accuracy limits for planar measurements of flow field velocity, temperature and pressure using filtered Rayleigh Scattering. *Experiments in Fluids*, 24:151, 1998.

[34] M.L. Fotia and J.F. Driscoll. Isolator–combustor interactions in a direct-connect isolator-combustor interactions in a direct-connect ramjet-scramjet experiment. *Journal of Propulsion and Power*, 28(1), 2012.

[35] F. Fuest, R.S. Barlow, D. Geyer, F. Seffrin, and A. Dreizler. A hybrid method for data evaluation in 1-d raman spectroscopy. *Proceedings of the Combustion Institute*, 33:815–822, 2010.

[36] K.N. Gabet, N Jiang, W.R. Lempert, and J.A. Sutton. Demonstration of high-speed 1d raman scattering line imaging. *Applied Physics B*, 101:1–5, 2010.

[37] D. Geyer, A. Kempf, A. Dreizler, and J. Janicka. Scalar dissipation rates in isothermal and reactive turbulent opposed-jets: 1-d-raman/rayleigh experiments supported by les. *Proceedings of the Combustion Institute*, 30:681–689, 2005.

[38] I. Glassman. *Combustion*. Academic Press, Boston, MA, 4th edition, 2008.

[39] D.G. Goodwin. An open-source, extensible software suite for CVD process simulation. *Proceedings of CVD XVI and EuroCVD Fourteenth, Electrochemical Society*, 2003.

[40] E.P. Hassel. Ultraviolet raman-scattering measurements in flames by the use of a narrow-band xecl excimer laser. *Applied Optics*, 32(21):4058–4065, 1993.

[41] E.P. Hassel. *RAMSES Spectral Synthesis Source Code.* University of Darmstadt, Darmstadt, Germany, 1996.

[42] P.G. Hill and C.R. Peterson. *Mechanics and thermodynamics of propulsion.* Addison-Wesley Publishing Co., Reading, MA, 1992.

[43] J.O. Hirschfelder, C.F. Curtiss, and R.B. Bird. *Molecular theory of gases and liquids.* Wiley, 1954.

[44] A.G. Hsu, R. Srinivasan, R.D. Bowersox, and S.W. North. Molecular tagging using vibrationally excited nitric oxide in an underexpanded jet flowfield. *AIAA Journal*, 47(11), November 2009.

[45] H. Inaba and T. Kobayasi. Laser-raman scattering methods for remote detection and analysis of atmospheric pollution. *Opto-Electronics*, 4(2):101–123, 1972.

[46] J.R. Janesick, T. Elliott, S. Collins, M.M. Blouke, and J. Freeman. Scientific charge-coupled devices. *Optical Engineering*, 26(8):268692–268692, 1987.

[47] E. Jeong, S. O'Byrne, I. Jeung, and A.F.P. Houwing. Investigation of supersonic combustion with angled injection in a cavity-based combustor. *Journal of Propulsion and Power*, 24(6):1258–1268, 2008.

[48] P. Jerram, P.J. Pool, R. Bell, D.J. Burt, S. Bowring, S. Spencer, M. Hazelwood, I. Moody, N. Catlett, and P.S. Heyes. The llccd: low-light imaging without the need for an intensifier. In *Society of Photo-Optical Instrumentation Engineers (SPIE) Conference Series*, volume 4306, pages 178–186, 2001.

[49] P.A. Jerram, P.J. Pool, D.J. Burt, R.T. Bell, and M.S. Robbins. Electron multiplying ccds. In *SNIC Symposium*, pages 1–5, 2006.

[50] J.E.A. John and T.G. Keith. *Gas Dynamics*. Prentice Hall, 2006.

[51] G.T. Kalghatgi. Lift-off heights and visible lengths of vertical turbulent jet diffusion flames in still air. *Combustion Science and Technology*, 41(1-2):17–29, 1984.

[52] A.N. Karpetis and R.S. Barlow. Measurements of scalar dissipation in a turbulent piloted methane/air jet flame. *Proceedings of the Combustion Institute*, 29:1929–1936, 2002.

[53] A.N. Karpetis and A. Gomez. Temperature measurements in spray flames by spontaneous Raman scattering. *Optics Letters*, 21:704–706, 1996.

[54] R.J. Kee, M.E. Coltrin, and P. Glarborg. *Chemically Reacting Flow: Theory and Practice*. John Wiley and Sons, Inc., 2003.

[55] K.G. Klavuhn and J.C. McDaniel. Underexpanded jet for testing laser-based combustion diagnostics. *Journal of Propulsion and Power*, 17(5):1067 – 1075, September-October 2001.

[56] J. Kojima and Q.-V. Nguyen. Laser pulse-stretching with multiple optical ring cavities. *Applied Optics*, 41(30):6360–6370, October 2002.

[57] J. Kojima and Q.-V. Nguyen. Measurement and simulation of spontaneous Raman scattering in high-pressure fuel-rich H2-air flames. *Measurement Science and Technology*, 15:565–580, 2004.

[58] J. Kojima and Q.-V. Nguyen. Single-shot rotational raman thermometry for turbulent flames using a low-resolution bandwidth technique. *Measurement Science and Technology*, 19(1):015406, 2007.

[59] W. Kreutner, W. Stricker, and T.H. Just. Comparison of spontaneous raman and cars measurements in a laminar flame at atmospheric pressure. *Applied Spectroscopy*, 41(1):98–106, 1987.

[60] G. Laufer, T.M. Quagliaroli, R.H. Krauss, R.B. Whitehurst, and J.C. McDaniel. Planar oh density and apparent temperature measurements in a supersonic combusting flow. *AIAA Journal*, 34(3):463–469, 1996.

[61] S. Lederman. The use of laser raman diagnostics in flow fields and combustion. *Progress in Energy and Combustion Science*, 3:1–34, 1977.

[62] A.H. Lefebvre. *Gas Turbine Combustion.* Hemisphere Publishing Company, Washington, 1983.

[63] A.H. Lefebvre. The role of fuel preparation in low-emission combustion. *Journal of Engineering for Gas Turbines and Power*, 117(4):617, October 1995.

[64] M. Lequime. Tunable thin-film filters: review and perspectives. *Proceedings of The Society of Photo-Optical Instumentation Engineers*, 5250:302–311, 2003.

[65] J.W.L. Lewis and W.D. Williams. Measurement of temperature and number density in hypersonic flow fields using laser raman spectroscopy. In *American Institute of Aeronautics and Astronautics, Aerospace Sciences Meeting, 13 th, Pasadena, CA*, page 1975, 1975.

[66] R.P. Lindstedt, H.C.R.S. Ozarovsky, R.S. Barlow, and A.N. Karpetis. Progression of localised extinction in high reynolds turbulent jet flames. *Proceedings of the Combustion Institute*, 31:1551–1558, 2007.

[67] J.P. Longwell, E.E. Frost, and M.A. Weiss. Flame stability in bluff body recirculation zones. *Industrial & Engineering Chemistry*, 45(8):1629–1633, 1953.

[68] G. Magnotti, A.D. Cutler, and P.M. Danehy. Development of a dual-pump cars system for measurements in a supersonic combusting free jet. 2012. *50th AIAA Aerospace Sciences Meeting*, Nashville, Tennessee, January 2012, Paper AIAA-2012-1193.

[69] L. Martinsson, P.-E. Bengtsson, M. Aldén, S. Kröll, and J. Bonamy. A test of different rotational raman linewidth models: Accuracy of rotational coherent anti-stokes raman scattering thermometry in nitrogen from 295 to 1850 k. *The Journal of Chemical Physics*, 99:2466, 1993.

[70] A.R. Masri, R.W. Bilger, and R.W. Dibble. “fluorescence” interference with raman measurements in nonpremixed flames of methane. *Combustion and Flame*, 68(2):109–119, 1987.

[71] R.L. McCreery. *Raman Spectroscopy for Chemical Analysis*. John Wiley and Sons, Inc., New York, NY, 2000.

[72] W. Meier and O. Keck. Laser raman scattering in fuel-rich flames: background levels at different excitation wavelengths. *Measurement Science and Technology*, 13(5):741, 2002.

[73] R. Menzel, D. Puhlmann, A. Heuer, and W.P. Schleich. Wave-particle dualism and complementarity unraveled by a different mode. *Proceedings of the National Academy of Sciences*, 109(24):9314–9319, 2012.

[74] D.J. Micka and J.F. Driscoll. Combustion characteristics of a dual-mode scramjet combustor with cavity flameholder. *Proceedings of the Combustion Institute*, 32:2397–2404, 2009.

[75] P.C. Miles and R.S. Barlow. A fast mechanical shutter for spectroscopic applications. *Measurement Science and Technology*, 11:392, 2000.

[76] R.B. Miles, W.R. Lempert, and J.N. Forkey. Laser Rayleigh scattering. *Measurement Science and Technology*, 12:R33, 2001.

[77] W.F. Murphy. The rayleigh depolarization ratio and rotational raman spectrum of water vapor and the polarizability components for the water molecule. *The Journal of Chemical Physics*, 67:5877, 1977.

[78] S.P. Nandula, T.M. Brown, and R.W. Pitz. Measurements of scalar dissipation in the reaction zones of turbulent nonpremixed H-2 air flames. *Combustion and Flame*, 99:775–783, 1994.

[79] Q.V. Nguyen, R.W. Dibble, C.D. Carter, G.J. Feichtner, and R.S. Barlow. Raman-lif measurements of temperature, major species, oh, and no in a methane-air bunsen flame. *Combustion and Flame*, 105:499–510, 1996.

[80] S. O'Byrne, P.M. Danehy, S.A. Tedder, and A.D. Cutler. Dual-pump coherent anti-stokes raman scattering measurements in a supersonic combustor. *AIAA Journal*, 45(4):922–933, April 2007.

[81] A. O'Grady. A comparison of emccd, ccd and emerging technologies optimized for low light spectroscopy applications. In *Proc. SPIE*, volume 6093, page 60930S, 2006.

[82] H. Owen, D.E. Battey, M.J. Pelletier, and J.B. Slater. New spectroscopic intrument based on volume holographic optical elements. *SPIE Proceedings*, 2406, April 1995.

[83] C.M. Penney, R.L. Peters, and M. Lapp. Absolute rotational raman cross sections for n2, o2, and co2. *JOSA*, 64(5):712–716, 1974.

[84] N. Peters. Partially premixed diffusion flamelets in non-premixed turbulent combustion. *Proceedings of the Combustion Institute*, 20:353–360, 1985.

[85] N. Peters and F.A. Williams. Liftoff characteristic of turbulent jet diffusion flames. *AIAA Journal*, 21:243, 1983.

[86] T.X. Phuoc. Laser spark ignition: experimental determination of laser-induced breakdown thresholds of combustion gases. *Optics Communications*, 175(4-6):419–423, 2000.

[87] A.E. Potter and E.L. Wong. Effect of pressure and duct geometry on bluff-body flame stabilization. National Advisory Committee on Aeronautics Techical Note 4381, National Advisory Committee on Aeronautics, 1958.

[88] C. Presser, A.K. Gupta, and H.G. Semerjian. Aerodynamic characteristics of swirling spray flames: Pressure-jet atomizer. *Combustion and Flame*, 92(1-2):25–30, January 1993.

[89] W. Reckers, L. Hüwel, G. Grünefeld, and P. Andresen. Spatially resolved multispecies and temperature analysis in hydrogen flames. *Applied Optics*, 32(6):907–924, 1993.

[90] Semrock. Razoredge filters at non-normal aoi. http://www.semrock.com/edge-filter-spectra-at-non-normal-aoi.aspx, 2011. Accessed: October 2, 2011.

[91] S.J. Shanbhogue, S. Husain, and T. Lieuwen. Lean blowoff of bluff body stabilized flames: Scaling and dynamics. *Progress in Energy and Combustion Science*, 35(1):98–120, February 2009.

[92] Z. Shu, B.J. Krass, C.W. Choi, S.K. Aggarwal, V.R. Katta, and I.K. Puri. An experimental and numerical investigation of the structure of steady two-dimensional partially premixed methane-air flames. *Proceedings of the Combustion Institute*, 27:625–632, 1998.

[93] G.P. Smith, D.M. Golden, M. Frenklach, N.W. Moriarty, B. Eiteneer, M. Goldenberg, C.T. Bowman, R.K. Hanson, S. Song, W.C. Gardiner, V.V. Lissianski, and Z. Qin. http://www.me.berkeley.edu/gri_mech/. Accessed: November 1, 2011.

[94] U. Stopper, M. Aigner, H. Ax, W. Meier, R. Sadanandan, M. Stöhr, and A. Bonaldo. Piv, 2d-lif and 1d-raman measurements of flow field, composition and temperature in premixed gas turbine flames. *Experimental Thermal and Fluid Science*, 34(3):396–403, 2010.

[95] S.A. Tedder, J.L. Wheeler, A.D. Cutler, and P.M. Danehy. Width-increased dual-pump enhanced coherent anti-stokes raman spectroscopy. *Applied Optics*, 49(8):1305–1313, March 2010.

[96] P.A. Thompson. *Compressible Fluid Dynamics.* New York, McGraw-Hill, 1971.

[97] P.S. Wilke, C.D. Johnson, E.R. Fosness, S. Crist, D.R. Glass, and P.M. Sherman. Study of the highly underexpanded sonic jet. *AIAA Journal*, 4(1):68–71, 1966.

[98] D.R. Williams, D. McKeown, F.M. Porter, C.A. Baker, A.G. Astill, and K.M. Rawley. Coherent anti-stokes-raman spectroscopy (cars) and laser-induced fluorescence (lif) measurements in a rocket engine plume. *Combustion and Flame*, 94(1-2):77–90, 1993.

[99] F.A. Williams. *Combustion Theory.* Benjamin/Cummings, Menlo Park, CA, second edition, 1985.

[100] W.D. Williams, H.M. Powell, R.L. McGuire, J.H. Jones, L.L. Price, and J.W.L. Lewis. Laser raman diagnostics of temperature and number density in the mixing region of a rocket engine exhaust and a coflowing air stream. *AIAA Paper*, pages 77–211, 1977.

[101] G. Winterfield. On processes of turbulent exchange behind flame holders. *Proceedings of The Combustion Institute*, 10(1265-1275), 1965.

[102] C.S. Yoo, R. Sankaran, and J.H. Chen. Three-dimensional direct numerical simulation of a turbulent lifted hydrogen jet flame in heated coflow: Flame stabilization and structure. *Journal of Fluid Mechanics*, 640:453–481, 2009.

[103] J. Zhao. Image curvature correction and cosmic removal for high-throughput dispersive raman spectroscopy. *Applied Spectroscopy*, 57(11):1368–1375, Nov. 2003.